

Real-time dose compensation methods for scanned ion beam therapy of moving tumors

**Methoden zur Echtzeitdosiskompensation für die Therapie bewegter Tumore mit einem
gescannten Ionenstrahl**

Zur Erlangung des Grades eines Doktors der Naturwissenschaften (Dr. rer. nat.)

genehmigte Dissertation von Dipl.-Phys. Robert Lüchtenborg aus Nordhorn

Januar 2012 — Darmstadt — D 17



TECHNISCHE
UNIVERSITÄT
DARMSTADT



Real-time dose compensation methods for scanned ion beam therapy of moving tumors
Methoden zur Echtzeitdosiskompensation für die Therapie bewegter Tumore mit einem gescannten
Ionenstrahl

Genehmigte Dissertation von Dipl.-Phys. Robert Lüchtenborg aus Nordhorn

1. Gutachten: Prof. Marco Durante, Ph.D.
2. Gutachten: Prof. Dr. Dr. h. c. Gerhard Kraft

Tag der Einreichung: 17. Oktober 2011

Tag der Prüfung: 12. Dezember 2011

Darmstadt — D 17

Summary

Scanned ion beam therapy provides highly tumor-conformal treatments. So far, only tumors showing no considerable motion during therapy have been treated as tumor motion and dynamic beam delivery interfere, causing dose deteriorations. One proposed technique to mitigate these deteriorations is *beam tracking* (BT), which adapts the beam position to the moving tumor. Despite application of BT, dose deviations can occur in the case of non-translational motion.

In this work, *real-time dose compensation combined with beam tracking* (RDBT) has been implemented into the control system to compensate these dose changes by adaptation of nominal particle numbers during irradiation. Compared to BT, significantly reduced dose deviations were measured using RDBT. Treatment planning studies for lung cancer patients including the increased biological effectiveness of ions revealed a significantly reduced over-dose level (3/5 patients) as well as significantly improved dose homogeneity (4/5 patients) for RDBT. Based on these findings, *real-time dose compensated re-scanning* (RDRS) has been proposed that potentially supersedes the technically complex fast energy adaptation necessary for BT and RDBT. Significantly improved conformity compared to *re-scanning*, i.e., averaging of dose deviations by repeated irradiation, was measured in film irradiations. Simulations comparing RDRS to BT revealed reduced under- and overdoses of the former method.

Zusammenfassung

Strahlentherapie mit gescannten Teilchenstrahlen ermöglicht sehr tumorkonforme Dosisverteilungen. Bis jetzt sind jedoch nur Tumore, die sich während der Bestrahlung nicht merklich bewegen, behandelt worden. Tumorbewegung und dynamische Strahlanwendung verursachen Interferenzen, die die resultierende Dosisverteilung beeinträchtigen. Bei einer vorgeschlagenen Technik zur Abschwächung des Bewegungseinflusses, der *bewegungskompensierten Bestrahlung* (BKB), wird der Strahl der Tumorbewegung nachgeführt. Trotz Verwendung dieser Technik können bei nichttranslationaler Bewegung Dosisabweichungen auftreten.

In dieser Arbeit wurde *dosis- und bewegungskompensierte Bestrahlung* (DBKB) implementiert, das diese Dosisabweichungen durch Anpassung der nominellen Teilchenzahlen in Echtzeit kompensiert. Im Vergleich zu BKB wurde eine signifikante Verringerung von Fehldosierungen gemessen. Bestrahlungsplanungsstudien für Lungentumore ergaben eine signifikante Verringerung der Überdosierungen (3/5 Patienten) und eine signifikante Verbesserung der Dosishomogenität (4/5 Patienten). Basierend auf dieser Methode wurde *dosiskompensierte Mehrfachbestrahlung* (DKMB) vorgeschlagen, das ohne die technisch komplexe schnelle Strahlenergieanpassung, die für BKB und DBKB benötigt wird, auskommt. Signifikant bessere Konformität von DKMB im Vergleich zu konventioneller Mehrfachbestrahlung wurde in Filmbestrahlungen gemessen. Außerdem zeigte DKMB in Simulationen geringere Unter- und Überdosierungen als BKB.



Publications related to this work

Peer-reviewed article

Lüchtenborg, R., Saito, N., Durante, M., and Bert, C. (2011). Experimental verification of a real-time compensation functionality for dose changes due to target motion in scanned particle therapy. *Medical Physics*, 38(10):5448–5458.

GSI scientific reports

Lüchtenborg, R., Saito, N., Chaudhri, N., Durante, M., Rietzel, E., and Bert, C. (2009). On-line compensation of dose changes caused by tumor motion. *GSI Scientific Report 2008*, 396.

Lüchtenborg, R., Saito, N., Chaudhri, N., Durante, M., Rietzel, E., and Bert, C. (2010). Upgrade of the therapy control system for on-line dose compensation. *GSI Scientific Report 2009*, 499.

Lüchtenborg, R., Richter, D., Durante, M., Kraft, G., and Bert, C. (2011). Implementation of Beam Tracking and Dose Compensation in TRiP4D. *GSI Scientific Report 2010*, 471.

Patent applications

Lüchtenborg, R. and Bert, C. (2009). Verfahren und Vorrichtung zur Steuerung der Dosisapplikation bei der Bestrahlung. *Patent application*, DE 10 2009 055 902.7.

Bert, C., Lüchtenborg, R., and Richter, D. (2009). Bestrahlungsverfahren und Vorrichtung zur Durchführung des Verfahrens. *Patent application*, DE 10 2009 058 294.0.

Lüchtenborg, R. and Bert, C. (2010). Verfahren zur Erstellung einer Bestrahlungsplanung sowie Verfahren zur Applizierung einer orts aufgelösten Strahlendosis. *Patent application*, DE 10 2010 048 233.1.

Conference contributions

Lüchtenborg, R., Saito, N., Chaudhri, N., Durante, M., Rietzel, E., and Bert, C. (2009). Compensation of dose changes due to intrafractional tumor motion. *DPG spring meeting*. Oral presentation.

-
- Lüchtenborg, R., Saito, N., Chaudhri, N., Durante, M., Rietzel, E., and Bert, C. (2009). On-line compensation of dose changes caused by intrafractional tumor motion. *IBIBAM*. Oral presentation.
- Lüchtenborg, R., Saito, N., Chaudhri, N., Durante, M., Rietzel, E., and Bert, C. (2009). On-line compensation of dose changes introduced by tumor motion during scanned particle therapy. In W. Doessel, O. and Schlegel, W., editors, *IFMBE Proceedings*, 25:449–452. Springer. Oral presentation.
- Lüchtenborg, R., Saito, N., Chaudhri, N., Durante, M., Rietzel, E., and Bert, C. (2009). On-line compensation of dose changes caused by intrafractional tumor motion. *PTCOG 48*. Poster presentation.
- Lüchtenborg, R., Saito, N., Chaudhri, N., Durante, M., Rietzel, E., and Bert, C. (2010). On-line dose compensation for ion beam tracking of moving targets. In *Proceedings of the XVIth ICCR*. Oral presentation.
- Lüchtenborg, R. (2010). Bewegte Tumore bei Strahlentherapie mit gescanntem Teilchenstrahl. *DEGRO*. Invited oral presentation.
- Lüchtenborg, R., Saito, N., Chaudhri, N., Durante, M., Rietzel, E., and Bert, C. (2010). On-line compensation of dose changes caused by intrafractional tumor motion. *Radiotherapy and Oncology*, 96(Supplement 1):S539. Poster presentation.
- Lüchtenborg, R., Saito, N., Chaudhri, N., Durante, M., Rietzel, E., and Bert, C. (2010). Dose compensated re-scanning. *PTCOG 50*. Oral presentation.

Contents

List of Abbreviations	7
1. Introduction	9
1.1. Interaction of radiation and matter	10
1.2. Radiobiology	20
1.3. Photon therapy	28
1.4. Ion therapy	32
1.5. Organ motion in radiotherapy	40
1.6. Aim of this work	48
2. Implementation and experimental verification	51
2.1. Introduction	51
2.2. Material & methods	52
2.3. Results	62
2.4. Discussion	66
2.5. Conclusions	68
3. Treatment planning studies	69
3.1. Clinical particle therapy for lung cancer	69
3.2. Material & methods	70
3.3. Results	83
3.4. Discussion	88
4. Dose compensated re-scanning	91
4.1. Material & methods	92
4.2. Results	95
4.3. Discussion	100
5. Discussion and perspectives	103
6. Conclusions	111
A. Results treatment planning studies	113



List of Abbreviations

4DCT	time resolved computed tomography	PSI	Paul Scherer Institut
AP	anterior-posterior	PTA	planning target area
BT	<i>beam tracking</i>	PTV	planning target volume
CI	conformity index	RBE	relative biological effectiveness
CNAO	centro nazionale di adroterapia oncologica	RDBT	<i>real-time dose compensation combined with beam tracking</i>
CT	computed tomography	RDRS	<i>real-time dose compensated re-scanning</i>
CTV	clinical target volume	RPTC	Rinecker Proton Therapy Centre
DNA	deoxyribonucleic acid	SD	standard deviation
DRRT	dose-rate regulated tracking	SI	superior-inferior
DVH	dose volume histogram	SOBP	spread out Bragg peak
FWHM	full width at half maximum	TA	target area
GSI	GSI Helmholtzzentrum für Schwerionenforschung GmbH	TCS	therapy control system
GTV	gross tumor volume	OAR	organ at risk
HIT	Heidelberg Ion-Beam Therapy Centre	TRiP	Treatment planning for Particles
IC	ionization chamber	VOI	volume of interest
IES	iso-energy slice		
IMRT	intensity modulated radiotherapy		
ITV	internal target volume		
LBT	lateral <i>beam tracking</i>		
LEM	local effect model		
LET	linear energy transfer		
MAO	motion-adaptive-optimization		
MDACC	MD Anderson Cancer Center		
MRI	magnetic resonance imaging		
MSD	motion synchronized delivery		
NIRS	National Institute of Radiological Sciences		
NSCLC	non-small cell lung cancer		
OD	optical density		
PET	positron emission tomography		
PMMA	polymethyl methacrylate		



1 Introduction

Contents

1.1. Interaction of radiation and matter	10
1.1.1. Interaction of photons and matter	10
1.1.2. Interaction of ions and matter	14
1.1.3. Energy loss of electrons	15
1.2. Radiobiology	20
1.2.1. Radiobiological modeling	22
1.2.2. Radiation response	26
1.3. Photon therapy	28
1.4. Ion therapy	32
1.4.1. Projectile ion	32
1.4.2. Application technique	33
1.4.3. Treatment planning	37
1.4.4. GSI particle therapy pilot project	39
1.5. Organ motion in radiotherapy	40
1.5.1. Types of organ motion	40
1.5.2. Motion acquisition	42
1.5.3. Mitigation of organ motion influence	43
1.6. Aim of this work	48

The development of radiotherapy techniques is mainly driven by the aim to deliver dose distributions as conformal as possible to the tumor. Transferring the high tumor conformity nowadays achievable in stationary treatments to the treatment of moving tumors is technically challenging. This work focuses on the treatment of mobile tumors.

Reports about cancer incidence and mortality are published by Husmann most recently for 2006 et al. (Husmann et al., 2010). Data with regard to lung cancer are reported here. For men as well as for women lung cancer had the third highest incidence rate (47.100 or 11% of all incidences in Germany). In the same year 210.930 people in Germany died from cancer (19% or 40.771 cases among them because of lung cancer). Among men lung cancer is even the most

frequent cause of cancer death in Germany. These numbers indicate a relatively poor prognosis for lung cancer patients.

The three most common treatment options for cancer are surgery, radiotherapy and chemotherapy. They are also used in combination. Radiotherapy is the therapeutic application of ionizing radiation. It is further divided into internal radiotherapy where the radiation source is inside the body (e.g., brachytherapy where needles are used to place a radioactive source directly inside the tumor.) and external radiotherapy where an external source, e.g., an accelerator, is employed to deliver radiation to the body. This work will focus on external radiotherapy thus if not stated otherwise radiotherapy in the following refers to external radiotherapy.

The aim of curative radiotherapy is to sterilize a, typically local, tumor by depositing sufficient dose to the tumor tissue. Ionizing radiation can damage cells. If the damage is severe enough the cell will subsequently die and a tumor can be sterilized. Not only tumor but also normal cells are damaged by radiation causing side effects. To reduce the probability for side effects the dose to the healthy tissue surrounding the tumor should be kept as low as possible. To understand the rationale for radiotherapy some knowledge concerning the interaction of radiation and matter as well as radiobiology is indispensable. Thus, these two topics are addressed in this chapter before different radiotherapy methods are introduced. The last part of this chapter is dedicated to organ motion in radiotherapy.

1.1 Interaction of radiation and matter

For this work radiation therapy employing ions is investigated. The majority of radiotherapy treatments is carried out with photons. There are distinctive differences but also similarities in the physical principles of these two therapy approaches. Thus, the following sections outline the interaction of these radiation types with matter. An overview about photon interactions with matter with focus on radiotherapy applications can be found, e.g., in Alpen (Alpen, 1998). A comprehensive overview concerning the interaction of particles with matter is given by the Particle Data Group (Nakamura and Particle Data Group, 2010).

1.1.1 Interaction of photons and matter

While passing through matter photons lose energy or are absorbed undergoing different processes. The intensity I of a monoenergetic photon beam with initial intensity I_0 after passing a homogeneous material of thickness d can be described by an exponential function:

$$I = I_0 \cdot e^{-\mu d}. \quad (1.1)$$

The linear attenuation coefficient μ depends on photon energy and material. In practice the coefficient is often normalized to the material density ρ to make it independent from the material's physical state. The normalized quantity is called the mass attenuation coefficient. Different physical processes contribute to the total mass attenuation coefficient. They are outlined in the following.

Coherent scattering

Coherent scattering, also referred to as Rayleigh scattering, does not transfer energy to the medium. Electron oscillations are induced by interactions between photons and electrons. The subsequently emitted photons have the same energy as the incident photons but a different direction. Hence this process enlarges the angular dispersion of the incident photon beam. The linear attenuation coefficient σ_{coherent} of this process is negligible for photon energies above 100 keV. It thus plays no relevant role for radiotherapy.

Photoelectric effect

The photoelectric effect is the absorption of a photon by an atom. The absorbed photon energy is released by emission of an electron from one of the atomic shells. The energy E_{e^-} of the emitted electron equals the photon energy $h\nu$ reduced by the electron's binding energy E_b :

$$E_{e^-} = h\nu - E_b, \quad (1.2)$$

where h means the Planck constant and ν is the frequency of the impinging photon. The electron hole in the atomic shell is refilled by an electron from an outer orbital. The energy difference between the orbitals can be emitted via a photon or an Auger electron. The linear attenuation coefficient $\tau_{\text{photoelectric}}$ for the photoelectric process is largest for small photon energies. Its dependence on photon energy can approximately be described by $(h\nu)^{-3}$ but has sharp peaks at the binding energies of the electron orbitals.

Compton scattering

Compton scattering describes a process where an impinging photon is scattered at a loosely bound electron and transfers a part of its energy to the electron. The energy of the quasi-free electron is given by the energy difference of the incident and the scattered photon:

$$E_{e^-} = h\nu - h\nu', \quad (1.3)$$

where ν and ν' mean the frequency of the incident and scattered photon, respectively. The Compton scattering linear attenuation coefficient σ_{Compton} is almost independent of atomic number and decreases with increasing photon energy. In the energy range between 100 keV and 10 MeV Compton scattering is the dominant photon interaction process in soft tissue material.

Pair production

Pair production is only possible if the photon energy $h\nu$ exceeds twice the rest energy of an electron with mass m_e : $h\nu > 2m_e c^2$. In the nucleus field of an atom the photon can be absorbed and an electron positron pair can be produced. While the excitation state of the nucleus remains unchanged energy and momentum are partly transferred to the nucleus. Since the amount of energy transferred to the nucleus is very small the energy of the electron E_{e^-} and the positron E_{e^+} can be written as:

$$E_{e^-} + E_{e^+} = h\nu - 2m_e c^2. \quad (1.4)$$

The linear attenuation coefficient κ_{pair} for pair production increases with the square of the atomic charge: $\kappa_{\text{pair}} \propto Z^2$. Especially for high energetic photons Z in this equation has to be corrected for the screening effect taking into account that the atomic charge of the nucleus is partly screened by shell electrons.

Total mass attenuation coefficient

The total mass attenuation coefficient μ/ρ is the sum of the contributions from the single processes:

$$\frac{\mu}{\rho} = \frac{1}{\rho} \left(\sigma_{\text{coherent}} + \tau_{\text{photoelectric}} + \sigma_{\text{Compton}} + \kappa_{\text{pair}} \right). \quad (1.5)$$

The mass attenuation coefficients of water represent biological tissue very well when scaled to the respective density. The mass attenuation coefficients for water are shown in Figure 1.1 on the facing page.

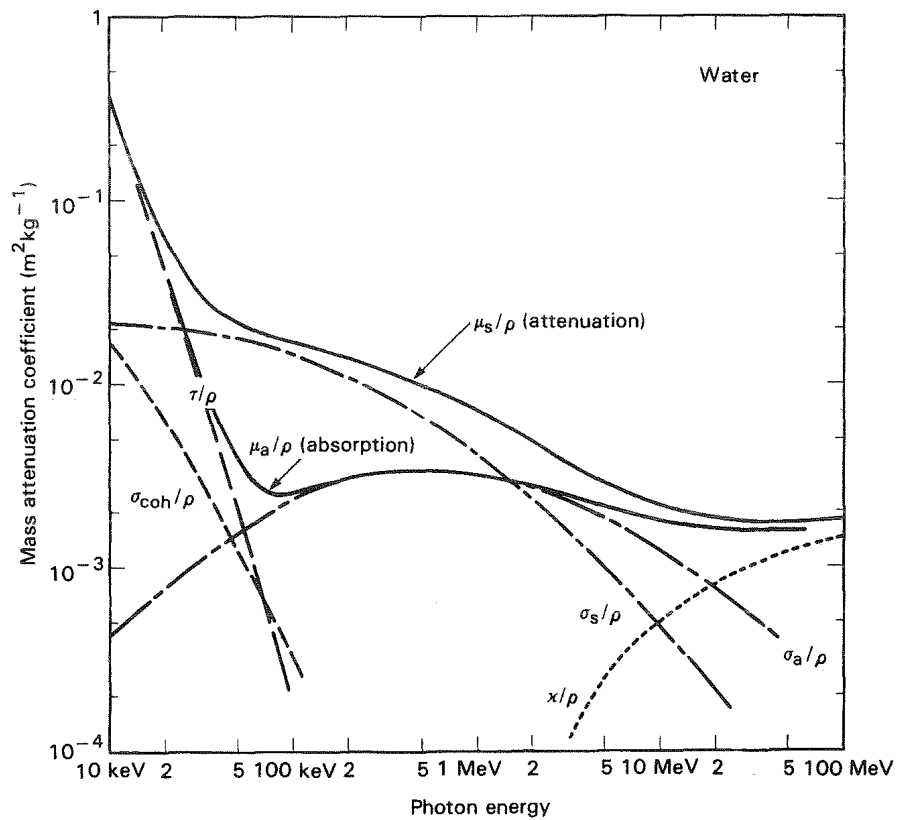


Figure 1.1.: Mass attenuation coefficients in water for a range of photon energies. The coefficients for energy scattered μ_s/ρ and energy absorbed μ_a/ρ are shown separately. The dominating process contributing to energy absorption between 100 keV and 10 MeV is Compton scattering. Figure from (Alpen, 1998).

1.1.2 Interaction of ions and matter

The interaction of ions and more generally charged particles with matter has been quantum mechanically described by Bethe (Bethe, 1930). At moderately relativistic energies the mean rate of energy loss is given by the Bethe equation:

$$-\left\langle \frac{dE}{dx} \right\rangle = \frac{4\pi N_e z_{\text{eff}}^2}{m_e c^2 \beta^2} \left(\frac{e^2}{4\pi\epsilon_0} \right)^2 \left[\frac{1}{2} \ln \left(\frac{2m_e c^2 \beta^2 \gamma^2 T_{\text{max}}}{I^2} \right) - \beta^2 \right], \quad (1.6)$$

where N_e is the absorber's electron density, z_{eff} is the effective projectile's charge in units of the electron charge, c is the vacuum speed of light, β is the projectile speed in units of c , γ is the relativistic Lorentz factor $\gamma = 1/\sqrt{1 - \beta^2}$, I is the mean excitation energy of the absorber and T_{max} is the maximum kinetic energy that can be transferred per collision. The electron density of the absorber material can be given either in electrons/cm³ or in electrons/g. In analogy to introducing the mass attenuation coefficient in Section 1.1.1 the latter definition of electron density has the advantage of providing a mean energy loss independent of absorber density. The mean energy loss in that case is given in units of MeV cm²/g. The absorber atoms are excited or ionized by the energy transferred from the projectiles.

The main dependencies can easily be seen from this equation. The mean energy loss increases with the square of the projectile's charge. Going to low projectile energies the mean energy loss increases with $1/\beta^2$. This behavior can be understood if considering that at lower energies the interaction time a projectile spends in the Coulomb field of an atom increases.

Several corrections need to be applied to this equation if the projectile's energy is very high or very low. For therapy applications only the low energy corrections are of interest. In this case T_{max} can be approximated by (Nakamura and Particle Data Group, 2010):

$$T_{\text{max}} = 2m_e c^2 \beta^2 \gamma^2. \quad (1.7)$$

The Bethe equation (Equation 1.6) can then be approximated by:

$$-\left\langle \frac{dE}{dx} \right\rangle = \frac{4\pi N_e z_{\text{eff}}^2}{m_e v^2} \left(\frac{e^2}{4\pi\epsilon_0} \right)^2 \left[\ln \left(\frac{2m_e v^2}{I} \right) + \text{corrections} \right], \quad (1.8)$$

where v is the projectile velocity.

The Bethe equation is proportional to z_{eff}^2 . A more precise description, taking into account higher orders of z_{eff} is needed especially for low energies. At low energies also atomic bindings

become relevant. For a detailed discussion of low energy corrections to the Bethe equation the reader is referred to ICRU report 49 (ICRU, 1993b).

The rationale for the introduction of the effective charge are electron capture processes reducing the projectile's charge. They are important if the projectile velocity is in the order of the velocity of the absorber's outer shell electrons. A correction has been found by Barkas (Barkas, 1963):

$$z_{\text{eff}} = z \left(1 - e^{-125\beta z^{-\frac{2}{3}}} \right). \quad (1.9)$$

Several descriptions for the regime of extremely small projectile energies have been found (Andersen and Ziegler, 1977; Lindhard et al., 1963).

The energy loss for an ion is shown in Figure 1.2.

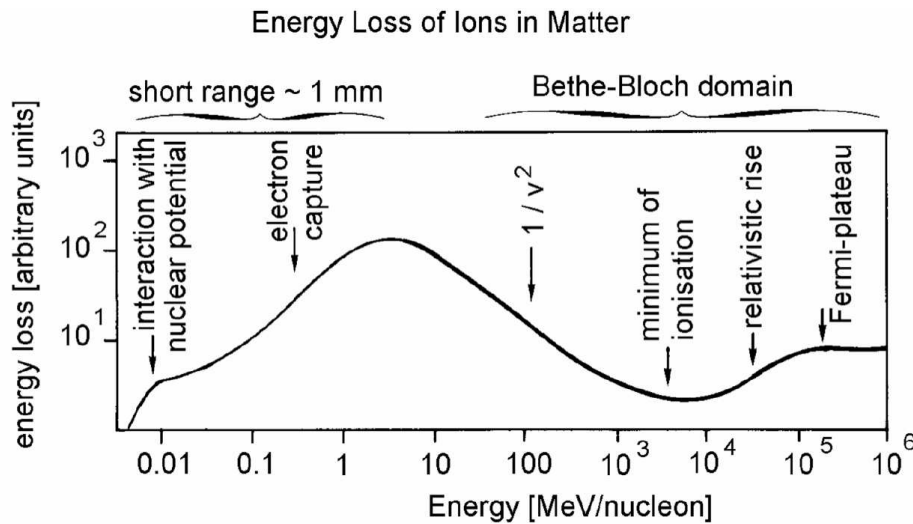


Figure 1.2.: Energy loss of ions. The Bethe equation describes the particle in a moderate energy regime quite well. For low energies electron capture lowering the effective projectile charge and eventually nuclear interactions become important.

The Bethe equation only describes the electronic energy loss. At extremely low energies ions lose energy primarily via nuclear reactions. The energy loss for protons (electronic energy loss) and carbon ions (electronic and nuclear energy loss) can be seen in Figure 1.3 on the next page.

1.1.3 Energy loss of electrons

Both kinds of radiation, photons as well as ions cause ionization of the absorber material. The produced electrons subsequently lose their kinetic energy when travelling through the material. Thus, the main energy transfer to the medium for both types of radiation happens via energy loss of the electrons. Electrons lose energy primarily via ionization and Bremsstrahlung. The

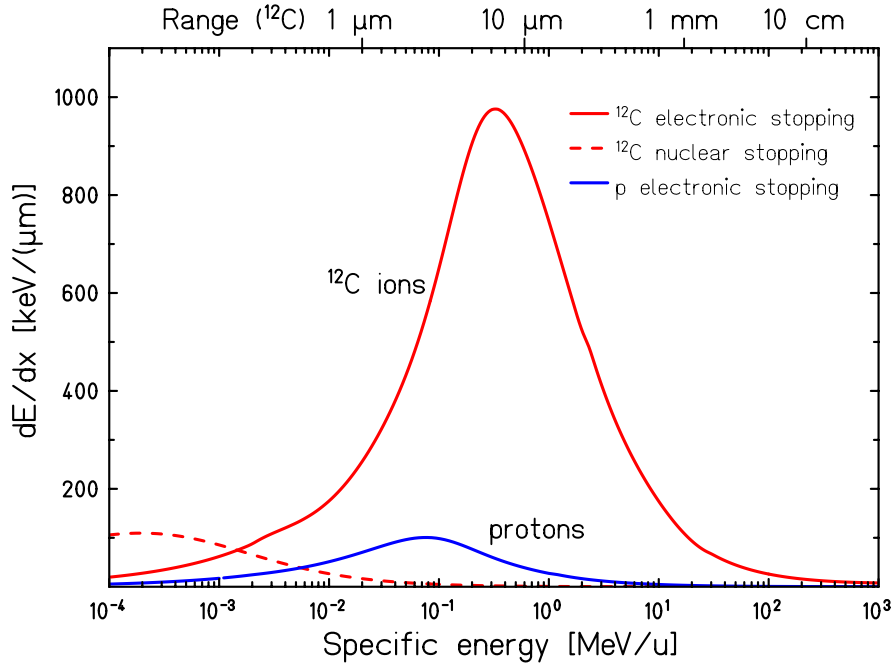


Figure 1.3.: Energy loss for protons and carbon ions. For carbon ions also the nuclear energy loss is given that is the dominating process only at extremely low energies. Figure from (Schardt et al., 2010).

energy loss for both processes depends on the electron energy E_{e^-} . These dependency can be approximated by (Nakamura and Particle Data Group, 2010):

$$-\left\langle \frac{dE}{dx} \right\rangle_{\text{ion}} \propto \ln(E_{e^-}) \quad (1.10)$$

for ionization as well as

$$-\left\langle \frac{dE}{dx} \right\rangle_{\text{BS}} \propto E_{e^-} \quad (1.11)$$

for Bremsstrahlung. Thus, for high energies Bremsstrahlung is the dominating process while for low energies the energy loss is dominated by ionization events. For the therapeutic energy regime the main energy loss mechanism for electrons is ionization. The mean free path length of an electron depends on its energy. It has a minimum around 100 eV where the mean free path length is in the order of 1 nm. As will be shown in Figure 1.6 on page 20, this length is characteristic for the critical target in radiotherapy, the cell's deoxyribonucleic acid (DNA).

From the approximation in Equation 1.7 on page 14 that is valid for therapeutic energies it can be seen that the maximal electron energy is only dependent on the projectile velocity and not e.g., its mass or charge. The maximal electron energy determines the maximal range of the

electrons and thus the radius of the dose distribution around a particle track. A parameterization for the track radius has been found by Kiefer and Straaten (Kiefer and Straaten, 1986):

$$r_{\max} = \gamma T_{\max}^{\delta}, \quad (1.12)$$

with $\gamma = 0.062 \mu\text{m} (\text{MeV/u})^{-1.7}$ and $\delta = 1.7$.

Implications for therapeutic beam application

For therapeutic applications the depth dose profile of the therapeutic radiation beam is of outstanding importance. Photons deposit the highest local dose shortly after entering the material (see Figure 1.4 on the following page). This can be explained when considering that the photon intensity is more and more attenuated (see Equation 1.1 on page 10). The short build up period before reaching the maximal local dose is due to the non-isotropic emission of electrons from primary ionizations, mainly Compton electrons. They are emitted preferably in beam direction. In contrast to the photon depth dose profile, ions are characterized by an inverted depth dose profile where the highest local dose deposition happens at the very end of the particle track, the so called Bragg-Peak region (see Figure 1.4 on the following page). This can be understood if taking into account that the mean energy loss increases with $1/v^2$ for slow particles and at the very end of the track decreases again as the effective charge diminishes (see Section 1.1.2).

The interaction mechanism for dose deposition for photons as well as for different ions is primarily via secondary electrons. Nevertheless the therapeutic efficacy of photons and ions differs. Moreover the efficacy for different ion types differs. These differences are caused by the different dose distributions. Differences are apparent on the macroscopic as well as on the microscopic scale. The macroscopic depth dose profiles for photons and ions have already been introduced above. The dose distribution of different ions on the microscopic scale have been simulated by Krämer and Kraft (Krämer and Kraft, 1994). Results of these simulations are shown in Figure 1.5 on page 19. The key to understanding the differences in the biological efficacy of different types of radiation lies in radiobiology. Thus, in the following section some fundamental concepts of radiobiology are introduced.

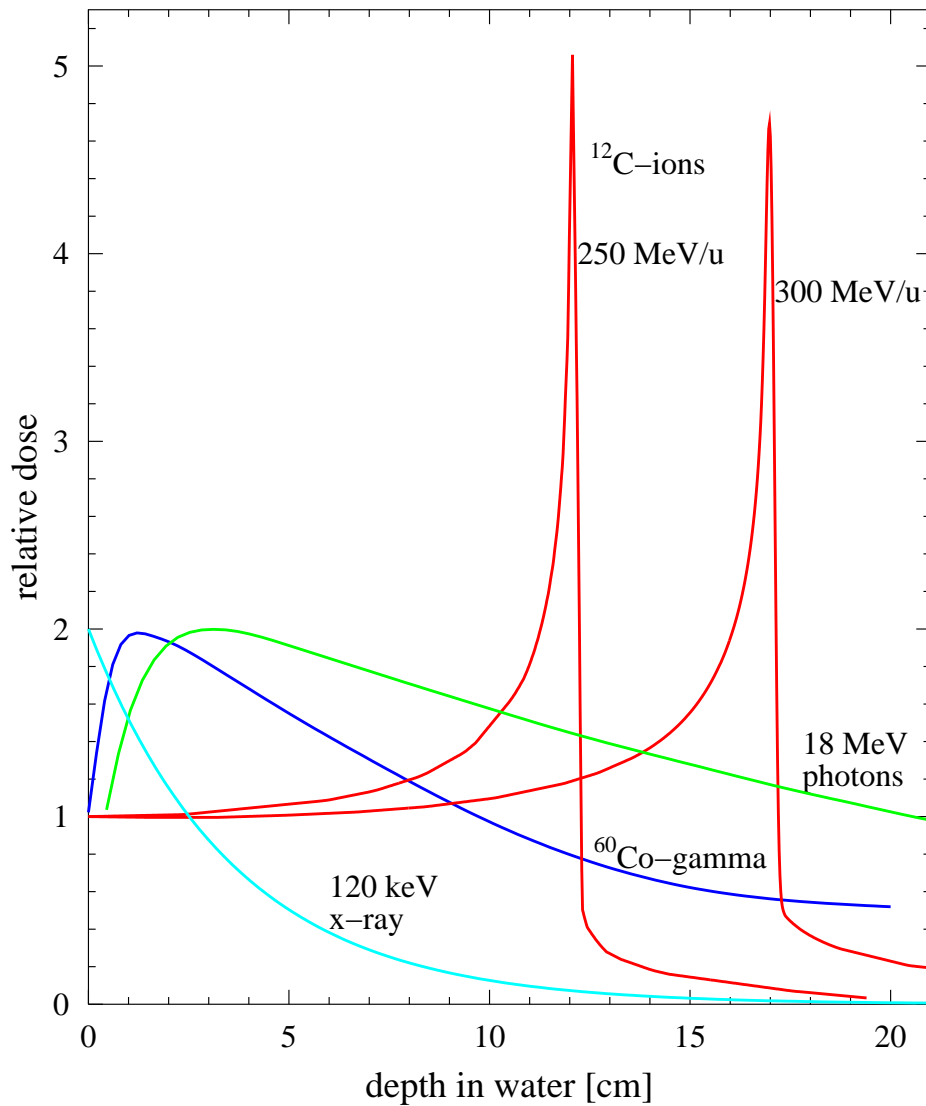


Figure 1.4.: Depth dose profiles of photons with different energy spectra compared to carbon ions at different energies. The dose deposition of ions is concentrated to the distal end of the particle track, the so called Bragg-Peak. The depth of the Bragg-Peak can be varied by changing the ion energy. The depth dose distribution for photons shows an exponential decrease after a build up depending on the energy spectrum of the photons.

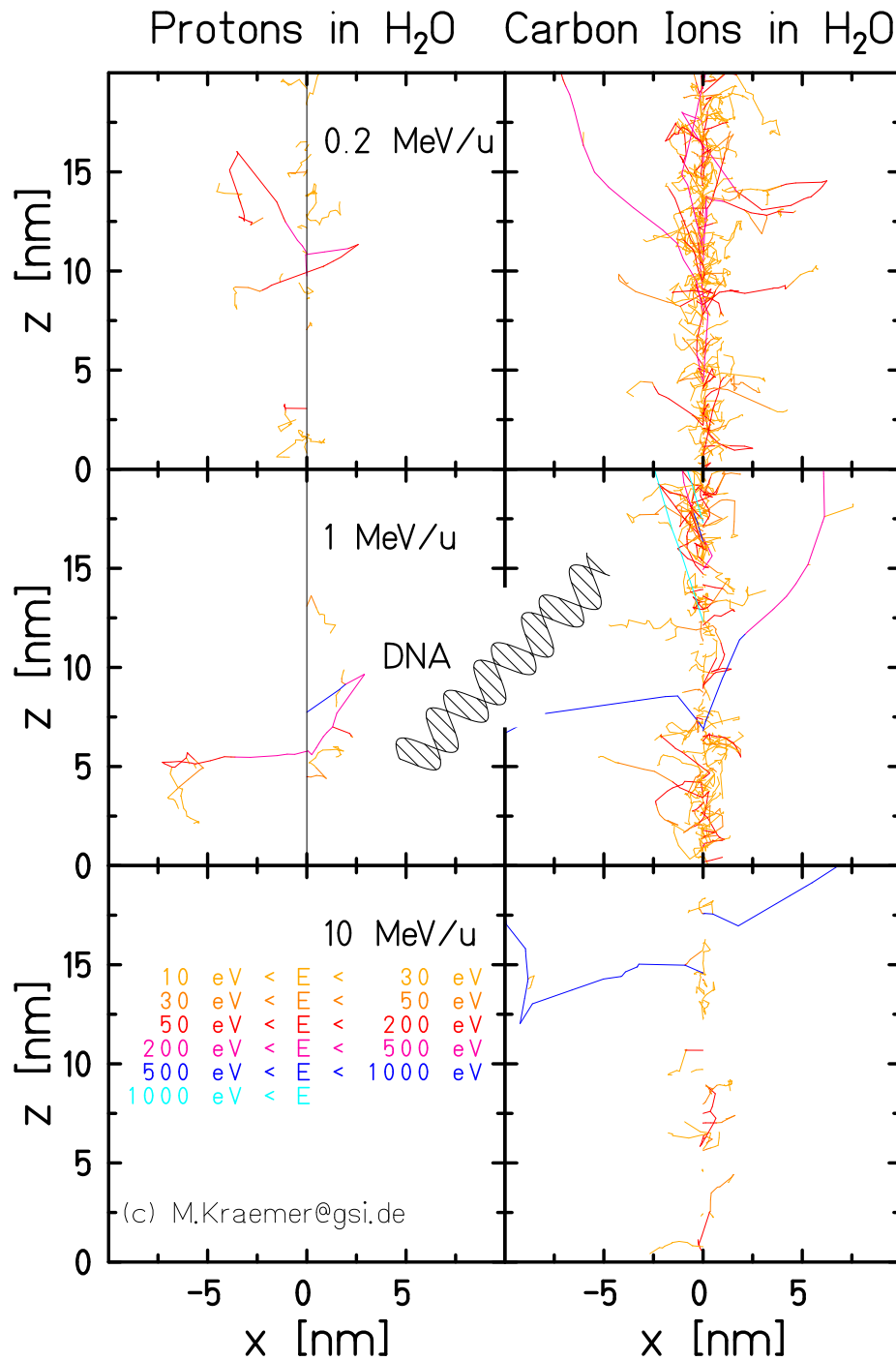


Figure 1.5.: Microscopic track structure comparing protons and carbon ions at different energies. While protons and high energetic carbon ions are sparsely ionizing irradiation carbon ions at low energies show a high density of ionization events close to the particle track. Thus, they are considered as densely ionizing radiation. The size of a DNA is provided for comparison. Figure courtesy of Michael Krämer.

1.2 Radiobiology

Photons in the energy regime used for radiotherapy as well as ions are ionizing radiation. The beam's energy is in both cases mainly deposited by ionization events. The electrons produced can cause subsequent ionizations. These ionizations damage biological structures like a cell's DNA. DNA is the carrier of genetic information in living organisms. It is therefore considered to be the critical target in radiotherapy. In eukaryotic cells¹ most of the DNA is within the cell nucleus. A single DNA strand comprises the backbone made of phosphate and sugar residues as well as bases attached to the sugar/phosphate group. In DNA four different bases can be found: adenine (A), cytosine (C), guanine (G) and thymine (T). The sequence of these bases along a strand encodes the genetic information. DNA normally appears as a double helix formed by two single strands. Base pairs are formed along the double helix each consisting of one base from each of the two strands. Pairs are always formed by either A and T or C and G. Thus, for an existing single strand the partner single strand to form a double helix is predetermined. This means there is redundancy in the cell's genetic information. This redundancy is important e.g., for repair processes and DNA replication. The genetic information is distributed among chromosomes, each consisting of one long DNA double helix. The length of the DNA double strand of a single chromosome can easily be several centimeters. It only fits into a cell nucleus because it is packed on several structural levels (see Figure 1.6).

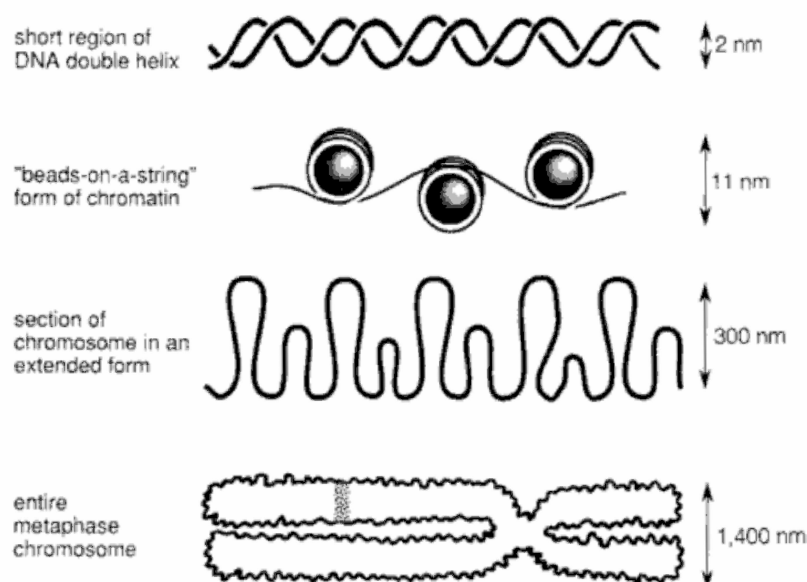


Figure 1.6.: Different levels of DNA organization. The DNA double helix is packed on several levels. Thus, several double strands each with a length in the order of cm fit within the cell nucleus. Figure from (Hall and Giaccia, 2006).

¹ Eukaryotic cells have a cell nucleus e.g., most human cells.

Several types of DNA damage can be caused by ionizing radiation. The most important ones are shown in Figure 1.7. The space between the two strands is around 2 nm (see Figure 1.6 on the facing page). Thus electrons with a mean free path on this length scale are most effective in introducing more double strand breaks. Cells have developed several countermeasures in case

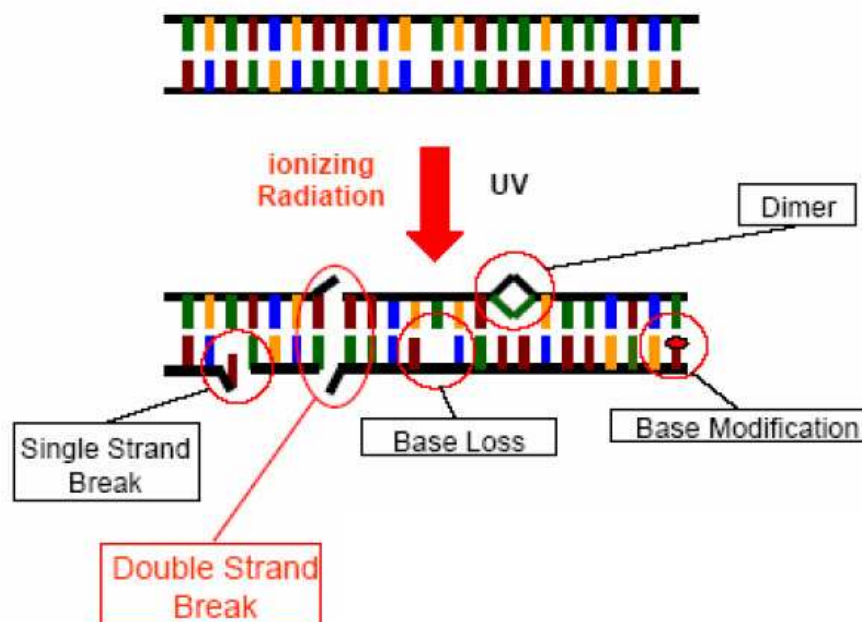


Figure 1.7.: DNA damage caused by ionizing radiation. Single-strand breaks and base damage are considered as elementary lesions. Two elementary lesions closer than ≈ 20 base pairs form a simple clustered lesion, e.g., a double-strand break. Complex clustered lesions (not drawn) are formed by three or more elementary lesions.

DNA damage is detected. Different repair mechanisms are available which are very effective in repairing especially less complex lesions. In case of irreparable damage a controlled pathway to self-inactivation, called apoptosis, is activated. In this case the remainder of the cell is removed by cells of the immune system. Apoptosis usually is the preferred pathway of tumor cell inactivation in radiotherapy. Other pathways like necrosis, i.e., uncontrolled destruction of the cell, typically cause more severe reactions of the immune system, e.g., inflammations. Cells are typically effective in repairing elementary lesions (i.e., single-strand breaks and base changes) or even double-strand breaks, i.e., two single-strand breaks within ≈ 20 base pairs. As more complex damages² are involved, the probability for induction of an irreparable lesion eventually leading to cell death is increased. At the same dose level the probability to induce complex damages varies depending on the local energy deposition pattern. The critical measure is the linear energy transfer (LET). It is defined as the energy locally deposited per unit path

² A complex damage is defined as a damage comprising three or more elementary lesions.

length and typically given in keV/μm. Photons, protons as well as fast ions³ are considered to be sparsely ionizing radiation with a low LET while slow ions are considered densely ionizing radiation with a high LET. To quantify an increased biological effectiveness the measure relative biological effectiveness (RBE) is introduced. It is defined as follows:

$$\text{RBE} = \frac{D_{\text{photon}}}{D_{\text{test}}} \Big|_{\text{iso-effect}} \quad (1.13)$$

where D_{photon} denotes the absorbed photon dose necessary to obtain a certain iso-effect and D_{test} is the absorbed dose of a test radiation, e.g., ions at a defined energy, leading to the same iso-effect.

Assuming a given fluence of one ion species, with increasing LET the probability to induce cell killing⁴ increases but at the same time also the locally deposited dose increases. For LET values below a certain threshold the increase in dose is over-compensated by the increased cell killing. Therefore, for this LET regime the RBE increases with increasing LET. Around this threshold, typically lying between 100 keV/μm and 200 keV/μm, the deposited dose is most effective in inducing cell killing while at even higher LET the increase in local dose deposition outweighs the additional cell killing. The RBE consequently decreases again with further increasing LET. This effect is known as overkill effect. The RBE dependence on LET for carbon ions is shown in Figure 1.8 on the next page.

The RBE dependencies are complex. Besides the introduced dependency on LET the RBE also depends on other factors like projectile, tissue or cell type, end point and dose level. The dependence on end point and dose is illustrated in Figure 1.9 on the facing page.

1.2.1 Radiobiological modeling

For radiotherapy a quantitative understanding of the biological radiation response is needed. A complete simulation of dose deposition and subsequent biological processes eventually leading to cell death is currently not achievable. This is due to the huge complexity and the limited understanding of the vast amount of biological processes. Thus, current radiotherapy relies on models. After introducing the linear-quadratic model often used to describe cell survival curves (Hall and Giaccia, 2006), one radiobiological model, the local effect model (LEM), developed by Scholz et al. (Scholz and Kraft, 1996), will be introduced.

³ If not stated otherwise here and in the following ions refers to ions of interest for external radiotherapy. These are usually elements of the periodic table's first two periods.

⁴ The following is also true for many other end points.

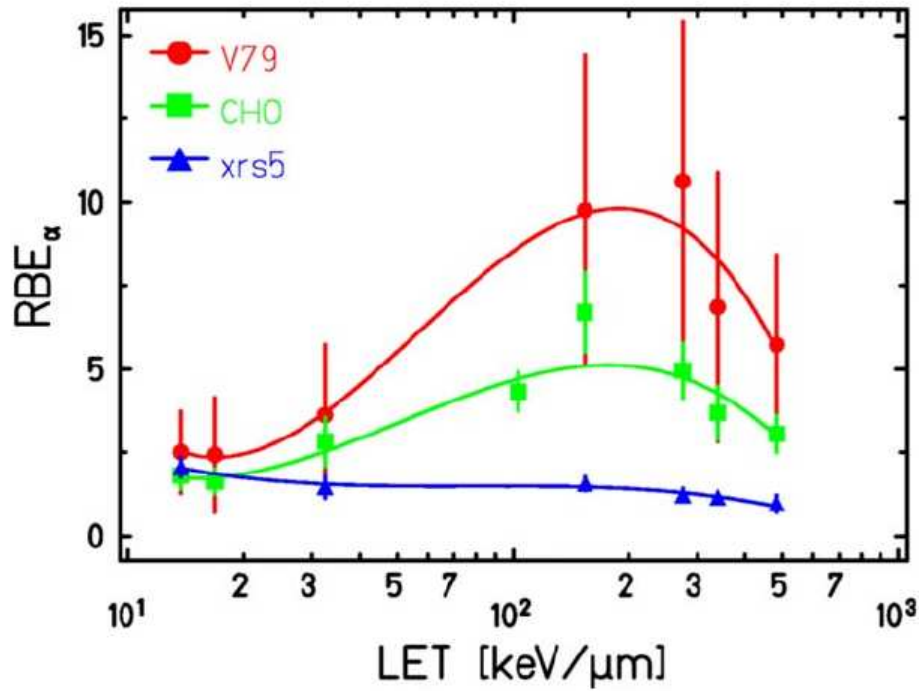


Figure 1.8.: RBE_{α} dependence on LET. RBE_{α} denotes the initial RBE. A rise of the RBE with increasing LET can be seen but around an LET of $200 \text{ keV}/\mu\text{m}$, the RBE peaks and drops again if LET is further increased. The xrs5 cell line is a repair deficient cell line. Figure from (Schardt et al., 2010). Experimental data from (Weyrather et al., 1999).

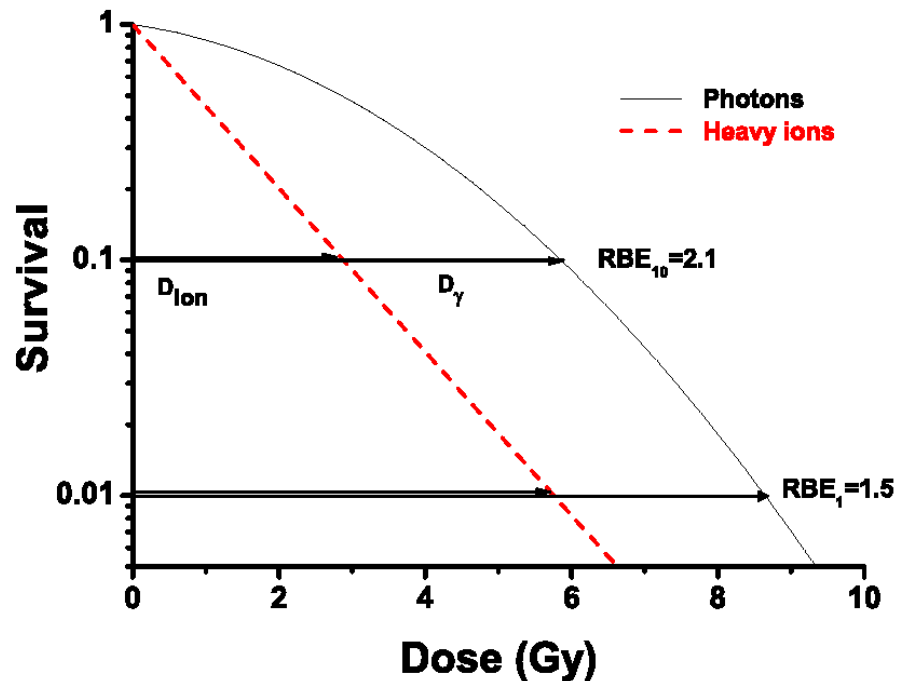


Figure 1.9.: Typical dose response curves for photon and heavy ion irradiation. Depending on the end point (here survival of 0.1 and survival of 0.01, respectively) the RBE changes. Thus, the RBE for high doses is lower than the RBE for small doses. Figure from (Schardt et al., 2010).

Linear-quadratic model

The dose response for cell killing is often described using an exponential function with a linear-quadratic exponent. For high doses experimental data suggest that a purely linear-quadratic model overestimates the cell killing. Some models thus introduce a threshold dose D_t above which the response curve is purely exponential:

$$S = \begin{cases} e^{\alpha D + \beta D^2} : & D \leq D_t \\ S_t e^{s(D - D_t)} : & D > D_t, \end{cases} \quad (1.14)$$

where α and β are the linear-quadratic parameters, S_t is the survival at D_t and s is the curve's slope at D_t . The linear-quadratic model with this extension will in this work be referred to as the linear-quadratic-linear model. Depending on the chosen parameters the dose response curve exhibit a more or less pronounced shoulder shape 1.10 on the next page.

Local effect model

The basic idea of LEM is to separate the physical part and the biological part. As mentioned above the biological part is very difficult to simulate. LEM includes the biological effects by taking dose response curves for photon radiation into account. LEM assumes that the biological response to a local dose deposition does not depend on the primary radiation quality (e.g., photon or ion radiation). This assumption is justified by the final interaction mechanisms described in Section 1.1. For photons as well as ions the final step in dose deposition is interaction of secondary electrons with the target material. The different response to the same overall dose apparent when introducing the RBE formalism thus has to be caused by differences in local dose deposition. The local dose distribution is purely physical and can be modeled reasonably well. For the calculation of cell survival the cell nucleus containing the DNA is the critical structure. LEM models the local dose deposition in small subvolumes of the cell nucleus based on Monte Carlo simulations and determines the survival level by integration over the nucleus' volume taking into account photon dose response curves. These curves need to be extrapolated as in ion radiation local doses close to the ion track can be extremely large.

Different improvements have been implemented to improve LEM. One main extension was the consideration of clustered single strand breaks effectively leading to additional double strand breaks (Elsässer and Scholz, 2007). A further development was the implementation of an energy dependent track radius leading to a further improved description of measured data. The most recent LEM implementation is based on an analysis of the distribution pattern of double strand

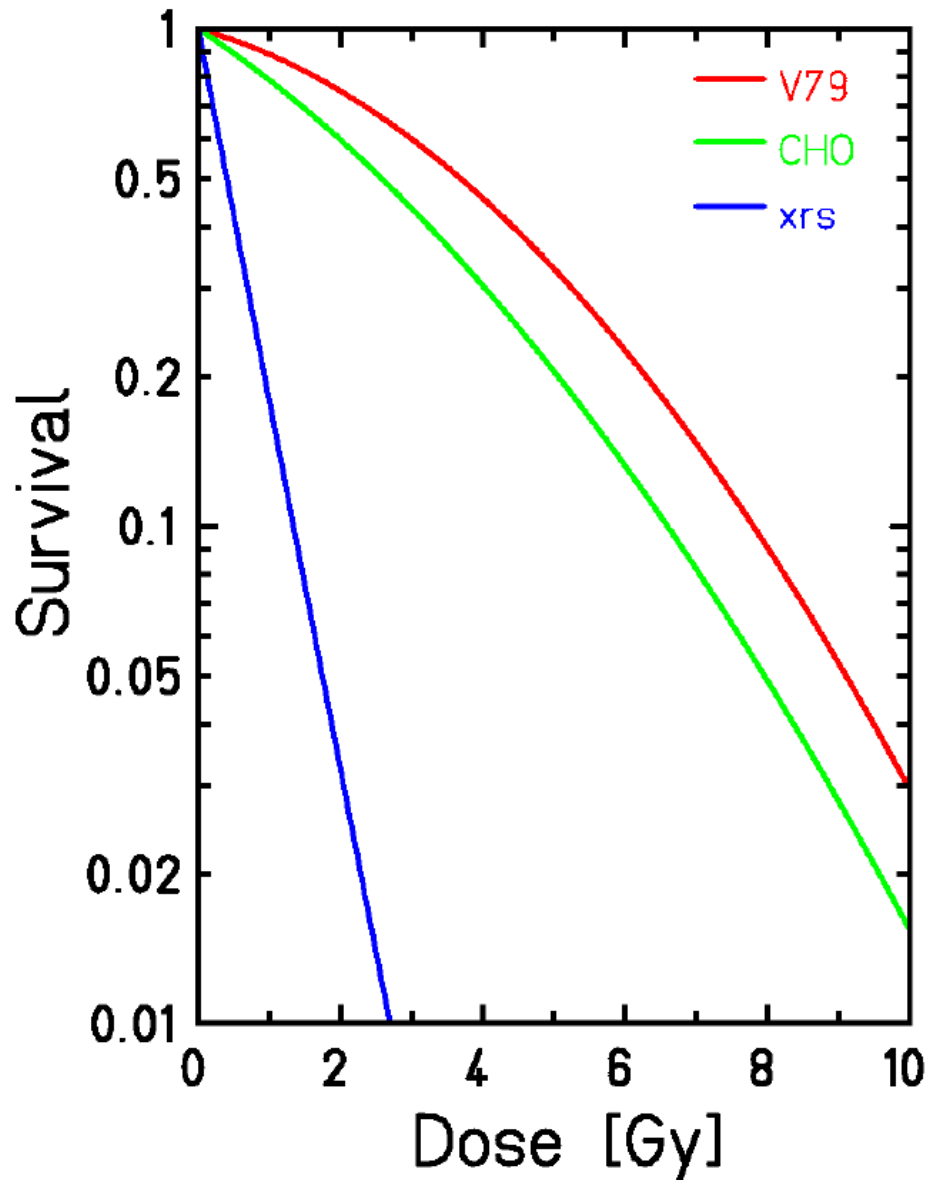


Figure 1.10.: Dose response curves after x-ray irradiation. Different cell lines exhibit different combinations of α and β values. Thus, the shape of the dose response curve differs. Repair deficient cell lines, here xrs5, show a nearly straight survival curve while other cell lines show a more pronounced shoulder. Figure from (Schardt et al., 2010). Data from (Weyrather et al., 1999).

breaks. These distributions are analyzed with respect to their proximity (Elsässer et al., 2010; Friedrich et al., 2012). Thus, this approach provides a more mechanistic description of the biological effects in response to ion radiation.

1.2.2 Radiation response

There are several factors modifying the radiation response. A genetic predisposition is suggested, e.g., by the study of Flint-Richter and Sadetzki (Flint-Richter and Sadetzki, 2007). Other factors include cellular status like oxygenation level and cell cycle state. An assessment of these factors and a prediction of the individual sensitivity is very challenging and currently not in clinical routine for radiotherapy.

Fractionation

Another factor modifying the radiation response is depending on the delivery scheme. When the therapeutic dose is not delivered at once but within a fractionation scheme, the biological response is altered.

Applying the linear-quadratic model the effect E , e.g., logarithmic cell killing, of a single dose D can be written as:

$$E_1 = \alpha D + \beta D^2. \quad (1.15)$$

Typically one fraction is applied per day. After one day repair processes can be considered to be completed. In that case for a fractionated treatment with n fractions and fraction dose d the effect E_n can be written assuming n independent treatments:

$$E_n = n (\alpha d + \beta d^2) \quad (1.16)$$

$$= \alpha (nd) \left(1 + \frac{d}{\alpha/\beta} \right). \quad (1.17)$$

The biologically effective dose (BED) is often used to compare different fractionation schemes and is defined as:

$$\frac{E_n}{\alpha} = nd \left(1 + \frac{d}{\alpha/\beta} \right). \quad (1.18)$$

Equation 1.15 can be written as:

$$\frac{E_1}{\alpha} = D \left(1 + \frac{D}{\alpha/\beta} \right). \quad (1.19)$$

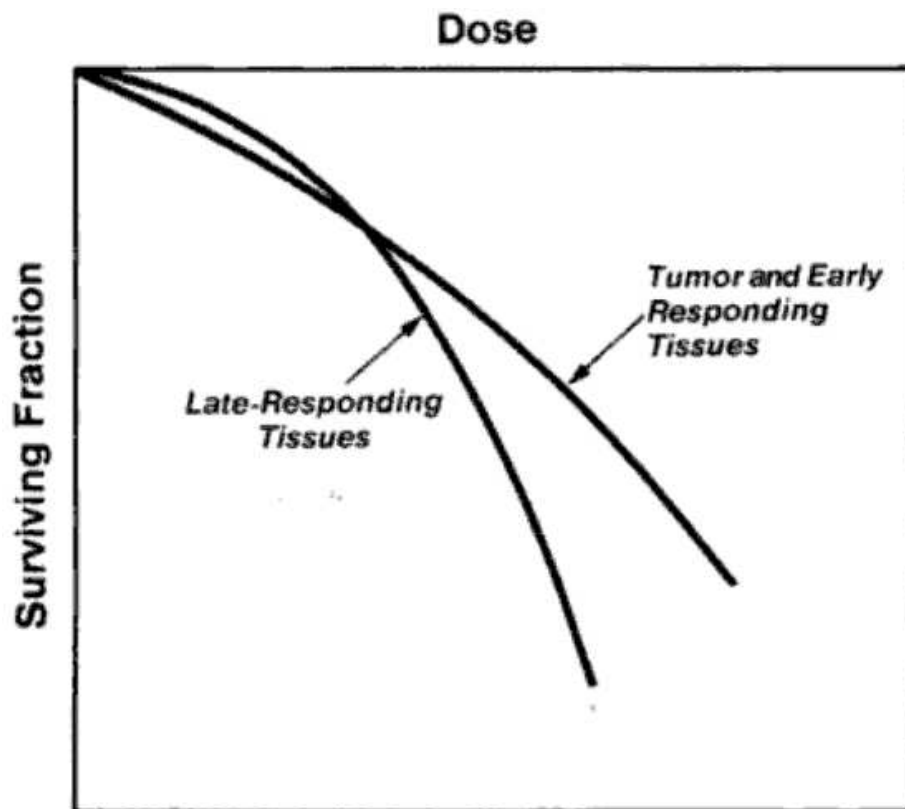


Figure 1.11.: Dose response for late responding tissue and early responding tissue. Late responding tissue shows a more pronounced shoulder as the α/β is relatively small and thus the quadratic dose term is important already at low doses. Tumors typically behave like early responding tissue. Figure from (Hall and Giaccia, 2006).

Comparing Equation 1.19 on the preceding page and Equation 1.18 on the facing page, it can be easily seen that the biological effect of a dose $D = nd$ is always largest for a single dose application. Thus, fractionation results in a smaller effect after application of the same cumulative dose. Depending on the shape of the dose response curve the effect of fractionation is more or less pronounced.

Tissue effects can be categorized in early effects that are typically already apparent during the course of radiotherapy and late effects that appear after months or even years. Survival of tumor cells is clonogenic survival, i.e., a tumor cell is considered dead if it is not able to proliferate⁵. Clonogenic survival tends, like early responding tissue, to exhibit a large α/β ratio implicating a less pronounced bending. Organ functioning, in contrast, is rather related to functional survival showing a more pronounced shoulder in radiation response due to a relatively small α/β ratio (Hall and Giaccia, 2006). Thus, normal tissue surrounding the tumor and organs at risk (OARs) close to the tumor typically exhibit a relatively small α/β . This is illustrated in Figure 1.11. The main rationale for fractionation is the differential response to fractionation of typical tumor compared to typical normal tissues and OAR: Late responding

⁵ Precisely, cells able to form colonies with more than 50 cells are considered clonogenic survivors.

tissue profits stronger from fractionation than early responding tissue and most tumors do. This tendency for different α/β ratios can already be seen from Equation 1.18 on page 26. Thus, fractionation allows to reduce the probability for late effects while largely maintaining tumor response.

1.3 Photon therapy

After the discovery of x-rays by Röntgen in 1895 the first photon treatment was already conducted in 1897 (Freund, 1897). First photon treatments used x-ray tubes and radioactive sources (e.g., radium sources) providing photons in the keV range. Increasing the photon energy allows more effective treatment of deeper seated tumors (see photon depth dose curves in Figure 1.4 on page 18). The effort to increase photon energy lead to the introduction of ^{60}Co sources emitting photons with 1.17 MeV and 1.33 MeV and eventually linear accelerators. In these linear accelerators electrons are accelerated and hit a target. The emitted bremsstrahlung is used for therapy. State of the art are medical linear accelerators delivering photon spectra in the megavolt (MV)⁶ regime. Until today, for the majority of radiotherapy treatments photons are used.

Not only the photon energy spectrum but also the application technique itself has a major impact on tumor conformity. The medical advances in photon therapy have been reviewed by Bucci et al. (Bucci et al., 2005). In conventional photon therapy treatment fields could only be conformed to the lateral tumor shape, resulting in substantial dose delivery to healthy tissue. The introduction of 3D imaging techniques, e.g., computed tomography (CT) and positron emission tomography (PET), allowed to assess the tumor shape in all three dimensions and subsequently better conform the photon fields to the 3D contour of the tumor. In combination with dedicated treatment planning algorithms, this method is called 3D conformal therapy. However, the amount of conformity was still limited as only single static fields were used.

Intensity modulated radiotherapy (IMRT) has strongly improved achievable dose distributions in photon therapy (IMRT Collaborative Working Group, 2001). In IMRT, many small beamlets with varying intensities are delivered from different beam angles. The beamlets are shaped by multileaf collimators (MLC). A sketch of an intensity modulated beam application using a MLC is shown in Figure 1.12 on the facing page. This technique introduces new degrees of freedom that lead, in combination with dedicated treatment plan optimization, to much conformer dose distributions with superior OAR sparing if compared to conventional and 3D conformal photon therapy. The dosimetric advancement of IMRT in comparison to conventional therapy is exemplary shown in Figure 1.13 on the next page. Different implementations of IMRT are available. Most commonly, the linear accelerator is mounted on a gantry that allows to deliver the treatment beam from different angles.

⁶ For linear accelerators the photons energy spectrum is usually described by a voltage unit not an energy unit.

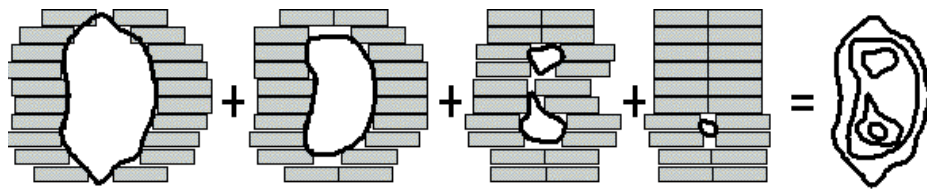


Figure 1.12.: Principle of IMRT. The multileaf collimator is used to conform the photon field to the target extent. Different positions of the single leaves allow for an intensity modulated radiation field. Figure from (Schlegel and Mahr, 2001).

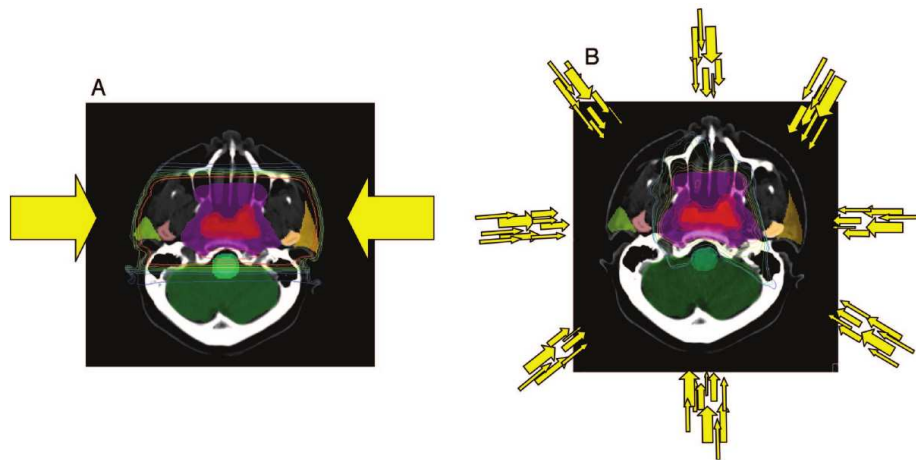


Figure 1.13.: Comparison of dose distributions for conventional therapy using two treatment fields and IMRT therapy. In conventional therapy treatment fields can only be conformed to the lateral tumor extent. Field intensities are constant. IMRT in contrast uses more field angles and varying intensities per field. The dose distribution can be adapted to the tumor shape in all three dimensions. Clearly superior tumor conformity can be achieved with IMRT. Tumor coverage is achieved for both techniques but normal tissue sparing is much better for IMRT (see the iso dose lines). Figure from (Bucci et al., 2005).

Two particular implementations are introduced here as they will be of importance later in this work.

TomoTherapy TomoTherapy is an implementation where the linear accelerator for IMRT treatment is mounted on a ring (Mackie et al., 1993). Like a CT, the accelerator can move around the patient enabling beam delivery from all possible beam angles (360°). Together with a linear couch motion, spiral beam delivery can be achieved. Thus, also large treatment fields can be irradiated at once. The system can be seen in Figure 1.14 on the facing page.

Cyberknife The Cyberknife system comprises a linear accelerator mounted on a robotic arm (Kilby et al., 2010). Thus, this system offers a large freedom in the choice of treatment ports. Of special importance for the treatment of moving tumors is the Synchrony extension of the Cyberknife system. The Synchrony system provides adaptation of the therapeutic beam position to the changing tumor position. Two basic requirements have to be met for fast beam adaptation. A flexible beam delivery unit allowing for fast beam position adaptations and a motion monitoring system assessing tumor motion. The flexibility of beam delivery is guaranteed by the robotic arm. Motion monitoring is achieved by a combination of external motion monitoring using a camera system and infrared markers as well as internal motion monitoring using x-ray fluoroscopy. The system is shown in Figure 1.15 on the next page. Tumor motion as well as its monitoring and techniques to mitigate its influence will be discussed in more detail in Section 1.5.



Figure 1.14.: TomoTherapy treatment unit. The system comprises a linear accelerator mounted on a ring around a movable patient couch. The setup is comparable to a CT mounting. Full 360° treatment angles are available. Together with couch motion spiral beam delivery can be used, e.g., for large treatment fields. Figure courtesy of Accuray Inc.



Figure 1.15.: Cyberknife Synchrony system. The linear accelerator is mounted on a robotic arm. Motion monitoring for mobile tumors is performed with a combination of external imaging using infrared markers and a camera system (ceiling-mounted, left device) and internal imaging using x-ray fluoroscopy (two ceiling mounted x-ray tubes and two detector panels integrated to the floor). Figure courtesy of Accuray Inc.

1.4 Ion therapy

Even though photon therapy techniques nowadays are very advanced the unfavorable photon depth dose profile limits achievable tumor conformity. Ion beams, in contrast, have a finite range with the highest local energy deposition at the very end of the particle range, the Bragg peak, which depth can be controlled via the particle energy (see Figure 1.4 on page 18).

Based on this physical advantage Wilson proposed already in 1946 the usage of ions for tumor treatment (Wilson, 1946). It is remarkable that state of the art concepts like increased biological effectiveness, range modulator wheels, and carbon therapy have already been mentioned by Wilson. The first ion beam therapies were already performed in 1954 at Berkeley Lab (Tobias et al., 1958). First treatments have been performed using protons but from 1957 on also other ions (primarily Helium ions) have been employed exploring the efficacy of heavier ions.

As in photon treatment, also in ion treatment several improvements lead to more conformal dose depositions. Improvements concern, e.g., the choice of the projectile ions as well as more sophisticated beam delivery methods.

1.4.1 Projectile ion

Already in Berkeley heavier ions have been used for therapy. Heavier ions provide preferable physical as well as biological properties. Physical properties include reduced lateral scattering of heavier ions. According to Molière (Molière, 1948) the scattering angle's root mean square is approximately inversely proportional to the projectile's momentum. Thus, the use of heavier ions like carbon enables sharper lateral penumbras of the dose distribution. These are of particular importance if an OAR is close to the tumor.

Besides this physical advantage, heavier ions also provide increased biological effectiveness. This increased effectiveness is caused by a different track structure of heavier ions. While photons as well as protons and fast heavier ions are considered as sparsely ionizing low LET radiation, heavier ions at low energies are densely ionizing high LET radiation. In Section 1.2 the relation between RBE and LET has been described. When choosing the therapeutic ion species, ions for which the Bragg peak region coincides with the most effective LET region, are to be preferred (Krämer et al., 2003). Due to the z_{eff}^2 dependence of the Bethe equation (see Equation 1.6 on page 14), light ions reach the most effective LET only in the very distal part of the Bragg peak resulting in a relatively low average RBE in the spread out Bragg peak (SOBP). Very heavy ions in contrast reach the most effective LET region already in the entrance channel.

It is important to realize that an increased biological effectiveness is only advantageous for therapy if it is differential, i.e., if the increase is more pronounced in the tumor tissue than in the normal tissue. While for protons only the very distal Bragg exhibits an elevated RBE and

thus the average RBE of the SOBP is virtually the same as for the plateau region⁷ ions heavier than oxygen have the highest RBE in the proximal part of the Bragg peak or, for even heavier ions, already in the plateau of the depth dose distribution (Krämer et al., 2003).

Carbon ions are biologically most effective in the Bragg peak region and thus physical and biological advantages coincide. For a typical treatment situation with carbon ions the average LET in the tumor region is larger than the LET in the entrance channel where typically normal tissue is affected.

Besides the choice of the projectile ion, also the application technique has a large influence on resulting dose distributions.

1.4.2 Application technique

First treatments in Berkeley were performed by shooting the proton beam through the complete patient head (Tobias et al., 1958). Passive beam delivery uses the Bragg peak region of the beam for dose coverage of the tumor (Koehler et al., 1975, 1977). In this technique, the beam delivered by the accelerator is scattered. This broad beam's energy spectrum is subsequently widened by a range modulator, e.g., a modulator wheel⁸ or a ridge filter, to deliver a SOBP covering the tumor extent (typically plus margins) in longitudinal direction. The weights of the different energies in the SOBP are optimized such that a typically constant (RBE weighted) dose level is delivered to the whole SOBP. Conformity to the distal tumor border is achieved by a compensator while a collimator is used for collimation in the lateral plane. The proximal border of the tumor can not be directly shaped in this approach as the width of the SOBP is fixed by the energy modulator to the largest longitudinal tumor extent. For lateral positions where the longitudinal tumor extent is smaller the target dose is pulled to the tissue proximal to the target. A sketch of a static delivery system is shown in Figure 1.16 on the following page

One of the major improvements was the introduction of beam scanning (Haberer et al., 1993; Pedroni et al., 1995). In contrast to passive beam delivery techniques, beam scanning is considered as active beam delivery. Instead of passive beam shaping material a large number of small pencil beams (full width at half maximum (FWHM) typically several mm) delivered by an accelerator are used to conform the dose distribution to the tumor extent. These pencil beams can be positioned laterally by magnetic deflection or patient couch movement as well as in depth by choosing a suitable energy. An example of a scanning delivery system is shown in Figure 1.17 on page 35.

In longitudinal direction the tumor is divided into iso-energy slices with, e.g., 3 mm_{H₂O} spacing. An iso-energy slice (IES) is the entity of beam positions with a common energy. Obviously

⁷ Clinically, a constant proton RBE of 1.1 is used.

⁸ A modulator wheel is a fast rotating wheel with variable thickness. Depending on the wheel position the energy adaptation changes resulting in a broadening of the energy spectrum.

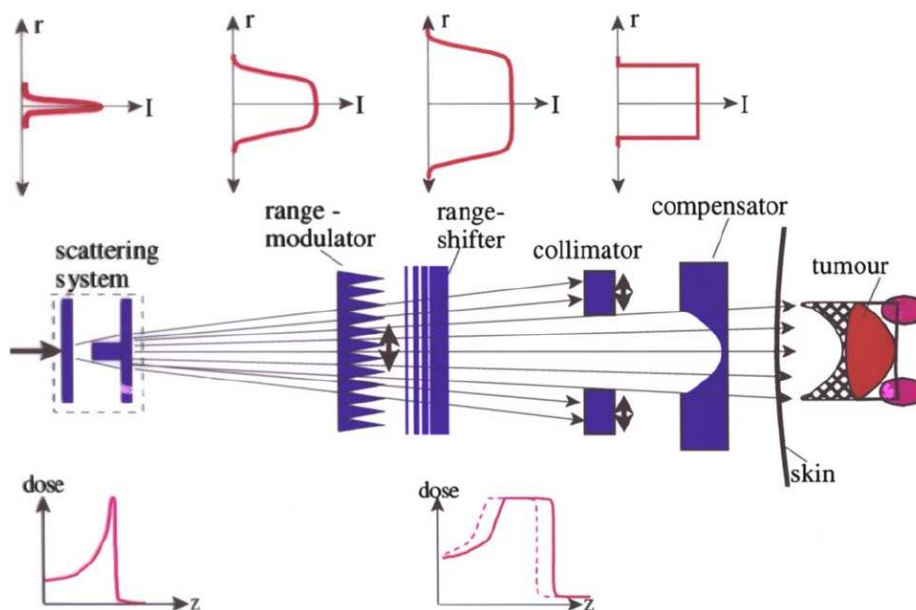


Figure 1.16.: Passive beam delivery system. The thin beam delivered by the accelerator is broadened by a scattering system. The width of the SOBP can be adjusted by the range modulator (here a ridge filter) widening the energy spectrum. A range shifter shifts the spectrum to the desired depth. Lateral and distal conformity are achieved by a collimator and a compensator, respectively. The proximal field border can not be shaped as the width of the SOBP is fixed by the range modulator. Thus, the dose distribution is pulled to the proximal part of the target volume. The transversal beam shape as well as the longitudinal dose distribution are additionally shown. Figure from (Schardt et al., 2010).

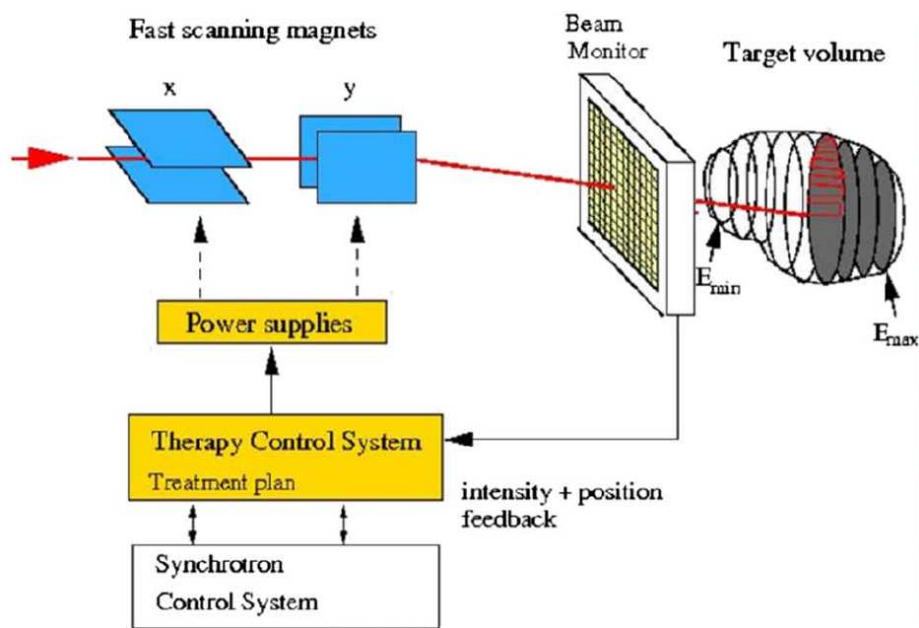


Figure 1.17.: Scanning beam delivery system. Two pairs of scanning magnets are employed to scan the pencil beam over one IES. A beam monitor system feeds beam position and intensity back to the TCS. The TCS steers the magnets via their power supplies to switch to the next beam position as soon as the nominal particle number from the treatment plan is reached. The beam energy matching the next IES to form the SOBP is actively requested from the synchrotron control system. Scanning systems are also used in combination with cyclotrons. In this case, energy changes are typically achieved by inserting absorber material into the beam line. Figure from (Schardt et al., 2010).

the definition of IES depends on the field angle. The IES concept takes into account particle range instead of geometrical depth. Hence positions belonging to the same IES might have very different geometrical depths but rather share the same radiological or water equivalent depth. The water equivalent depth of a position given in $\text{mm}|_{\text{H}_2\text{O}}$ is the depth particles stopping at that position would have reached in water. By overlaying beams with different energies a SOBP can be formed for scanned beam systems. An example is shown in Figure 1.18. Lateral tumor

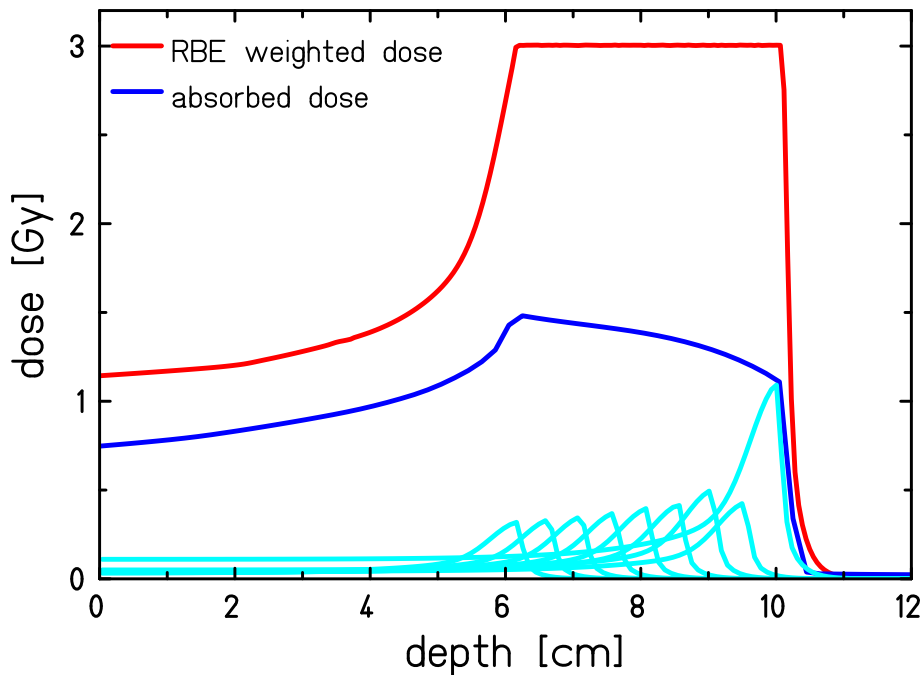


Figure 1.18.: SOBP for a scanned beam. Several Bragg peaks with different energies are overlaid to deliver a flat RBE weighted dose to the target area. Also shown is the corresponding absorbed dose that is not flat in the target area as the RBE is not constant throughout the SOBP but depends e.g., on LET. Figure courtesy of Michael Scholz.

conformity within one iso-energy slice is achieved by overlaying many pencil beams of the same energy. The Bragg Peak of each pencil beam represents one beam position.

Different scanning flavors exist, e.g., spot scanning (Pedroni et al., 1995) and raster scanning (Haberer et al., 1993; Furukawa et al., 2007). While in spot scanning the beam is switched off between two beam positions raster scanning works in continuous mode, i.e., beam is not switched off between beam positions. Compared to their FWHM the spacing of beam positions is smaller for raster scanning what makes dose distributions more robust. Lateral deflection relative to the patient is typically achieved by magnets or a combination of magnets and patient couch motion. The SOBP covering the tumor extent in the longitudinal direction is formed by overlaying many IESs. Scanning methods allow improved tumor conformity when compared to passive beam delivery as each IES can be laterally shaped. Especially the proximal tumor border coverage is typically more conformal as the width of the SOBP for scanning techniques is not fixed for the whole lateral tumor extent.

1.4.3 Treatment planning

The goal of treatment planning is to find machine parameters that ensure delivery of the prescribed dose to the tumor. At the same time, OAR dose constraints have to be met. While this basic principle is true for all kinds of radiotherapy techniques, in the following the focus will be on scanned particle beam techniques.

Scanning techniques in particle treatments have a large number of degrees of freedom. Typical treatment plans can easily comprise several thousand or ten thousand beam positions. For each beam position, an individual particle number to deliver has to be determined such that a predescribed, typically flat, overall (RBE weighted) dose distribution to the tumor is obtained.

Treatment planning is based on patient imaging data. In particle therapy, CT data is used because it represents photon attenuation that can be converted into water-equivalent depth. Other imaging methods like magnetic resonance imaging (MRI) or PET provide complementary information and are often used to support, e.g., tumor delineation. Once the images are obtained, tumor and OARs are delineated and tumor dose as well as OAR dose constraints are defined. For tumor delineation, different volumes are defined by the international commission on radiation units and measurements (ICRU) in different reports. ICRU report 50 defines the gross tumor volume gross tumor volume (GTV), the clinical target volume (CTV), and the planning target volume (PTV) for photon treatments as follows (ICRU, 1993a):

GTV "The Gross Tumor Volume (GTV) is the gross palpable or visible/demonstrable extent and location of the malignant growth."

CTV "The Clinical Target Volume (CTV) is a tissue volume that contains a GTV and/or subclinical microscopic malignant disease, which has to be eliminated. This volume thus has to be treated adequately in order to achieve the aim of therapy: cure or palliation."

PTV "The Planning Target Volume (PTV) is a geometrical concept, and it is defined to select appropriate beam sizes and beam arrangements, taking into consideration the net effect of all the possible geometrical variations and inaccuracies in order to ensure that the prescribed dose is actually absorbed in the CTV."

These three volumes are shown for a lung cancer patient in Figure 1.19 on the next page.

In ICRU report 62, a supplement to report 50, the ICRU defined the internal margin (IM) (ICRU, 1999):

IM "The Internal Margin, commonly asymmetric around the CTV, is intended to compensate for all movements and all variations in site, size, and shape of the organs and tissues contained or adjacent to the CTV. They may result, e.g., from respiration, different fillings of the bladder, different fillings of the rectum, swallowing, heart beat, movements of the bowel."

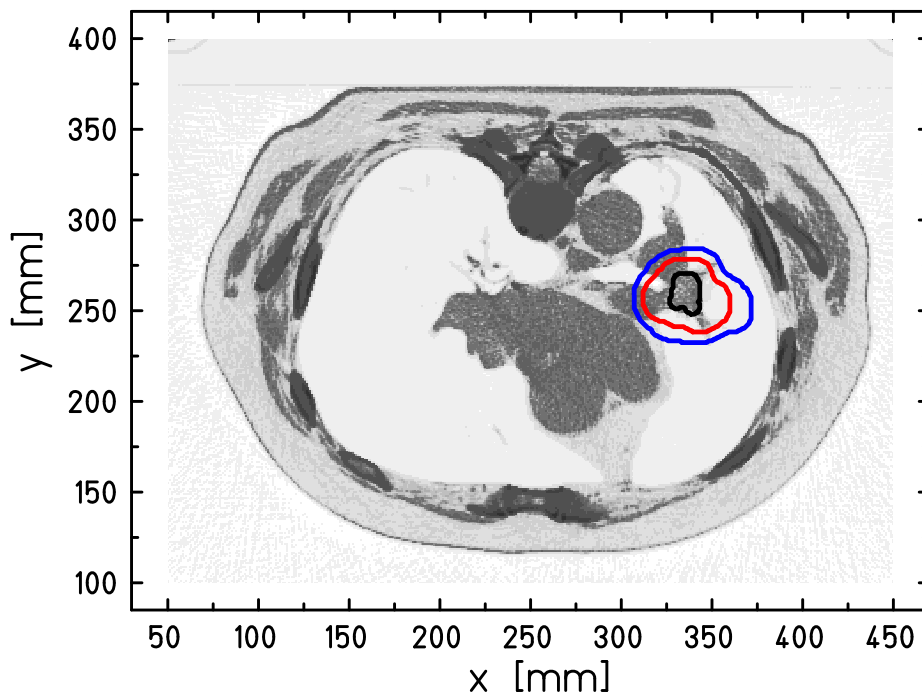


Figure 1.19.: CT slice of a lung tumor patient. GTV (black), CTV (red), and PTV (blue) contours delineated. Definitions of GTV, CTV, and PTV are given in the Section 1.4.3.

Based on this definition, the term internal target volume (ITV) is commonly used to describe the volume encompassing CTV and IM.

Another report addressing specifically proton therapy has been published by the ICRU (ICRU, 2007). As far as volumes are concerned the concepts of GTV and CTV remain unchanged as they are independent on modality. The PTV in contrast does depend on modality. Especially the longitudinal margin is crucial for proton (and other ion) therapy due to their depth dose profile. The distinctive Bragg peak structure implies an increased susceptibility to range uncertainties if particle dose distributions are compared to photon dose distributions. Drawing of the ITV contour is considered to be optional. It might not be drawn but has to be taken into account when drawing the PTV (ICRU, 2007).

After delineation, the number of fields as well as the field angles are chosen to spare OARs as well as possible. Because of their superior depth dose distribution, for particle treatments often two fields are sufficient.

In the next step the number of particles to be delivered at each beam position is optimized. Dedicated treatment planning software has been developed for that purpose. At GSI Helmholtzzentrum für Schwerionenforschung GmbH (GSI) Treatment planning for Particles (TRiP) was developed (Krämer and Scholz, 2000; Krämer et al., 2000). Optimization has to include RBE calculation. As already mentioned, RBE depends on many different factors. Within TRiP, LEM (see Section 1.2.1) is used for RBE modeling (Krämer and Scholz, 2006).

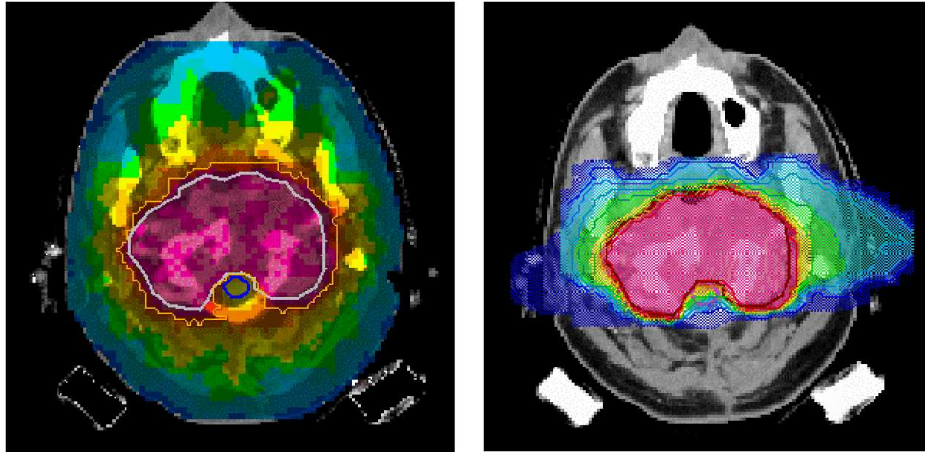


Figure 1.20.: Comparison of dose distributions achievable with IMRT (left) and scanned carbon ions (right), respectively. While both methods show a homogeneous target coverage the integral dose delivered to the patient is larger with IMRT. Especially the dose level to organs at risk close to the target e.g., the brain stem is superior if scanned carbon ions are used.

1.4.4 GSI particle therapy pilot project

At GSI a pilot project using carbon radiotherapy has been conducted between 1997 and 2008. The pilot project has been conducted in a collaboration between GSI, Heidelberg university hospital, the German cancer research center (DKFZ), and the research center Rossendorf/Dresden. In total 440 patient treatments have been performed. Mostly, tumors in the head and neck region have been treated. The usual fractionation scheme has been 20 fractions on consecutive days. Later also prostate and spinal cord tumors have been treated. The treatments have been performed using a dedicated raster scanning system (Haberer et al., 1993). Treatment planning was performed with TRiP (Krämer and Scholz, 2000; Krämer et al., 2000).

For online verification of dose delivery, an in-beam PET system has been developed (Enghardt et al., 2004). In nuclear reactions between projectile ions and target atoms β^+ emitters are produced. By reconstructing the vertices of consecutive $e^+ - e^-$ annihilations, the expected dose distribution could be verified after each fraction.

A comparison of dose distributions achievable with IMRT versus scanned carbon ions is shown in Figure 1.20.

Based on the successful pilot project the Heidelberg Ion-Beam Therapy Centre (HIT) has started clinical operation in 2009 (Haberer et al., 2004; Combs et al., 2010). The centro nazionale di adroterapia oncologica (CNAO) in Pavia, Italy started patient treatments with scanned ions in October 2011 (Amaldi, 2004).

1.5 Organ motion in radiotherapy

The organs of a patient are subject to temporal changes. That is not only true for the organs but also for a patient's tumor. As treatment planning is, like described above, based on acquired imaging information, changes in the patient anatomy not accounted for in treatment planning are likely to impair the quality of the delivered dose distribution compared to the optimized treatment plan. Hence, assessing and, if necessary, considering organ motion in treatment planning is an essential task.

In the following different types of organ motion are described. The sources for organ motion can be categorized in patient positioning related motion and motion caused by the patient's anatomy or physiology. The latter cause of motion is commonly subdivided with regard to its time scale into interfractional and intrafractional motion. An overview is given by Langen and Jones (Langen and Jones, 2001).

1.5.1 Types of organ motion

Different types of organ motion are shown in Figure 1.21 and will be described in the following.

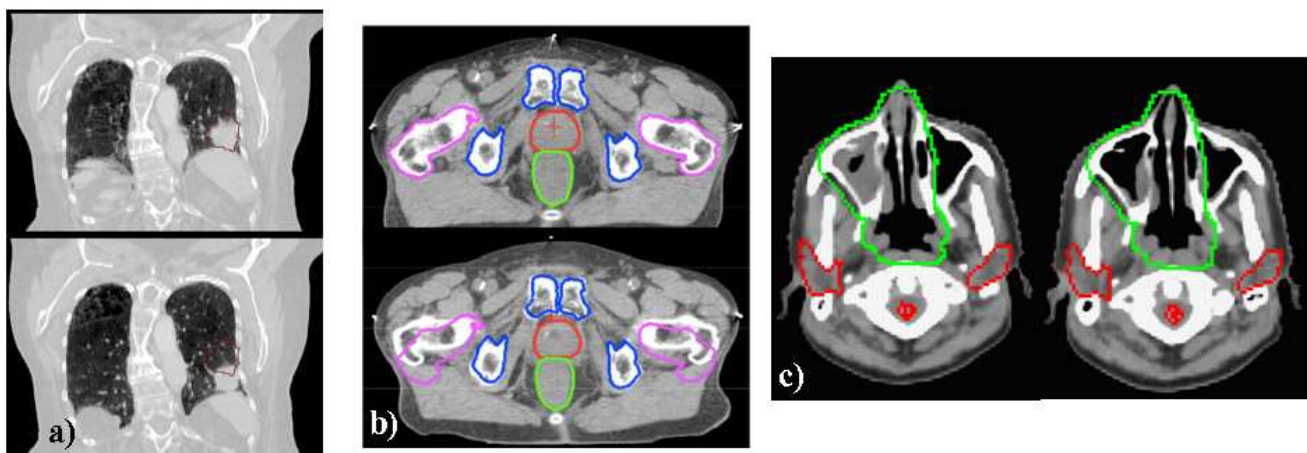


Figure 1.21.: Different types of organ motion. In a) a lung tumor is shown in two extreme motion states. This is an example for intrafractional motion. In b) two CT scans of a prostate patient are compared. Interfractional position changes are visible. In c) density variations between two CT scans are shown. Figure from (Engelsman and Bert, 2011).

Patient positioning related motion

Patient positioning related motion can occur on the interfractional as well as the intrafractional time scale. Patient positioning introduces an uncertainty of tumor position with respect to the

treatment field and can thus be considered as organ motion. While the daily variations in patient positioning between different fractions are typically random uncertainties, other uncertainties like different positioning in imaging and therapy (e.g., sitting versus lying patient position) can also introduce systematic displacements. Although typically patient fixation systems are applied residual patient movement within one fraction might play a role on the intrafractional time scale.

Interfractional motion

Interfractional motion introduces anatomic changes between different fractions of the treatment course while it is negligible within one fraction. Thus, the time scale of interfractional motion typically is hours or even days.

One type of interfractional motion is caused by physiological processes like gut and bladder filling or bowel movement. Organs subject to this kind of interfractional motion are, e.g., organs of the abdomen like prostate, intestine, and bladder.

Changes in the breathing motion pattern between fractions are observed. Sonke et al. report that the motion trajectory of lung tumors is often reproducible but the base line of the motion might be subject to considerable interfractional changes (Sonke et al., 2008).

Not only position or motion of the tumor but the extent of the tumor entity itself might be subject to changes during the course of radiotherapy. Tumor shrinkage has been observed e.g., for lung tumors by Erridge et al. (Erridge et al., 2003).

Density differences between different fractions are not necessarily due to organ motion but may e.g., be caused by air cavities being filled with liquid. Especially for particle beams these changes are of importance as they have a large impact on beam range (see Figure 1.21 on the facing page).

Intrafractional motion

Intrafractional motion plays a role on a much shorter time scale compared to interfractional motion. Typical time scales are seconds or minutes. The main causes of intrafractional motion are breathing and heart beat. Lung tumors and organs close to the diaphragm are especially prone to this kind of organ motion.

The amount of intrafractional lung tumor motion has been investigated by Liu et al. (Liu et al., 2007). They found that lung tumor motion is most prominent in the superior-inferior (SI) direction. The average motion amount in their patient cohort was found to be 0.50 cm, 0.12 cm, and 0.21 cm in the superior-inferior (SI), lateral, and anterior-posterior (AP) direction, respectively. Identified factors significantly influencing the motion amount in this study were

T staging of the tumor (Edge et al., 2009), GTV size, and fractional tumor location in the SI direction.

1.5.2 Motion acquisition

4DCT

Like described in section 1.4.3, typically CT information is used for particle therapy treatment planning. If the tumor site is subject to intrafractional motion, acquisition of a CT leads to a blurred image. More precise information about the moving tumor is provided by time resolved computed tomography (4DCT) (Low et al., 2003; Rietzel et al., 2005b). For this technique a motion signal is recorded during the CT scan. The motion trace is divided into a set of motion states each representing a different anatomical state within the (cyclic) patient motion. CT image projections are sorted into different bins according to the motion state they have been acquired in. Thus, a series of quasi-static 3D images each representing a different motion state of the whole motion cycle can be reconstructed.

Motion monitoring

The assessment of intrafractional motion is relevant, e.g., for 4DCT image sorting as well as the application of motion mitigation techniques (these techniques will be described in Section 1.5.3). Different techniques are available and are reviewed by Evans et al. (Evans, 2008).

The acquired motion signals can be categorized in direct measurements and surrogate signals. Direct tumor position measurements are, e.g., fluoroscopy and tracking of electromagnetic transponders implanted in or nearby the tumor. Surrogate signals demand knowledge concerning a correlation function to obtain the tumor position.

Implanted fiducial markers can facilitate precise tumor localization for fluoroscopy (Shirato et al., 2003). But as the implantation poses an additional risk for the patient and possibly comprises image acquisition (e.g., CT) or dose delivery (especially for particles), fluoroscopy without implantation of fiducial markers has been proposed and is already in use (Schweikard et al., 2005; Cui et al., 2007). Electromagnetic transponder systems are, e.g., used for photon prostate treatments (Willoughby et al., 2006).

Methods using a surrogate signal are, e.g., camera systems, systems attached to the patient measuring respiratory movement, or systems measuring respiratory air. Camera systems acquire images either of the patient surface or of infrared markers attached to the patient (Bert et al., 2005; Schweikard et al., 2004). Alternatively, a motion signal can be obtained e.g., by a belt measuring expansion and contraction of the body (Li et al., 2006). Systems measuring

the patient's respiratory airflow are another option to obtain a surrogate signal for tumor motion (Kubo and Hill, 1996). All these methods are implantation-free, provide a motion signal with high frequency and deliver no additional dose to the patient. Their main drawback is the indirect tumor motion measurement that requires knowledge of the correlation between tumor position and surrogate signal.

Direct measurements and acquisition of surrogate signals can be combined. The Cyberknife Synchrony system performs *beam tracking* (BT) for photon therapy and is already in clinical use. Its motion monitoring system combines direct (fluoroscopy) and surrogate (infrared camera system) motion signals. Thus, the frequency of fluoroscopic imaging can be kept low. Fluoroscopy is used to update the correlation model of the surrogate system. The accuracy of this system has been assessed by Seppenwoolde et al. (Seppenwoolde et al., 2007).

1.5.3 Mitigation of organ motion influence

Mitigation of patient positioning related motion influence

Different countermeasures to mitigate the influence of organ motion on the treatment outcome are in clinical use or currently under investigation.

By implementing precise and reliable patient positioning and patient fixation techniques, the influence of interfractional as well as intrafractional positioning related motion can be minimized. For intra-cranial lesions patient fixation employing head masks is commonly used. The positioning accuracy using different head mask systems has been investigated in different studies (Karger et al., 2001; Tryggestad et al., 2011). In conclusion, margins of 1 mm to 2 mm are recommended to account for positioning uncertainties if the investigated mask systems are used.

Mitigation of interfractional motion influence

Repeated imaging is essential to assess interfractional motion. Based on the new imaging information dose delivery can be adapted. This is called adaptive radiotherapy (ART). Several concepts are currently investigated. One of those is the "plan of the day" approach. Several treatment plans are optimized typically before the treatment course. From this treatment plan library the best matching treatment plan is chosen after each re-imaging (Murthy et al., 2011). Also a re-optimization of the treatment plan based on the new imaging data is investigated. Especially this approach demands fast treatment plan optimization and a sophisticated clinical workflow. ART for lung tumors has been reviewed by Sonke and Belderbos (Sonke and Belderbos, 2010).

Mitigation of intrafractional motion influence

Different motion mitigation techniques to mitigate the influence of intrafractional motion are currently investigated or are already in clinical use. Intrafractional motion is particularly challenging if the dynamics of beam delivery is on the same scale as the intrafractional motion. This is the case for the current implementations of the advanced dose treatment techniques IMRT and beam scanning. The common time scale of motion and beam delivery is the cause for interference effects leading to over- and underdoses within the irradiated area. This effect is commonly referred to as interplay (Phillips et al., 1992; Jiang et al., 2003; Bert et al., 2008).

If beam delivery is not dynamic, e.g., in passive particle therapy, the interplay effect does not occur and homogeneous dose delivery to the tumor volume is achievable by irradiation of an ITV encompassing the tumor motion (ICRU, 2007). However, this approach results in increased dose deposition to the healthy tissue surrounding the tumor. Motion mitigation techniques in passive particle therapy thus do not aim at mitigating dose deteriorations inside the tumor but at reducing the required margins.

Re-scanning is also known as *re-painting*. It is applicable to beam scanning dose delivery and is based on statistical averaging of interplay patterns. This effect has already been described in 1992 by Phillips et al. (Phillips et al., 1992).

An ITV encompassing the tumor in all possible motion states is the minimal target contour. The prescribed dose is not delivered in one but in multiple scans. The overall number of particles delivered to a beam position is distributed over these scans. In the simplest approach, N scans are used and a fraction of $1/N$ of the nominal particle number is delivered per scan. Radiographic films irradiated with different numbers of re-scans are shown in Figure 1.22 on the next page.

Different flavors of *re-scanning* have been investigated by Seco et al. (Seco et al., 2009). From their studies and earlier investigations by Furukawa et al. (Furukawa et al., 2007) it is known that one of the main concerns for *re-scanning* is insufficient averaging due to synchronization effects between beam delivery and respiratory breathing cycle. This problem can be overcome by distributing the re-scans over the respiratory cycle. Thus, unwanted synchronized starts of the re-scans in respect to the respiratory motion can be avoided.

Zenklusen et al. proposed a more sophisticated method of distributing the total particle number of each beam position over the different re-scans (Zenklusen et al., 2010). Instead of equally distributing the particles over all re-scans a fixed amount of particles is delivered to each beam position per re-scan. If its nominal particle number is reached the beam position is omitted in further re-scans. This method not only reduces the impact of synchronization by effectively changing the scan path between re-scans, but also can lower the technical demands regarding the irradiation time of a beam position. This is because in their approach the particle number

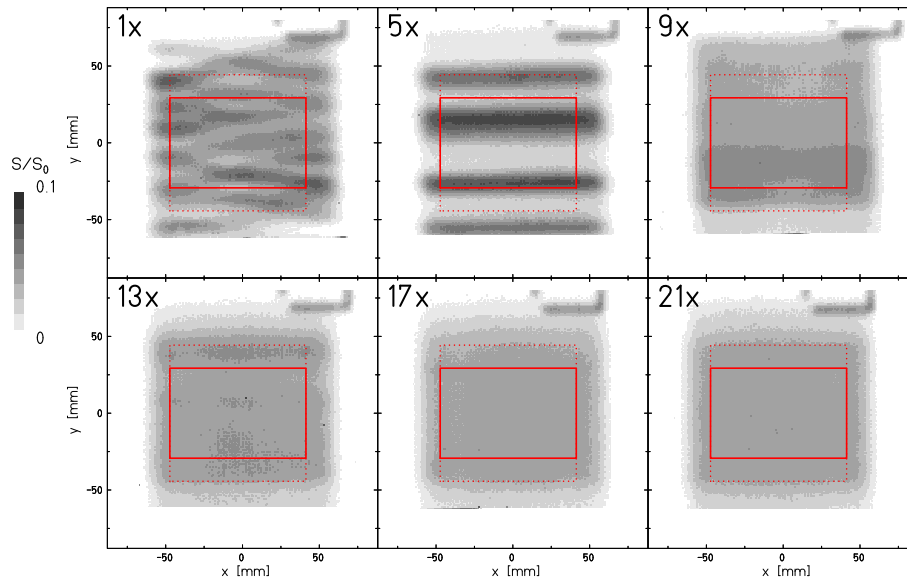


Figure 1.22.: Normalized film response for *re-scanning* irradiations. Target area is drawn with red solid lines. The IMs are indicated by dotted lines. Figure from (Bert et al., 2009a).

per beam position and re-scan is fixed while it scales with the beam positions overall particle number in case of equally distributing particle numbers over all re-scans.

Gating reduces the motion influence by delivering the treatment plan only in a subsample of the complete motion trajectory the so called gating window. Typically, a motion window around end-exhale is chosen as it is the most reproducible motion state showing a comparably small motion (Balter et al., 1998; Ritchie et al., 1994). *Gating* is applicable to both, scanned and passive beam delivery. The motion influence is reduced to the residual motion within the gating window. Thus, for scanned beams the dose distortions due to the interplay effect can be expected to be less severe, while passive beam delivery profits from reduced margins that only need to encompass the tumor under consideration of its residual motion within the gating window. For scanning techniques, several methods have been proposed to reduce the interplay effects due to residual tumor motion. While Furukawa et al. for National Institute of Radiological Sciences (NIRS) as well as Zenklusen et al. for Paul Scherer Institut (PSI) proposed a combination of *gating* and *re-scanning* (Furukawa et al., 2007; Zenklusen et al., 2010), Bert et al. proposed an increased overlap of adjacent pencil beams in lateral as well as longitudinal direction to mitigate the influence of the residual motion (Bert et al., 2009b). *Gating* requires motion monitoring as the beam has to be turned on and off depending on the current tumor position.

At NIRS *gating* functionality has been implemented and has been used with passive carbon beams for therapy of mobile tumors (Minohara et al., 2000). A sketch of a typical *gating* time sequence is shown in Figure 1.23 on the following page.

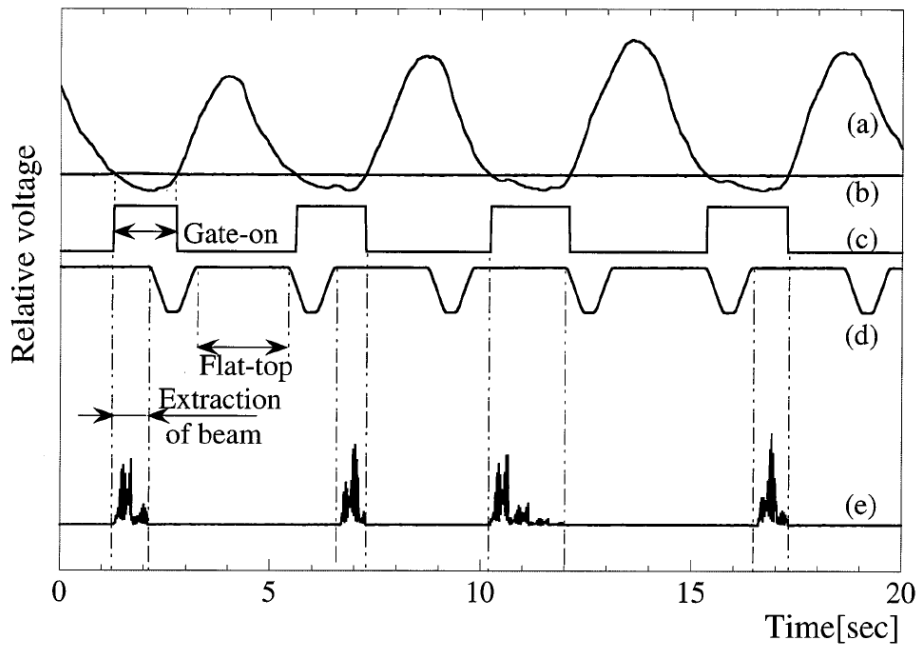


Figure 1.23.: Time sequence of *gating*. In (a) the breathing motion of a patient is shown. The gating window is marked by a solid line (b). Whenever the motion is within the gating window a "Gate-on" signal is triggered (c). Whenever a "Gate-on" coincides with a beam extraction window of the synchrotron accelerator (flat top (d)), beam is extracted (e). Figure from (Minohara et al., 2000).

The idea of BT is to adapt the position of the delivered beams to the actual tumor position in real-time. BT intrinsically does not require an increase of treatment margins. Precise motion monitoring and image registration maps are needed for BT.

BT has been proposed by Keall et al. for IMRT (Keall et al., 2001). In photon therapy, longitudinal tumor position changes can typically be ignored as the photon depth dose profile changes only gradually. Clinically, BT is used in the Cyberknife Synchrony system (see Section 1.3). BT is also applicable for particle beams. The Bragg peak structure of particles poses an additional challenge because dose distributions are also very sensitive against longitudinal changes.

A BT system has been implemented at GSI (Grözinger et al., 2004; Bert et al., 2007). Lateral compensation is performed by employing the scanner magnets. Energy with the required speed changes can not be achieved by the current synchrotron system but are obtained by a polymethyl methacrylate (PMMA) double wedge absorber system that is mounted on fast linear motors proximal to the target (Saito et al., 2009). In their implementation, compensation parameters for the lateral plane as well as the longitudinal direction are pre-calculated for each beam position in each motion state (Bert and Rietzel, 2007). A sketch of the GSI implementation of BT is shown in Figure 1.24 on the next page.

The impact of intrafractional motion on treatment outcome can not only be reduced by dedicated beam application methods as introduced above. By changing the motion itself its influence can become smaller or more predictable.

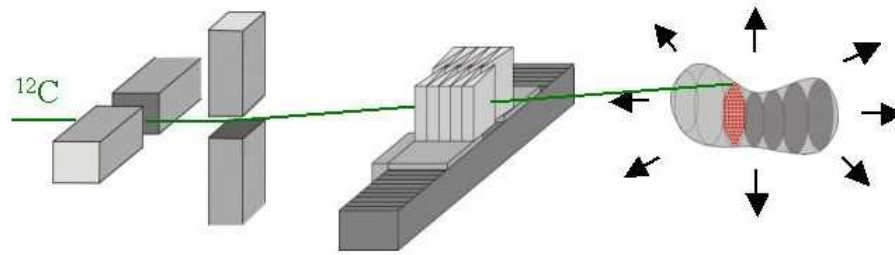


Figure 1.24.: BT system implemented at GSI. Scanner magnets are used for lateral adaptation of pencil beam positions. A dedicated double wedge system is used for fast energy adaptation (Saito et al., 2009). Figure from (Grözinger, 2004).

Breathing is the main cause of motion for many tumor sites subject to intrafractional motion. Different methods have been developed to mitigate the influence of breathing. To reduce the motion amplitude and consequently the required treatment margins abdominal press can be used. The use of abdominal press in photon lung cancer therapy is reported by, e.g., Negoro et al. (Negoro et al., 2001) and Hof et al. (Hof et al., 2003). Breath-hold techniques are reported by (Hanley et al., 1999; Wong et al., 1999). This technique is used to immobilize the tumor. Breath-holds can be induced either automatically by a dedicated device with valves or voluntarily by the patient. Reproducibility and stability of the tumor position are main concerns using this technique (Kimura et al., 2004; Yoshitake et al., 2009).

Expected uncertainties during treatment delivery, e.g., patient motion, can enter the treatment planning process. The aim is to optimize a treatment plan that is robust against these expected uncertainties. Plan robustness can be increased, e.g., by the choice of the treatment field entrance angles. If an OAR is close to the tumor the treatment port in particle therapy is typically chosen such that the OAR is at the lateral rather than the distal edge of the tumor. Thus, uncertainties in particle range do not result in a shift of the treatment field into the OAR. The rationale is that typically the longitudinal Bragg-Peak position is more prone to uncertainties than the lateral Bragg-Peak position is.

Also during optimization of the treatment plan robustness can be an objective. Inaniwa et al. have implemented a robust algorithm into their scanned carbon treatment planning code (Inaniwa et al., 2011). The algorithm explicitly takes range and setup uncertainties into account.

These methods for intrafractional motion mitigation can be combined. Combination of *gating* and *re-scanning* has been proposed by Furukawa et al. (Furukawa et al., 2007, 2010a). Van de Water and colleagues investigated BT for scanned proton beams. They concluded that this method is very susceptible for positioning uncertainties and recommended to combine *re-scanning* and BT to gain robustness (van de Water et al., 2009).

1.6 Aim of this work

This work focuses on the motion mitigation technique BT. BT is a technique that can use the whole accelerator duty cycle (in contrast to *gating*) and at the same time does not require intrinsic motion mitigation technique specific margins (like *re-scanning* and *gating*). BT thus has the potential to combine excellent tumor conformity and short irradiation times for moving tumors. On the other hand it is technically challenging. Especially important are precise motion detection and reliability of patient data, e.g., 4DCT and image registration.

But even if precise and reliable motion information can be provided, BT only works perfectly for translational motion. If other motion components like rotational or deformational components are present, even though the Bragg peak position is adapted the tissue beam path might change. These path changes alter the overall dose distribution. An example for rotational motion is shown in Figure 1.25.

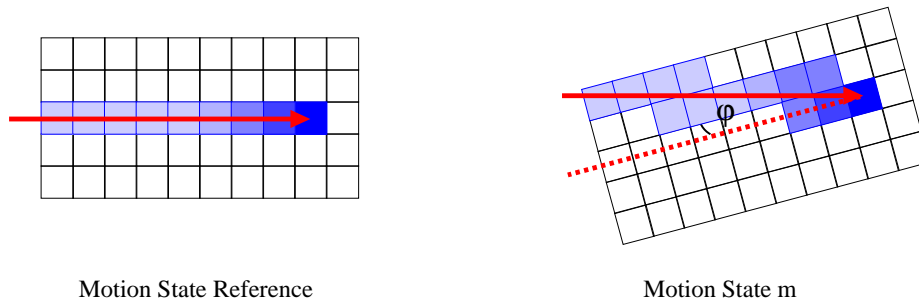


Figure 1.25.: Target volume in two different motion states in case of rotational motion. The shade of color represents the deposited dose. Although BT ensures delivery of Bragg peak dose to the correct position, the overall dose deposition is changed due to the changed tissue beam path. The arrows represents the beam direction while the dashed arrow shows the nominal beam direction for the reference state. Figure adapted from (Bert and Rietzel, 2007).

The exact transition of the patient through the 4DCT phases, i.e., the period and phase of the breathing motion at any time of a whole treatment fraction, is unknown a priori. Dose changes thus can not be considered beforehand, i.e., in treatment planning. Bert and Rietzel (Bert and Rietzel, 2007) proposed a method to compensate these dose changes during beam application. Such a method has to evaluate dose changes at individual beam positions, accumulate these dose changes and eventually compensate them by adapting the nominal particle numbers. All these steps have to be performed in real-time during beam delivery.

In this work such a method, called *real-time dose compensation combined with beam tracking* (RDBT), has been implemented into the therapy control system (TCS) at GSI. The implementation of that method and its experimental verification are described in Chapter 2.

For an assessment of the clinical efficacy of RDBT treatment planning studies have been conducted. They have been based on 4DCT data of lung cancer patients. The study compares the

motion mitigation techniques lateral *beam tracking* (LBT), BT, and RDBT and is presented in Chapter 3.

Finally, a new method based on RDBT is proposed that has the potential to supersede the technically complex fast energy adaptation system needed for BT and RDBT. This method along with initial measurements and simulations are presented in Chapter 4.



2 Implementation and experimental verification

The content of this chapter has in similar form been published (Lüchtenborg et al., 2011).

Contents

2.1. Introduction	51
2.2. Material & methods	52
2.2.1. Dose compensation - theoretical basis	52
2.2.2. Dose compensation - Implementation into therapy control system	57
2.2.3. Dose compensation - dosimetric assessment	57
2.3. Results	62
2.3.1. Measurements	62
2.3.2. Starting phase dependence	63
2.4. Discussion	66
2.5. Conclusions	68

2.1 Introduction

In this chapter the implementation of a real-time dose compensation extension for *beam tracking* (BT) into the therapy control system (TCS) at GSI Helmholtzzentrum für Schwerionenforschung GmbH (GSI) is described. Several experiments employing moving detectors have been performed to verify the implementation with the goal to show the benefit gained from the implemented dose compensation method. This has been done by comparing dose delivery on a static target and a moving target for BT as well as for *real-time dose compensation combined with beam tracking* (RDBT). Target volumes with simple geometric shapes, like box and sphere, were used in combination with a large (24°) purely rotational target motion. The scope of this work was verification of the implemented dose compensation technique rather than application to a scenario that resembles typical tumor motion. By choosing large rotational motion the effect of dose changes is expected to be also large. The chosen rotation angles rather represent a worst-case scenario than a typical tumor motion but are expected to facilitate the experimental comparison of RDBT and BT. The possible clinical benefit of RDBT for a more typical tumor motion range is assessed by means of treatment planning studies in Chapter 3.

2.2 Material & methods

The theoretical basis for dose compensation is described in Section 2.2.1, its implementation is described in Section 2.2.1. In Section 2.2.3 the measurements for dosimetric assessment of the implemented method are described.

2.2.1 Dose compensation - theoretical basis

BT treatment plans are typically optimized for one reference motion state from tumor imaging (e.g., one time resolved computed tomography (4DCT) state). Due to the tumor motion the anatomical structure underlying a beam position is in general not any longer at the position assumed in treatment planning, i.e., the position in the reference motion state. BT aims at changing beam parameters such that the Bragg Peak dose is again delivered to the same anatomical structure. Therefore, the beam parameters (i.e., beam position in perpendicular plane and beam energy determining beam range) are adapted according to the current motion. The required adaptation vectors can be obtained from image registration (Brock et al., 2006; Rietzel and Chen, 2006). The components of the BT system implemented at GSI are shown in Figure 2.1 on the next page.

However, BT can preserve the overall dose only for the special case of pure translational motion. In the presence of other motion components like rotations and deformations, parts of the tissue will receive more or less dose than in treatment planning because its position relative to the beam axis is changed despite BT (see Figure 1.25 on page 48). RDBT considers these dose changes by accumulating the dose changes for all beam positions during treatment delivery. Once a beam position is irradiated, its cumulative dose change is compensated by adapting the nominal particle number applied to that beam position. Overdose compensation is carried out by reducing the number of particles delivered to a beam position. Thus, the overdose compensation of a beam position is limited by its nominal particle number and can in some cases only be reduced but not completely avoided. In contrast, the clinically more crucial underdoses can always be compensated by increasing the number of particles delivered to a beam position.

The general workflow of the RDBT method is shown in Figure 2.2 on page 54. In addition to choosing the position adaptation values $\Delta(x, y, z)_i^m$ matching the actual beam position i and motion state m , dose changes to all following beam positions caused by the irradiation of the current beam position are calculated. As the applied particle number itself is fed back to the dose compensation calculation procedure, RDBT is considered a closed-loop approach. The term dose change here always means the difference between the (motion state m dependent) actual deposited dose to a beam position i and the dose that would have been deposited according to 3D reference treatment planning. Like mentioned earlier, even if the treatment planning 4DCT data is still valid at time of dose delivery, dose changes will occur simply due to the

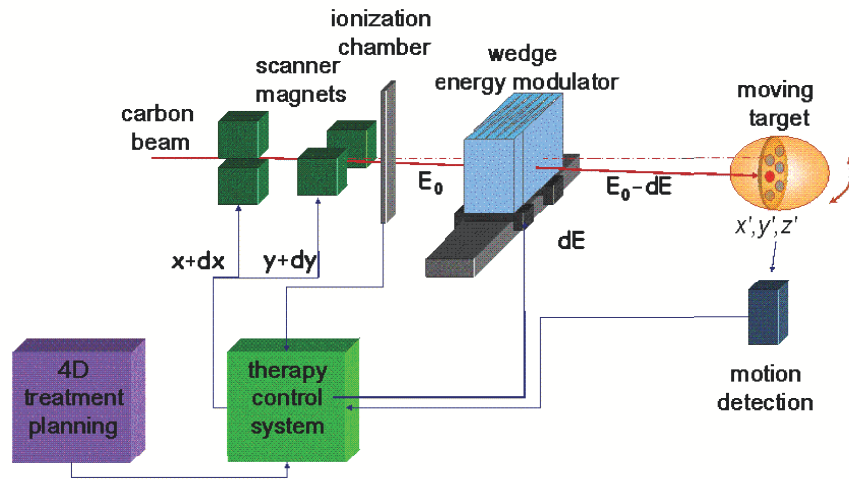


Figure 2.1.: Setup of the GSI BT system. Target motion is measured by laser triangulation and used to determine, based on 4D treatment planning, position adaptation parameters. For compensation of lateral shifts the scanner magnets are used while a double wedge is used to compensate depth changes. Figure adapted from (Saito et al., 2009).

a priori unknown motion state a beam position is actually irradiated in. Furthermore, while in this experimental setup the intrinsic assumption that the 4DCT is still valid at application time is obviously true, this assumption might not be valid in patient cases. The influence of anatomy changes between imaging and therapy on different motion mitigation techniques has to be investigated in dedicated treatment planning studies (see Chapter 3).

Implementation of the dose compensation functionality into GSI's treatment planning system TRreatment planning for Particles (TRiP) (Krämer et al., 2000) has been based on the method proposed by Bert and Rietzel (Bert and Rietzel, 2007) which is summarized in the following. The method can be subdivided into two parts. The first part is calculation of dose compensation parameters D_m^{ik} and can be done off-line during treatment planning and is therefore not time-critical. The second part, in contrast, is highly time-critical. During irradiation of one raster position (few ms) the resulting dose changes to all following beam positions have to be calculated from precalculated dose compensation parameters and measured motion state.

Dose compensation parameter optimization

The basic idea of dose compensation is to adapt the particle number applied to a beam position considering motion induced dose changes caused by earlier irradiated beam positions. At irradiation time of a beam position only the particle number of so far not irradiated beam positions can still be changed. Thus, it is sufficient to precalculate only dose compensation parameters concerning later irradiated beam positions.

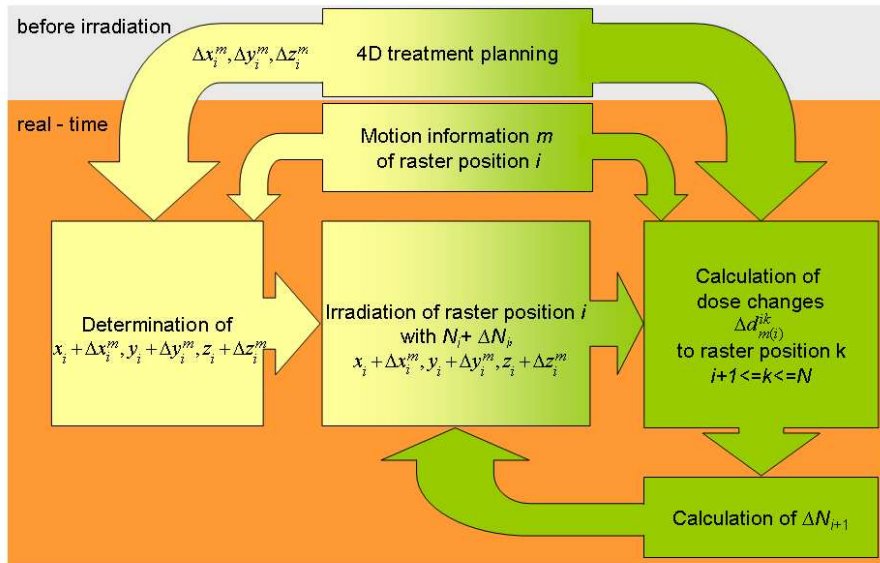


Figure 2.2.: This figure illustrates the basic workflow of RDBT. RDBT is an extension of BT. For a currently irradiated beam position i parameters $\Delta x_i^m, \Delta y_i^m, \Delta z_i^m$ are read from 4D treatment planning considering the motion information and the nominal Bragg peak position x_i, y_i, z_i are adapted accordingly. The dose changes at beam positions k , where $i + 1 \leq k \leq N$ are calculated. Necessary adaptation of particle number for beam position $i + 1$ is communicated to the therapy control system controlling the irradiation. While the BT part (left branch, bright yellow) can be considered as an open-loop approach, the dose compensation extension (right branch, dark green) is a closed-loop system as the result of the irradiation is fed back to the ΔN calculation to adapt future dose application.

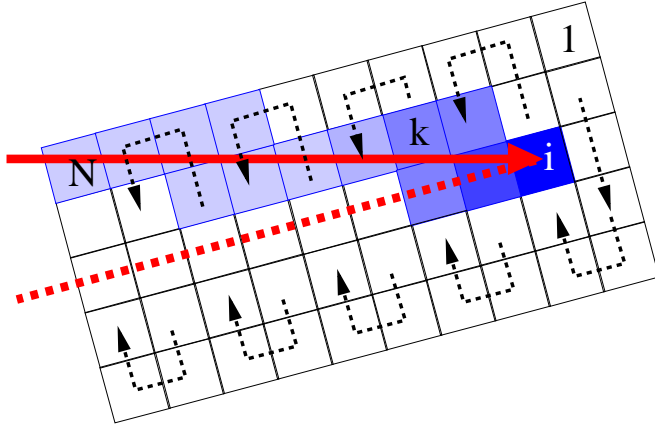


Figure 2.3: Treatment plan in motion state m . Scanning starts in the most distal slice at beam position 1 and passes beam positions i and k . The last beam position is N . Scan path is represented by the dashed arrows. Consider that this is a 2D representation of the treatment plan. Therefore, each vertical row represents one IES.

Motion State m

Assuming a target volume consisting of beam positions $1 \leq i, k \leq N$ and a motion described by 4DCT states $1 \leq m \leq M$ (see Figure 2.3), the motion state dependent dose delivered to beam position k while irradiating beam position i can be defined as D_m^{ik} . This quantity assumes deposition of the nominal particle number to beam position i . For each beam position i the D_m^{ik} for $i \leq k \leq N$ are calculated with TRiP and stored for each motion state m in a look-up table. Hence, the look-up table is dependent on the scan path, i.e., the sequence of the beam positions. As dose deviations are mainly caused by the beam plateau proximal to the Bragg peak, the plan is preferably executed starting at the most distal energy slice. Because the motion state a beam position is irradiated in is not known a priori, dose compensation parameters for all motion states need to be provided in real-time. In the current implementation of RDBT the number of beam positions in a treatment plan is limited by the memory size of the look-up table.

Real-time dose compensation

It is assumed that beam position i is currently irradiated. All calculations described in this section are performed by the TCS for all beam positions $1 \leq i \leq N$. At irradiation time of a beam position i the motion state m is known from motion monitoring. Thus, the actual dose difference for every beam position $k > i$ can be calculated. Hereby, one needs to take into account that the particle number delivered to beam position i is already adapted. Thus, the dose change to beam position k can be calculated as follows:

$$\Delta d_{m(i)}^{ik} = \left(\tilde{D}_{m(i)}^{ik} - D_{\text{ref}}^{ik} \right), \quad (2.1)$$

with ref denoting the reference motion state of the 4DCT and $\tilde{D}_{m(i)}^{ik}$ representing the dose actually deposited at beam position k during irradiation of raster position i . The dose deposited at position i itself typically is also modified by the dose compensation. As the look-up table entries

D_m^{ik} were determined assuming deposition of nominal particle number to beam position i , the actual dose can be calculated by multiplying D_m^{ik} by the fraction of the planned dose actually deposited at beam position i . ΔD^i denotes the cumulative dose change of beam position i from irradiation of beam positions $1 \leq p < i$:

$$\Delta D^i = \sum_{p=1}^{i-1} \Delta d_{m(p)}^{pi}. \quad (2.2)$$

$\tilde{D}_{m(i)}^{ik}$ can now be written as

$$\tilde{D}_{m(i)}^{ik} = D_{m(i)}^{ik} \left(1 - \frac{\Delta D^i}{D_{\text{ref}}^{ii}} \right). \quad (2.3)$$

It should be stated here that in case $\Delta D^i \geq D_{\text{ref}}^{ii}$ the dose received by beam position i already exceeds the planned dose delivery. As a reduction of the already delivered dose is not possible even applying no particles to that beam position will result in a local over- dose.

As the current GSI scanning system does not allow to skip single beam positions, currently instead of no particles a predefined minimal fraction of the nominal number of particles is delivered in case of an accumulated overdose that can not be completely compensated.

Combining Equation 2.1 on the previous page and Equation 2.3 yields

$$\Delta d_{m(i)}^{ik} = \left(D_{m(i)}^{ik} \left(1 - \frac{\Delta D^i}{D_{\text{ref}}^{ii}} \right) - D_{\text{ref}}^{ik} \right), \quad (2.4)$$

for the dose change deposited at beam position k during irradiation of beam position i . To correctly represent the real situation the term $1 - \Delta D^i / D_{\text{ref}}^{ii}$ is checked and if necessary set to the predefined minimal fraction of the nominal particle number. The individual dose change counters ΔD^k existing for each beam position are incremented by $\Delta d_{m(i)}^{ik}$ for all $k > i$. The dose change ΔD^{i+1} for beam position $i + 1$ is needed by the TCS for adapting the nominal particle number. In order to avoid conversions including daily changing ionization chamber calibration factors it is advantageous to pass a unit-independent quantity. Therefore, not ΔD^{i+1} but the relative quantity $\Delta D^{i+1} / D_{\text{ref}}^{(i+1)(i+1)}$ is passed to the TCS. The TCS finally changes the nominal particle number N_{nom}^{i+1} to

$$N_{\text{adapt}}^{i+1} = N_{\text{nom}}^{i+1} \left(1 - \frac{\Delta D^{i+1}}{D_{\text{ref}}^{(i+1)(i+1)}} \right). \quad (2.5)$$

2.2.2 Dose compensation - Implementation into therapy control system

The existing BT software of the TCS has been extended by a dose compensation functionality. Thus, RDBT is now experimentally available.

The TCS software is organized in a loop structure. It is essential that the loop time of the software is considerably shorter than the irradiation time of a beam position which is in the order of some milliseconds. This is crucial if the particle number of a beam position and thereby its irradiation time is lowered by the dose compensation itself. In the current setup the dose compensation software is running on a RIO4 VME processor board (CES, Switzerland) providing a 1 GHz GHz processor and 512 MB on-board memory. 448 MB are usable for dose compensation. In combination with 25 motion states this allows for a maximal treatment plan size of 3064 beam positions. With this implementation, loop times in the order of 30 μ s have been measured. In the following way the software workflow has been structured to minimize computational load during time-critical phases and to pass computed compensation values as fast as possible to the TCS:

During irradiation of beam position i the most time-critical task is to pass the cumulative dose change of beam position $i + 1$ to the TCS before irradiation of raster position $i + 1$ starts. Therefore in the current implementation first of all ΔD^{i+1} is calculated and the respective relative dose change is passed as described above. Then, the dose changes for the beam positions of the current IES are calculated and the respective counters are updated. To reduce the workload during the time-critical raster position irradiation, all calculations concerning beam positions in the remaining IESs of the treatment plan are shifted to the accelerator extraction pause prior to the next IES. These pauses before each IES are obligatory as the beam energy changes are actively requested from the synchrotron accelerator. Typically, they last for a few seconds (≈ 2.2 s at GSI), providing more than enough time to make up for the calculations shifted during irradiation of the IES. In Figure 2.4 on the next page the software workflow comprising the most important software tasks is summarized.

Log file analyses showed that these loop times are short enough to guarantee a proper execution of all necessary steps even for beam positions where the nominal particle number and consequently the irradiation time was decreased.

2.2.3 Dose compensation - dosimetric assessment

Measurements

Experiments to assess the technical performance of the implemented dose compensation functionality have been performed. As mentioned above, dose changes only occur for nontranslational motion components, so a rotational motion realized by a dedicated rotational table has

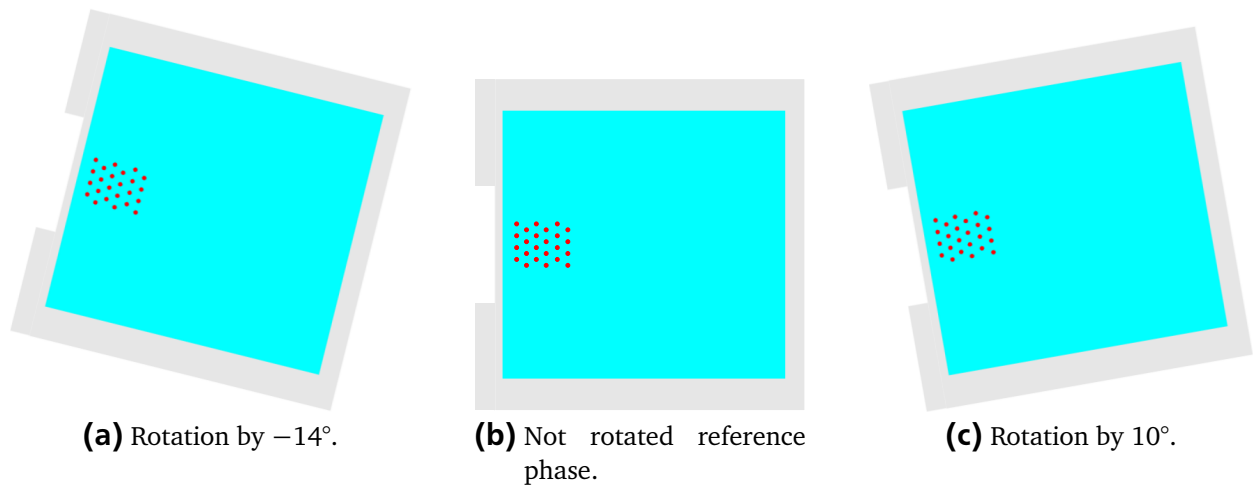


Figure 2.5.: Figure 2.5b shows the water phantom in its reference state while Figure 2.5a (-14° rotation) and 2.5c (10° rotation) show the extreme motion states. Filled red circles represent the position of the ionization chambers. The center of rotation is 45 mm downstream the entrance window.

been used in the experiments. The table was rotating between -14° and 10° (see Figure 2.5). A laser triangulation system (Sick Vertriebs GmbH, Düsseldorf, Germany, Model OD100-35P840) was used for motion feedback. To induce additional need for energy changes a ramp-shaped absorber made from polymethyl methacrylate (PMMA) was positioned proximal to the motion table. The absorber did not move during beam delivery thus introducing a position-dependent bolus thickness since BT was used. A sketch of the setup can be seen in Figure 2.6 on the next page. The large rotation as well as the additional ramp-absorber have been introduced to clearly demonstrate the dose change effect rather than to resemble the clinical situation where the tumor motion possibly comprises a mixture of translational, rotational, and deformable components.

A computed tomography (CT) reflecting the not rotated setup including the ramp-absorber was constructed and considered as reference state. The amplitude of the laser sensor signal representing the complete rotation (between -14° and 10°) was equidistantly divided into 25 motion states. For each motion state the rotational angle representing the motion state's center was determined and corresponding transformations for the reference CT state were analytically calculated. 4DCT phases were obtained by applying the transformation to the reference CT state.

An array of ionization chambers in a water tank that was used in clinical routine for patient treatment plan verifications at GSI (Karger et al., 1999) was employed as detector system. The setup was aligned using the in-room laser system that in the past was also used for patient alignment. Treatment planning was performed according to Bert and Rietzel (Bert and Rietzel, 2007) and is shortly summarized here. After delineation of the target contours, TRiP was used to optimize the number of carbon ions deposited at each beam position. The overall target dose

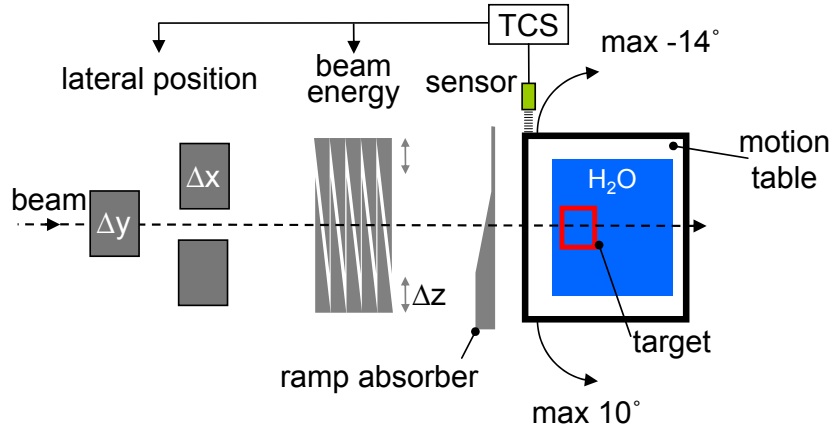


Figure 2.6.: Setup for experimental verification. The BT system (see Figure 2.1 on page 53) was employed to adapt beam positions to the changing target position. The motion table introduced rotational motion. Additional necessity for energy changes was caused by the ramp absorber.

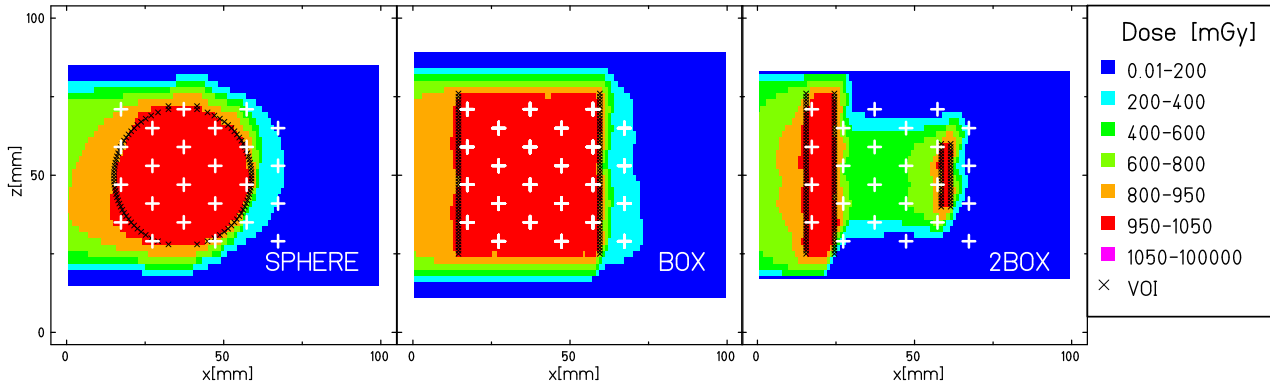


Figure 2.7.: Nominal dose distributions for all target geometries. Prescribed dose has been 1000 mGy.

was set to 1 Gy. IES spacing was set to 3 mm water-equivalent ($3 \text{ mm}|_{\text{H}_2\text{O}}$) and a 3 mm ripple filter was used (Weber and Kraft, 1999). For all plans irradiation sequence starts at the most distal IES. Within one slice the beam position spacing was set to 3 mm in horizontal as well as vertical direction. The spot size was from 7.3 mm to 7.6 mm (depending on IES) full width at half maximum (FWHM). Three different volumes of interest (VOIs) were used:

- **SPHERE:** A sphere with 22 mm radius,
- **BOX:** A box of $50 \times 15 \times 45 \text{ mm}^3$ (in beam's eye view horizontal 50 mm, vertical 15 mm, longitudinal 45 mm),
- **2BOX:** A plan consisting of two boxes (proximal box $50 \times 15 \times 10 \text{ mm}^3$, distal box $20 \times 15 \times 5 \text{ mm}^3$).

Nominal dose distributions for all geometries can be seen in Figure 2.7. In addition, dose

compensation parameters D_m^{ik} were calculated for $1 \leq i \leq N$, $i \leq k \leq N$, $1 \leq m \leq 25$. RDBT was compared to BT by experiments each consisting of three measurements:

- REF: Irradiation scheme where the nominal treatment plan was applied. target was in reference phase (i.e., 0°) and not moving. Neither BT nor RDBT were used,
- POS: Irradiation scheme using BT. The target was rotating between -14° and 10° ,
- FULL: Irradiation scheme using RDBT. The target was rotating between -14° and 10° .

All relevant delivery data, e.g., particle number for every beam position, beam position, and target motion state, were logged during treatment. Thus, it was possible to reconstruct dose distributions for each individual measurement by using TRiP4D (Bert and Rietzel, 2007; Richter et al., 2011). The treatment planning code TRiP4D is an extension of the TRiP98 code developed by Krämer et al. (Krämer et al., 2000; Krämer and Scholz, 2000). The 4D version is in more detail described in Section 3.2.1.

Data analysis

To focus on the motion and motion mitigation dependent differences between POS and FULL dose deviations in comparison to POS are reported. Direct access to these dose differences is provided by the ionization chamber measurements that have been analyzed separately for over- and underdose by determining the mean and standard deviations, respectively. Analysis has been restricted to ionization chambers that are positioned inside the respective VOIs. As the mean dose differences for FULL as well as POS is expected to be close to zero the distributions have been analyzed not for different mean values but for significant variance changes using the Bartlett test (Bartlett, 1937).

Data from dose reconstructions are complementing the direct dose measurements as they provide the dose deposition at any location inside the target volume. To compare measurements and dose reconstructions, reconstructed dose values were extracted at the nominal ionization chamber positions inside the target volumes. Measured as well as reconstructed dose values have been grouped into three subsamples (REF, POS, and FULL). Correlation analysis has been performed to assess the validity of dose reconstruction.

The reconstructed dose difference distributions were compared by means of histograms. χ^2 -analysis has been applied to test if the differences between the POS and the FULL histogram distributions are significant.

Robustness of dose compensation

It is well known that interplay patterns are very sensitive to the motion state at irradiation start (Bert et al., 2008). In the context of robust planning a motion mitigation technique is

favorable when the dependence of the resulting dose distributions on the motion starting phase is small. Simulations covering a larger parameter space and thus complementing the performed measurements were performed with TRiP4D. The goal of these simulations was to investigate the influence of the motion starting phase on BT and RDBT, respectively. Dose calculation is performed in a similar way like in the dose reconstructions described above but using simulated rather than measured input data.

The BOX and SPHERE treatment plans used for the experiments were used for this simulation. For better comparability one measured motion trajectory was used for all simulations. Ten different starting phases, evenly distributed over the whole motion cycle (≈ 3.8 s) were defined by introducing a time offset on the motion trajectory. Dose delivery was simulated using the same 4DCTs the experiments were based on. Dose-volume-histograms (DVH) were calculated from the resulting dose distributions.

2.3 Results

2.3.1 Measurements

Dosimetric results are assessed by calculating the dose differences obtained in the motion affected setups (POS and FULL) and the static setup (REF). To assess the benefit of RDBT the variances of the distributions have been compared. The Bartlett test (Bartlett, 1937) indicates significant variance changes for the BOX (20 measurement positions) as well as SPHERE plan (12 measurement positions) for the measured as well as the reconstructed distributions. The 2BOX plan did not show significant variance changes but at the same time only provides four measurement positions. For further analysis under- and overdoses are considered separately.

The average under- and overdoses measured by the ionization chambers positioned inside the VOI and their standard deviations are reported in Table 2.1. RDBT could in all cases re-

Table 2.1.: Average (± 1 standard deviation) measured under- as well as overdoses in POS and FULL compared to REF with dose values in mGy. Nominal dose was 1000 mGy. Only ionization chambers (ICs) inside the VOI are considered. The number of ICs for each geometry is listed.

geometry	# ICs	underdose		overdose	
		BT	RDBT	BT	RDBT
BOX	20	52(± 36)	12(± 14)	53(± 30)	37(± 32)
SPHERE	12	30(± 30)	24(± 13)	27(± 33)	13(± 26)
2BOX	4	68(± 91)	25(± 13)	45(± 35)	25(± 16)

duce the average under- as well as overdoses. In most of the measurements, especially for the underdoses, also the standard deviations could be considerably reduced.

Dose values from measurement as well as reconstruction were grouped in REF, POS, and FULL. Correlation has been investigated for all groups separately. The squared correlation coefficient r^2 was 0.98 for all groups. The respective slope was between 0.95 and 0.98. These results show that measurements and reconstructions are well correlated and the correlation is virtually independent on the motion mitigation technique applied. It could thus be concluded that the reconstructed dose difference distributions can also be used to compare BT and RDBT.

Histograms of the reconstructed dose difference distributions inside the VOIs for Pos as well as FULL are shown in Figure 2.8 on the following page for all geometries. χ^2 -analysis at 5% significance level showed that the dose difference distributions obtained in FULL are significantly different compared to the distributions obtained in Pos. These reconstructed distributions offer better statistics as every CT voxel inside the VOI could be evaluated compared to the above analyzed distributions that consider measurement positions only. Tests on the reconstructed dose difference distributions show a significant distribution difference also for the 2BOX geometry.

Cuts through the central plane of the reconstructed dose difference distributions are shown in Figure 2.8 on the next page for all geometries. While the dose differences outside the VOIs are comparable in BT and RDBT, inside the VOIs the dose differences are clearly reduced in case of RDBT. It is striking that the global dose change pattern for BT expands also into the VOI but for RDBT at the VOI border there is a sudden drop in the amount of dose change. For BT areas of under- as well as overdose exceeding 100 mGy are visible (brown and pink areas) representing cold and hot spots in the dose distribution. RDBT shows virtually no misdoses of that extent. Even under- and overdoses in the range between 50 mGy and 100 mGy (blue and red voxels) only appear rarely.

2.3.2 Starting phase dependence

The DVHs from simulations for BT as well as RDBT can be seen in Figure 2.9 on page 65 for the Box geometry as well as the SPHERE geometry, respectively. Each DVH is representing a different starting phase of the motion. In each figure the 10 DVHs for BT are drawn in red while the 10 DVHs representing RDBT are presented in blue. In both figures the RDBT DVHs are superior to the BT DVHs. Under- and overdoses are clearly reduced. Moreover, the spread of the RDBT DVHs is smaller than the spread of the BT DVHs meaning that the dose distributions are more robust against varying motion starting phases when RDBT is used. Comparing both geometries, it is interesting to see that although the spread in the BT DVHs is reduced for the SPHERE plan compared to the Box plan the average maximum over- and underdose is virtually unchanged.

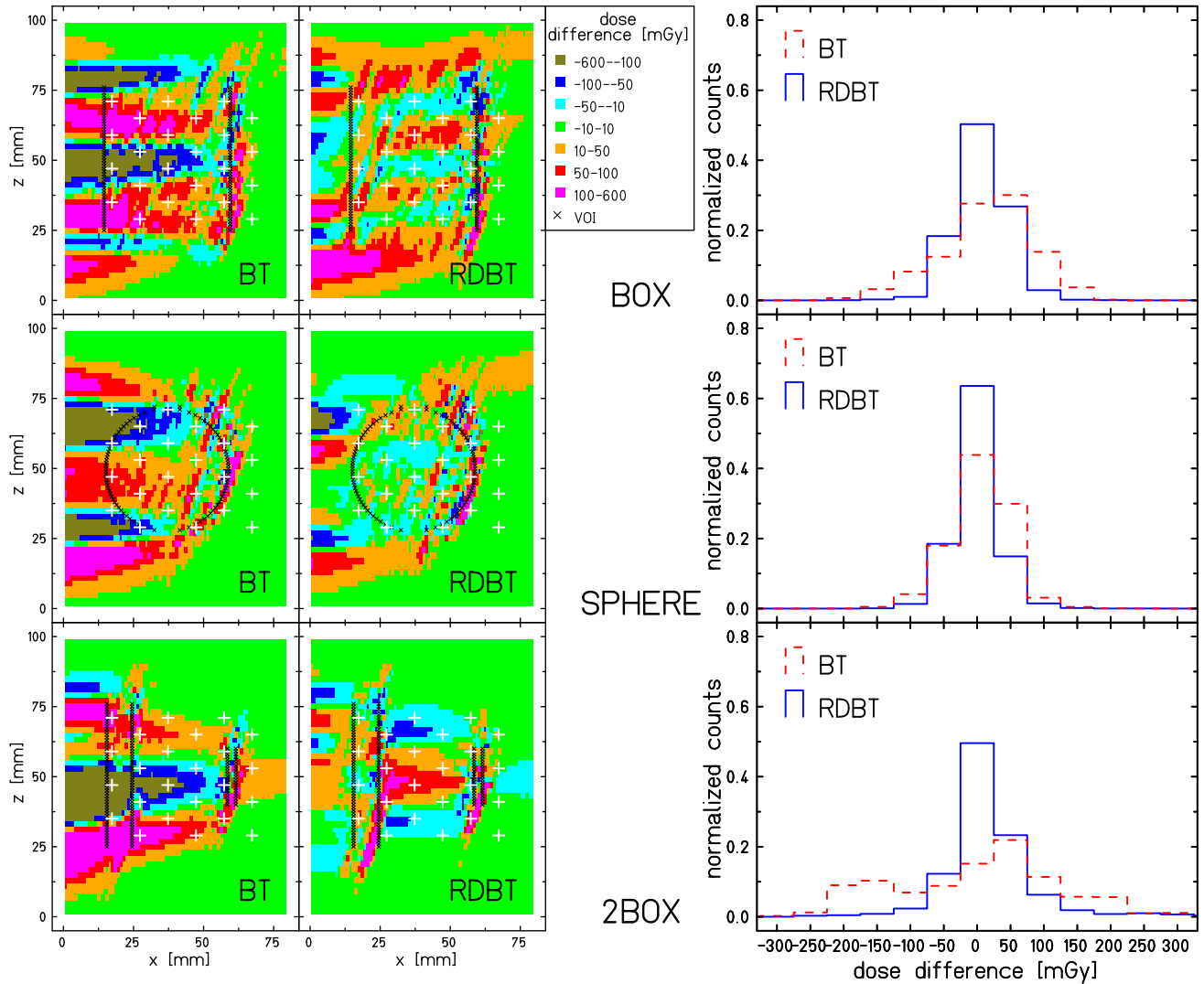


Figure 2.8.: Differences between the dose reconstructions for BOX (top row), SPHERE (middle row), and 2Box (bottom row). Shown is a cut in the x-z plane through the iso-centre. Dose reconstructions have been based on logged beam delivery data from experiments. Ionization chamber positions are marked by white crosses. x is beam direction, z is the lateral plane (left right in beam's eye view). To assess the dose differences not only in the iso-centre plane but in the complete VOI, additionally histograms of the dose difference distribution within the VOIs are shown (blue solid lines for RDBT, red dashed lines for BT). The under- as well as the overdose inside the VOI (marked in black) could substantially be reduced in RDBT compared to BT.

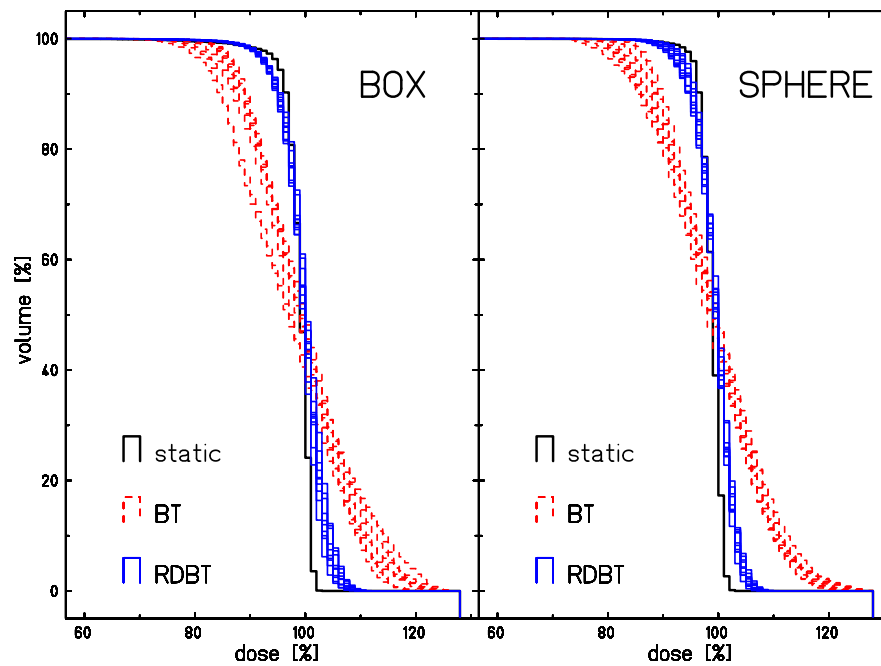


Figure 2.9.: DVHs for BT (red dashed lines) and RDBT (blue solid lines). The stationary DVH is drawn in black as reference. Simulations have been performed for the Box as well as the SPHERE treatment plan. For both moving cases ten different starting phases, evenly distributed over the motion cycle, have been analyzed. The RDBT cases are much closer to the reference showing much smaller under- as well as overdoses compared to BT. In addition, RDBT seems to be more robust against varying starting phases as the spread of the DVHs is much smaller.

2.4 Discussion

The general task of treatment planning is to determine delivery parameters that ensure delivery of a predefined dose to a patient represented by imaging data, e.g., a CT. By moving to tumor sites showing considerable intrafractional motion, additional knowledge concerning the motion trajectory is essential for treatment planning. Obtaining a motion data set before treatment that is still valid at time of therapy seems challenging, especially if patient motion is irregular. Even if the validity of the 4DCT itself can be assumed, uncertainty about the respiratory trace determining the temporal sequence of the single 4DCT states remains. One approach to overcome this problem is to implement a real-time closed-loop system. Such a system accounts for the dose deviations between planned and deposited dose distribution in real-time and feeds them back to the ongoing dose delivery process. Based on this information, the dose delivery parameters are adapted to minimize the dose deviations.

The proposed RDBT method is such a closed-loop method. Based on measured motion information obtained during beam delivery, the motion impact on dose delivery is calculated and used to change nominal particle numbers of future beam positions (see Figure 2.2 on page 54). In this way, the delivered dose distribution gets closer to the planned dose distribution. While changes in the motion trajectory (e.g. respiratory frequency) can be handled, it is still assumed that the planning 4DCT represents the patient's anatomy at treatment time. For the performed experiments this was obviously the case but for patient data the validity of the 4DCT will among other factors depend on the time between imaging and treatment delivery. Thus, the delay between imaging and treatment should be reduced as far as possible.

The quantitative benefit of RDBT for patient treatments can only be evaluated in dedicated treatment planning studies (see Chapter 3). Some qualitative trends can already be anticipated. All motion mitigation techniques rely on the validity of patient information. While, e.g., *gating* only relies on imaging, image registration and motion data concerning a subset of the whole motion cycle, i.e., the gating window, BT and RDBT require valid information during the whole motion cycle. The quality and reliability of imaging and registration data might thus be more crucial for BT and RDBT than for other motion mitigation techniques. Artifacts impairing the 4DCT quality have been reported among others by Persson et al. (Persson et al., 2010). However, methods to mitigate artifacts are reported (Mori et al., 2006) and further improvements in this field can be anticipated.

Several groups investigated reproducibility of respiratory motion and found that the motion itself is often reproducible (Sonke et al., 2008; Michalski et al., 2008). In a large multi-institutional study Brock et al. report that the accuracy of deformable image registration algorithms is within the CT voxel resolution especially for lung tumors (Brock, 2010).

Thus, sufficient data quality for at least a subgroup of patients seems achievable. Real-time motion monitoring is employed to deduce the 4DCT state representing the current motion state

best. Motion monitoring could be based on the methods used for the Cyberknife Synchrony system (Ozhasoglu et al., 2008; Seppenwoolde et al., 2007).

Taking into account these considerations, the patient predestinated for the application of RDBT would be a patient with good 4DCT and image registration quality, a reproducible motion with a large amplitude containing nontranslational components. The overall benefit of RDBT over BT in such a patient is expected to increase if the number of treatment fields or fractions is reduced, since it is known that a larger number of fields or fractions leads to an averaging of dose deviations and thus improves dose homogeneity (Phillips et al., 1992; Knopf et al., 2010).

As already stated above, the concept of RDBT shows some similarities to real-time motion-adaptive-optimization (MAO) proposed by Lu et al. for TomoTherapy (Lu et al., 2009). Both methods adapt the amount of dose delivered in the next basic dose delivery unit in real-time. While this basic unit for TomoTherapy is a projection and the according leaf-open time is changed, in RDBT the basic unit is a beam position and its nominal particle number is changed. Both methods also accumulate the already delivered dose based on real-time motion measurements and feed that information into the dose adaptation process. That makes both methods closed-loop approaches. While MAO also includes the future dose estimation into the optimization process in RDBT currently only the already deposited dose is considered. RDBT might also profit from future dose estimation, this will be discussed later in this section.

Reconstructed dose distributions show for the large rotational target motion used that the dose patterns deposited using RDBT are significantly closer to the ones deposited in the stationary reference irradiation than the dose distributions deposited using BT are. While for BT global dose change patterns expand into the VOI, RDBT dose distributions show clearly reduced dose deviations inside the VOI. Patterns outside the VOI are comparable. It is important to realize that RDBT can only accumulate and compensate dose changes for beam positions. beam positions are per definition within the VOI and not outside the VOI. Nevertheless, experiments give a hint that also motion and BT induced dose changes outside the VOI might be of importance. Especially if organs at risk (OARs) are concerned, methods to monitor and, if necessary, minimize these dose changes (at least the overdoses) might be needed. An implementation is possible by introducing virtual raster points in OARs which enter the RDBT process with maximal dose levels rather than nominal ones. This question can only be addressed by careful analysis of dedicated treatment planning studies.

Dose measurements and dose reconstructions have been shown to be highly correlated, indicating that analysis based on reconstructed dose distributions are suited as well to assess the performance of RDBT in comparison to BT.

Measured and reconstructed dose differences compared to the stationary reference irradiation could be significantly reduced if RDBT was used instead of BT alone. The occurrence of underdoses per se in RDBT is assigned to the fact that the currently implemented method only takes into account dose changes of already irradiated beam positions. Hence the contribution of

future beam positions, i.e., mainly beam positions in the same IES due to their lateral overlap, is assumed to be the nominal one, i.e., as in treatment planning. Depending on the motion state and the particle number correction applied to future beam positions their contribution to the current position might be different from their nominal contribution. Motion prediction would allow consideration of dose changes caused by the next beam positions. Their contribution to the current beam position is relatively large due to the lateral overlap of pencil beams. It is expected that underdoses can be further reduced if not even eliminated using motion prediction. Such a method presumably also reduces the remaining overdoses. Overdoses might, as discussed earlier, not be avoidable in every case because the minimum particle number applicable to a beam position equals zero. In contrast to photons, the majority of dose deposited by charged particles is delivered at the Bragg-Peak position. Therefore, it is expected that already a short term prediction of dose changes covering the beam positions in the direct surrounding of the actual Bragg peak position might be sufficient for a reasonable improvement. That would of course considerably facilitate the process of motion prediction. Considering irregularities in patient motion, its prediction gets harder the longer the relevant time span is.

Simulations showed that RDBT has the potential to substantially improve the outcome of an irradiation on a moving target. RDBT proved itself to be more robust than BT and to decrease the under- and overdoses introduced by target motion. However, also the simulations are based on the artificial experimental situation and are not easily transferrable to clinical situations. One might speculate that a RDBT irradiation is also for other clinically more typical motion patterns more robust against changing irradiation and motion parameters. The possible quantitative gain and the robustness against other factors have to be assessed in treatment planning studies that are currently ongoing.

It seems plausible that due to the large rotations the effects on dose distributions both inside as well as outside the VOI are larger in these experiments and simulations compared to those one should expect for a typical clinical case. However, the motion type does not influence the technical workflow. Thus, the current implementation is transferable to situations where also translations and deformations are present.

2.5 Conclusions

A method for real-time compensation of dose changes introduced in BT irradiations by non-translational motion components has been implemented in the GSI therapy control system and verified for large rotational motion. A transfer to more complex motions, especially measured patient motion, seems feasible if 4DCT data and registration data are provided. As the method uses already delivered dose as a feedback for adapting future dose deposition it is considered as a closed-loop approach. Experiments and complementary simulations comparing BT and RDBT showed significantly better coverage of the target volume of the latter method.

3 Treatment planning studies

Contents

3.1. Clinical particle therapy for lung cancer	69
3.2. Material & methods	70
3.2.1. 4D treatment planning framework	70
3.2.2. Simulation input data	76
3.2.3. Analysis	81
3.3. Results	83
3.4. Discussion	88

In the previous chapter the implementation of the *real-time dose compensation* functionality extending *beam tracking* (BT) has been verified. However, the experimentally used motion parameters were not meant to resemble typical motion parameters but rather to cover a worst-case scenario. Therefore, this chapter will focus on the assessment of the clinical benefit of *real-time dose compensation combined with beam tracking* (RDBT). Time resolved computed tomography (4DCT) data from lung cancer patients have been used to simulate scanned carbon ion dose delivery. Different techniques have been simulated: Beam application without motion mitigation (i.e., interplay), with lateral *beam tracking* (LBT)¹, with BT, and with RDBT.

The following sections will first shortly review the clinical experience for particle treatments of lung tumors. Subsequently the methods used for the simulation as well as the results are presented and discussed.

3.1 Clinical particle therapy for lung cancer

Most of the current particle therapy experience for lung tumors comes from irradiations performed at National Institute of Radiological Sciences (NIRS) in Chiba, Japan (Tsujii et al., 2007). Treatments have been conducted using a passive carbon beam delivery system. Recently the first lung tumor treatments with scanned proton beams have been performed. However, tumor sites showing comparably low motion (e.g., upper lung) were chosen (such treatments have been performed at MD Anderson Cancer Center (MDACC)) or patients were under anesthesia (such treatments are conducted at Rinecker Proton Therapy Centre (RPTC) (Eckermann

¹ For LBT beam positions are only adapted in the lateral plane ($\Delta x_i, \Delta y_i$).

et al., 2011)). In both cases, the intrafractional motion has been very low such that treatments could be performed quasi-static.

The treatment planning studies performed in this work are based on a clinical protocol used at NIRS for non-small cell lung cancer (NSCLC). In a phase I/II clinical study the optimal dosage for stage I NSCLC had been found to be 90 Gy (RBE) in 18 fractions over six weeks and 72 Gy (RBE) in nine fractions over three weeks (Miyamoto et al., 2003).

After this initial dose finding study, the efficacy of hypofractionation has been explored. Therefore the number of fractions has been reduced. This work is based on the second of these hypofractionation studies employing four fractions (Miyamoto et al., 2007). Instead of a passive beam delivery, active raster scanning has been simulated.

3.2 Material & methods

3.2.1 4D treatment planning framework

Treatment planning for the scanned carbon beam treatments at GSI Helmholtzzentrum für Schwerionenforschung GmbH (GSI) has been performed using TRiP treatment planning for Particles (TRiP) (Krämer et al., 2000). TRiP was originally developed for stationary tumor treatments but has been extended to 4D functionality based on the work of Bert and Rietzel (Bert and Rietzel, 2007). For clarity in the following if a specific version of TRiP is meant the 3D and the 4D version will be distinguished by their name. The extended 4D version of TRiP will be referred to as TRiP4D while the 3D version will be called TRiP98. TRiP will be used if general aspects are described.

The existing structures in TRiP98, like computed tomography (CT) and treatment plan, were extended from 3D to 4D by introducing a one dimensional array of structures. The number of array members is given by the number of CT states. Other structures are only needed in case of intrafractional motion and thus do not exist for TRiP98. They had to be added. The most important among these new structures are:

Motion In the motion structure the shape of the underlying target motion as well as optionally the motion of surrogate signals is defined. The amplitudes of target and signals are recorded versus time. The signals can be one or multi dimensional.

Spill The spill structure describes the accelerator behavior. For 4D calculations, not only the target motion but also the scanner progress governed by the delivered particle intensity is needed to establish a correlation between beam position and motion state. The spill structure comprises time stamps of different relevant beam delivery events, e.g., beam positions, begin and end of spill extraction, begin and end of iso-energy slices.

MLUT The BT lookup table (MLUT) contains beam adaptation parameters for the lateral as well as the longitudinal direction. For each beam position and each possible motion state defined by the 4DCT adaptation parameters have to be defined.

NLUT The dose compensation lookup table (NLUT) contains base data enabling the calculation of target motion induced dose changes to a beam position. One NLUT implementation has already been described in detail in Section 2.2.1. As already pointed out earlier, the memory requirement of that implementation is rapidly increasing with the number of beam positions. As patient treatment plans can easily comprise thousands or ten thousands of beam positions the NLUT format experimentally used was not usable. Thus, another format had to be implemented. It will be described more thoroughly in Section 3.2.1.

Different functions have been implemented to TRiP4D. The main functional extensions include the distribution of beam positions to the different states of a four dimensional treatment plan according to the particle number, motion, and spill information as well as the dose calculation on all 4DCT states and the subsequent accumulation in the reference CT state. TRiP4D has been implemented by Richter et al. (Richter et al., 2011). BT and RDBT as well as the corresponding calculation and handling of MLUT and NLUT has been implemented in this work.

Optimization of multiple fields

A treatment plan with multiple fields can be optimized in two different modes. Either each field is optimized separately or all fields are optimized simultaneously. In the former case each single field exhibits a homogeneous dose in the target area while in the latter case the single fields might have inhomogeneous dose distributions that only result in a homogeneous cumulative fraction dose if all fields are summed up. For clarity, relative biological effectiveness (RBE) weighted doses in this section are always used with the index "RBE" while the index "absorbed" will be assigned to absorbed doses. If fields are optimized separately, a field dose has to be defined from the fraction dose. For protons, for which a constant RBE of 1.1 is clinically used, the field dose D_{proton}^i can be calculated from the fraction dose $D_{\text{proton}}^{\text{fraction}}$ by dividing the latter by the number of fields n :

$$D_{\text{proton}}^i = \frac{D_{\text{proton}}^{\text{fraction}}}{n}. \quad (3.1)$$

Thus, the division of a proton fraction dose in field doses can be done by dividing the fraction dose by the number of fields. Applying the same formalism to situations where heavy ions, e.g., carbon ions are used, does not work. Because of the dose dependence of the RBE (compare Figure 1.9 on page 23) n superimposed fields with an RBE weighted dose of D_{RBE}^i will not result in a total RBE weighted dose of $n \cdot D_{\text{RBE}}^i$. In this case the calculation of field doses is more complex.

Instead of trying to find an adequate RBE weighted field dose for optimization, the fraction dose can be used for the optimization of n single fields with doses $D_{\text{RBE}}^{\text{fraction}}$. Thus, n fields, typically with different beam angles, are obtained, each optimized to deliver the total fraction dose. This fraction dose is connected to the absorbed dose D_{absorbed}^i via the respective RBE^i (see Equation 1.13 on page 22):

$$D_{\text{RBE}}^i = D_{\text{RBE}}^{\text{fraction}} = \text{RBE}^i D_{\text{absorbed}}^i. \quad (3.2)$$

In the next step, particle numbers of the resulting fields are then scaled with $1/n$ leading to a scaling of the absorbed field doses $D_{\text{absorbed}}^{i,\text{scaled}} = D_{\text{absorbed}}^i/n$. In the following it is shown that the overlay of these n scaled fields yields the desired RBE weighted fraction dose if the overall RBE of the treatment fraction (consisting of the n scaled fields) is sufficiently close to the harmonic mean of the RBE^i of all single fields before scaling. The following equations have to hold for all points of the target volume. Assuming the overlay of all scaled fields yields the fraction dose one can write:

$$D_{\text{RBE}}^{\text{fraction}} \stackrel{!}{=} \text{RBE}^{\text{fraction}} \sum_{i=1}^n \frac{D_{\text{absorbed}}^i}{n}. \quad (3.3)$$

The absorbed field doses can be substituted by the ratio of the RBE weighted dose and the respective RBE: $D_{\text{absorbed}}^i = D_{\text{RBE}}^{\text{fraction}}/\text{RBE}^i$. Thus, Equation 3.3 can be written as:

$$D_{\text{RBE}}^{\text{fraction}} \stackrel{!}{=} \text{RBE}^{\text{fraction}} \frac{D_{\text{RBE}}^{\text{fraction}}}{n} \sum_{i=1}^n \frac{1}{\text{RBE}^i} \quad (3.4)$$

$$\Leftrightarrow \text{RBE}^{\text{fraction}} \stackrel{!}{=} \frac{n}{\sum_{i=1}^n \frac{1}{\text{RBE}^i}}. \quad (3.5)$$

$n/\sum_{i=1}^n (1/x_i)$ is known as the harmonic mean of all x_i . In these treatment planning studies the above dose scaling method has been used. The resulting overall dose of all scaled fields has been calculated by TRiP without motion influence and showed excellent target coverage for all investigated patients. Thus, at least for the investigated patient cohort in conjunction with the chosen dose levels and local effect model (LEM) tables, the overall RBE seems to be sufficiently well represented by the harmonic mean of the unscaled field's RBEs.

Calculation of beam tracking parameters

Calculation of BT parameters has been done according to the method described by Bert and Rietzel (Bert and Rietzel, 2007). Beam adaptation parameters are calculated based on image

registration. While the lateral compensation parameters Δx and Δy are purely geometrical, the longitudinal compensation parameter Δz has to be provided as water-equivalent distance. Thus, for its calculation the geometrical image registration vector has to be combined with the CT information to obtain water-equivalent depth compensation parameters.

One potential issue in calculating BT parameters is the type of registration that is used. Rigid as well as non-rigid registration algorithms exist. Rigid registration algorithms rotate and shift one image to match the other image (e.g., to match an arbitrary CT phase image CT_i to the reference CT image CT_{ref}). As the whole image is transformed (one transformation for all image points) the shape of objects remains unchanged while the position and orientation of objects might change. That means that the distance between two points in the transformed image is exactly identical to the distance between these points in the original image. In contrast, in non-rigid transformations each image point has a different transformation. Thus, deformations can be described. Consequently, the distance of two image points in the transformed image might differ from the distance of these image points in the original image. The difference is illustrated in Figure 3.1.

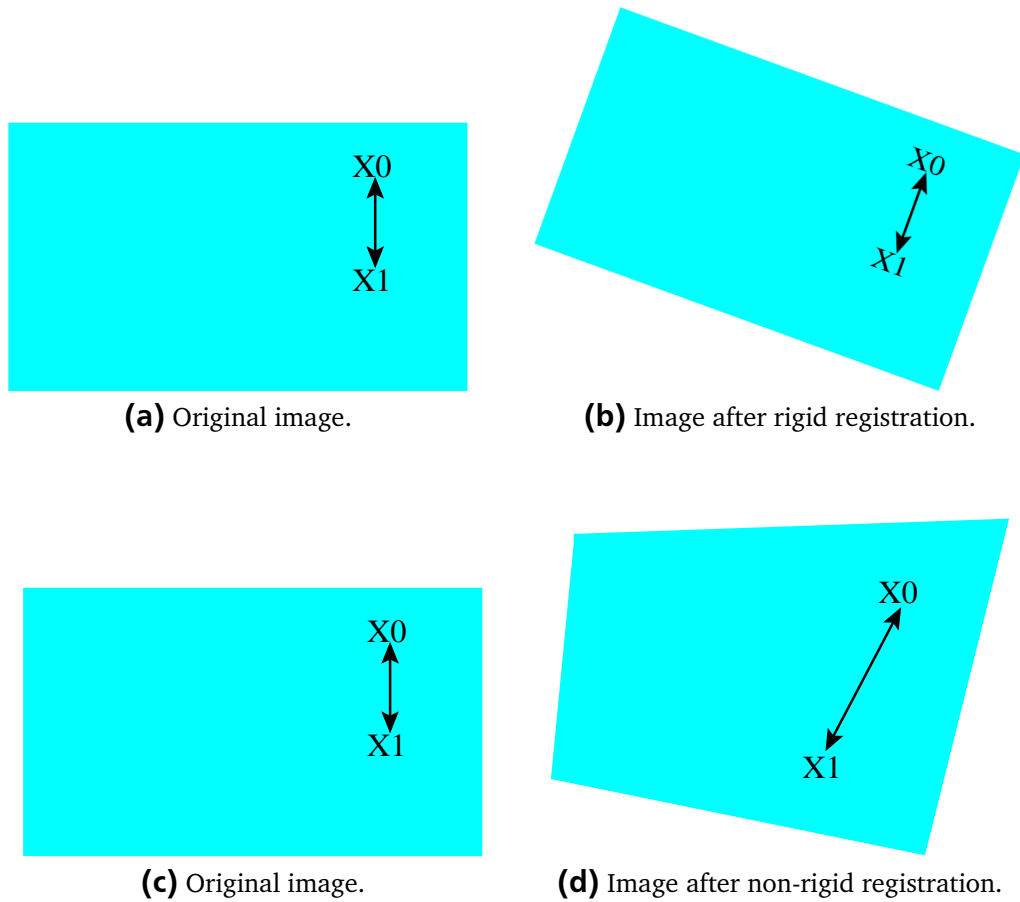


Figure 3.1.: Illustration of rigid and non-rigid image registration. While rigid registration conserves shape and point to point distances, in case of non-rigid registration the shape of objects can change and point to point distances are not conserved.

Treatment plans in scanned particle therapy are optimized for a homogeneous dose distribution assuming a predefined beam position spacing. If non-rigid registrations are used to calculate BT parameters, the distance between beam positions is not preserved. Rigid registrations, in contrast, preserve the distance between image positions and thus the distance between beam positions is preserved. In Figure 3.2 this effect is shown in one dimension. Grid spacing is 2mm and full width at half maximum (FWHM) of the Gaussian shaped spots is 6mm. A ratio of about three between FWHM and grid spacing is typically chosen in TRiP (Krämer and Scholz, 2000). For the rigid transformation, nominal raster position distances are preserved while small deviations are introduced in case of the non-rigid registration. The overall dose in case of the non-rigid registration shows inhomogeneities that are not present in case of the rigid registration.

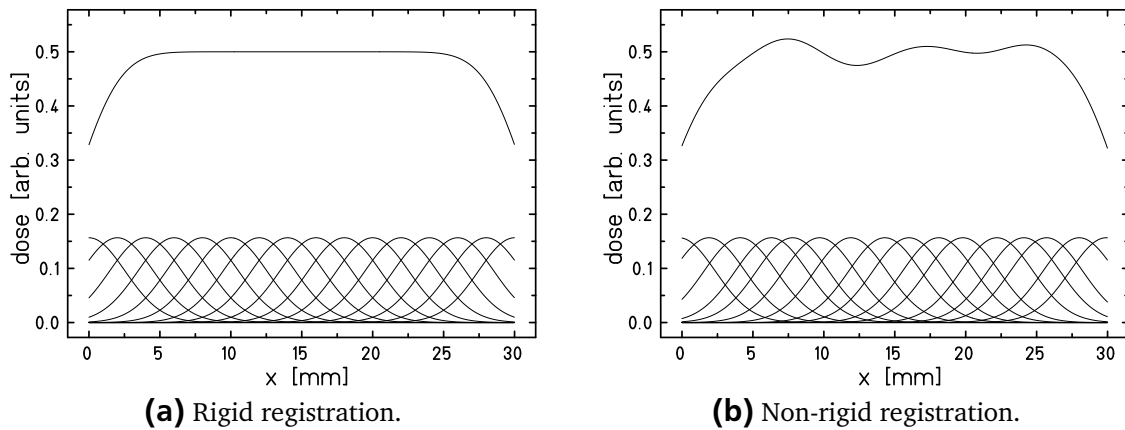


Figure 3.2.: Illustration of dose distribution in case of rigid and non-rigid image registration. While rigid registration conserves point to point distances, in case of non-rigid registration the point to point distances are not conserved. This can result in dose inhomogeneities due to changing overlap parameters compared to treatment planning. The single spot contributions as well as the overall dose are shown in both cases.

The tumor motion is in many cases best represented by non-rigid registration. But even if the BT parameters are calculated using rigid registration, the 4D dose calculation can still be based on a potentially more accurate non-rigid registration. Beam position distances are only conserved within one motion state. But as the number of motion state changes typically is small against the number of beam positions, the effect from changing motion states is expected to be comparably low.

A low memory consumption NLUT

The main requirement for the new NLUT format was to achieve reasonable file sizes, even if treatment plans with ten thousands of beam positions have to be dealt with. To be independent of the number of beam positions, no direct dose contributions from one beam position to an-

other beam position are stored. Instead, base data are provided that allow calculation of dose contributions in real-time.

In the analytical beam model used in TRiP dose deposition of a given particle beam can be calculated at any position knowing the beam's depth dose distribution (E, z) , its radial shape, here parameterized with a Gaussian distribution with variance σ , and the delivered number of particles N (Krämer et al., 2000):

$$D(E, r, z) [\text{Gy}] = 1.6 \cdot 10^{-8} d(E, z) \left[\frac{\text{MeV cm}^2}{\text{g}} \right] \frac{N}{2\pi\sigma^2 [\text{mm}^2]} \exp\left(-\frac{r^2}{2\sigma^2}\right), \quad (3.6)$$

where z and r denote the positions water-equivalent depth and the radial distance from the beam axis, respectively.

The new NLUT implementation contains for each iso-energy slice (IES) the corresponding focus setting of that IES and the depth dose distribution normalized to one particle. The latter has been interpolated to avoid the necessity for interpolation during beam application. The central task of dose compensation is calculation of dose differences between actual and nominal dose deposition (see Equation 2.1 on page 55). The actual dose deposition is influenced by target motion, BT, and particle number adaptation. Provided with the depth dose distribution for each beam the dose deposition normalized to one particle $D_{\text{norm}}(E, r, z)$ can be calculated at any position. The actual dose difference $\Delta d_{m(i)}^{ik}$ can then be calculated during beam delivery:

$$\Delta d_{m(i)}^{ik} = D_{\text{norm}}\left(E^i, r_m^k, z_m^k\right) \Big|_{\vec{x}_m^i + \Delta \vec{x}_m^i} \cdot N_{\text{adapt}}^i - D_{\text{norm}}\left(E^i, r_{\text{ref}}^k, z_{\text{ref}}\right) \Big|_{\vec{x}_m^i} \cdot N_{\text{nom}}^i, \quad (3.7)$$

where r_m^k and z_m^k are the radial distance and water-equivalent depth of beam position k in motion state m , the index term is a reminder that the relative position of beam position k has to be calculated with respect to a beam position \vec{x}_m^i , taking into account the position adaptation vector $\Delta \vec{x}_m^i$ from BT. $D_{\text{norm}}(E, r, z)$ is the dose normalized to delivery of one particle and is calculable from the parameters provided in the new NLUT format. The nominal particle number N_{nom}^i is derived from the treatment plan, while the actually delivered particle number N_{adapt}^i can be calculated during beam delivery according to Equation 2.5 on page 56.

As pointed out in Section 2.2.2, in the old NLUT format the size of the table was below 448 MB for treatment plans up to 3064 beam positions when 25 motion states were used. The new implementation produces NLUT tables with a size around 1 MB if the resolution for the depth dose distribution is set to 0.1 mm. Furthermore, the NLUT size no longer depends on the number of beam positions or motion states. Thus, the table size does not increase if, e.g., a finer grid spacing or more motion states are used. Besides resolution, the size only depends on the number of IESs, used in the treatment plan. On the other hand, the computational load for the

real-time calculation of dose differences is increased as dose distributions are not provided in a precalculated table but have to be calculated from the base data.

Spill simulation

Important parameters entering the spill simulation are the spill's length, its shape, and the particle intensity. All these parameters have been based on the GSI accelerator parameters. The spill length is 2.2 s, spill pause is 3.2 s when an energy change is required and 2.2 s without energy change. The spill shape has been approximated by a Gaussian function. 15 different particle intensity steps are available providing between 2×10^6 particles/spill and 2×10^8 particles/spill. The intensity step is automatically chosen from the treatment plan. If beam positions with a low particle number are present in an IES, a lower intensity is chosen for that IES to guarantee technical applicability of the treatment plan.

3.2.2 Simulation input data

4DCT data

Five lung cancer patients entered this study. 4DCT data have been recorded at MDACC in Houston, Texas, USA. The clinical target volumes (CTVs) covered a range from 45 cm^3 to 236 cm^3 . The motion amplitudes in the direction of the largest motion component were from 1 mm to 25 mm. The 4DCTs consist of ten motion states each. Time based state definition has been used. Thus, all CT states represent an equally long time span. Contours of the gross tumor volume (GTV), the CTV, and several organs at risk (OARs) are drawn on the reference motion state CT image. Patient data are summarized in Table 3.1.

Table 3.1.: CTV size, motion in the direction of the largest motion component, and contoured OARs for all investigated patients.

patient no	CTV size	largest motion	contoured OARs
1	236 cm^3	5 mm	carina, esophagus, heart, spinal cord, vertebral bodies
2	160 cm^3	20 mm	esophagus, heart, spinal cord
3	123 cm^3	1 mm	carina, esophagus, heart, spinal cord
4	45 cm^3	5 mm	esophagus, heart, spinal cord
5	125 cm^3	25 mm	carina, esophagus, heart, spinal cord

Image registration

Rigid as well as non-rigid image registrations have been performed. Rigid registration has been performed by an in-house tool. Non-rigid registration has been performed applying the Plastimatch code (Shackleford et al., 2010).

Treatment plan parameters

Like in the clinical setup used at NIRS, four beam entrance portals have been used. In contrast to the NIRS treatments where one portal has been used per fraction in this study all four portals are used for every fraction. At NIRS a horizontal and a vertical beam is used. For both beams the couch is tilted by $+20^\circ$ and by -20° , respectively, resulting in four treatment portals in total. A horizontal beam is represented by a gantry angle of 0° in TRiP while a gantry angle of -90° represents a vertical beam. Thus, in TRiP the clinical entrance portals are realized by gantry angles of $+20^\circ$, -20° , -70° , and -110° . For patient 2 a gantry angle of -110° would result in a treatment field partly traversing the heart. Besides elevated dose delivery to the heart this beam portal is also technically very unfavorable as it implies the need for very large beam energy adaptation. They are caused by the large density gradient between heart and lung tissue. The resulting difference in water equivalent path length has to be compensated by the BT system. For patient 2 a gantry angle of -50° has been used instead of -110° .

For the simulations the RBE weighted dose has been evaluated. It is calculated with TRiP according to LEM (see Section 1.2.1). The most recent version of LEM has been used (Elsässer et al., 2010; Friedrich et al., 2012). As introduced in Section 1.2.2, tumor cells and normal tissue typically exhibit a differential α/β ratio. As input $(\alpha/\beta)_{\text{CTV}} = 6 \text{ Gy}$ ($\alpha = 0.021 \text{ Gy}^{-1}$, $\beta = 0.0035 \text{ Gy}^{-2}$, $D_t = 10 \text{ Gy}$) has been chosen for the CTV tissue (Friedrich, 2011). This value is close to the α/β ratio of 5.585 Gy used by Kanai et al. for NSCLC (Kanai et al., 2006). Normal tissue typically has a lower α/β ratio (see Section 1.2.2). In this work $(\alpha/\beta)_{\text{norm}} = 2 \text{ Gy}$ ($\alpha = 0.3 \text{ Gy}^{-1}$, $\beta = 0.0015 \text{ Gy}^{-2}$, $D_t = 22 \text{ Gy}$) has been assigned to all tissues but the CTV. This value has been based on results from carbon irradiation of the spinal cord of rats (Karger et al., 2006).

Treatment plans have been optimized to homogeneously cover the CTVs. The TRiP "all points" algorithm has been used for calculation of absorbed dose, while the low dose approximation (Krämer and Scholz, 2006) was used for biological dose calculation. Grid spacing of the treatment plans has been chosen to be 3 mm in x - as well as in y -direction. Spacing between IESs has been set to $3 \text{ mm}|_{\text{H}_2\text{O}}$ and a 3 mm ripple filter (Weber and Kraft, 1999) has been used. Energy adaptation systems comparable to those installed at GSI (Saito et al., 2009) introduce material proximal to the patient. As the investigated techniques BT and RDBT require energy adaptation, a bolus of $56.8 \text{ mm}|_{\text{H}_2\text{O}}$ has been inserted proximal to the patient.

Fractionation scheme

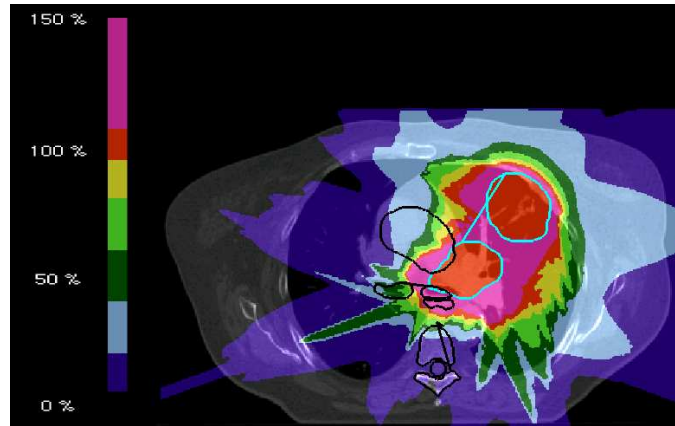
The NIRS fractionation scheme employing four fractions has been chosen (Miyamoto et al., 2007). At NIRS the fraction dose was 13.2 Gy (RBE) for Ia staged tumors and 15 Gy (RBE) for Ib staged tumors. It is known that the approach for RBE calculation used for carbon therapy at NIRS and the LEM based approach used at GSI yield different results (Steinsträter et al., 2011). Thus, for this study the fraction dose has been derived from tumor control probability curves calculated from the data reported from NIRS. For four fractions a RBE weighted dose of 8.2 Gy (RBE) per fraction has been obtained (Friedrich, 2011). This value has been used in this study for all patients. Single treatment fields have been optimized using the method described in Section 3.2.1. Thus, all four fields have been optimized for a target dose of 8.2 Gy (RBE) each and particle numbers have subsequently been divided by four. Nominal dose distributions for all patients are shown in Figure 3.3 on the facing page.

Motion trajectory

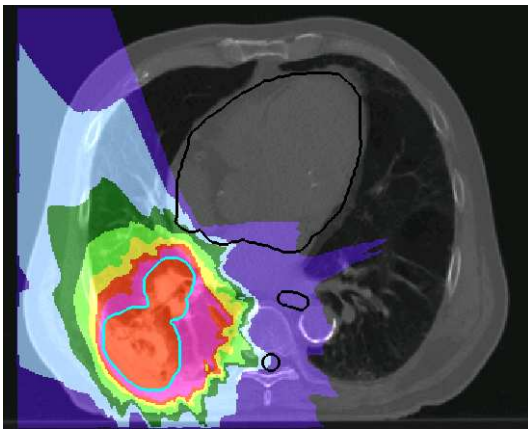
A sinusoidal motion trajectory has been used. Two different approaches can be employed for motion state detection. For phase-based motion detection and perfectly periodic motion traces the exact shape of the motion trajectory does not matter because the motion state definition is done in the time domain. In contrast, for amplitude based motion the shape of the motion is important for the motion state definition. An example for both state division methods comparing a sinusoidal and a Lujan type motion (Lujan et al., 1999) is shown in Figure 3.4 on page 80. The same state definition method used for the reconstruction of the 4DCTs should be used in simulations. As the 4DCTs used in this study have been reconstructed based on the time domain, phase-based motion detection has also been used for the simulations.

To account for the possible changes in patient motion patterns, different periods (2 s, 4 s, and 6 s) as well as different starting phases (0° , 90° , 180° , and 270°) have been chosen. Motion changes within the application of one field have not been considered in this study. Within one fraction the motion period has been kept constant while the starting phases have been changed. Four different combination of starting phases for the four fields of one fraction (gantry angles $+20^\circ$, -20° , -70° , and -110°) have been used:

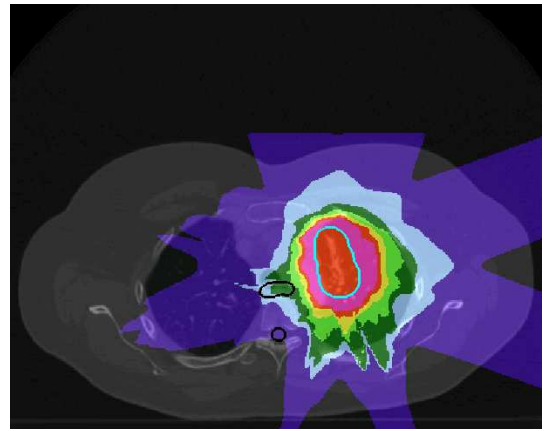
- 0° , 90° , 180° , and 270° ,
- 90° , 180° , 270° , and 0° ,
- 180° , 270° , 0° , and 90° , and
- 270° , 0° , 90° , and 180° .



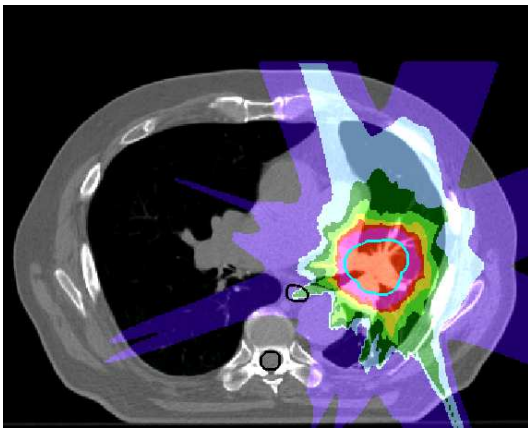
(a) Patient 1.



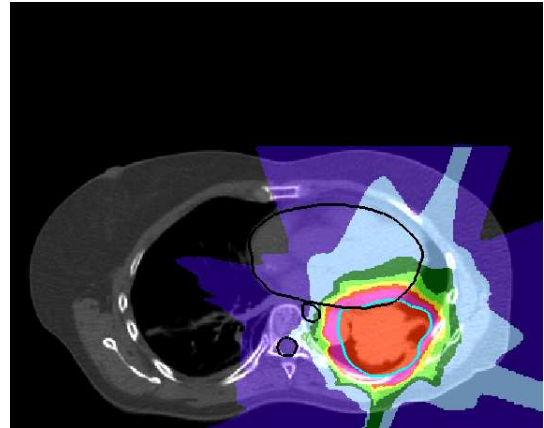
(b) Patient 2.



(c) Patient 3.

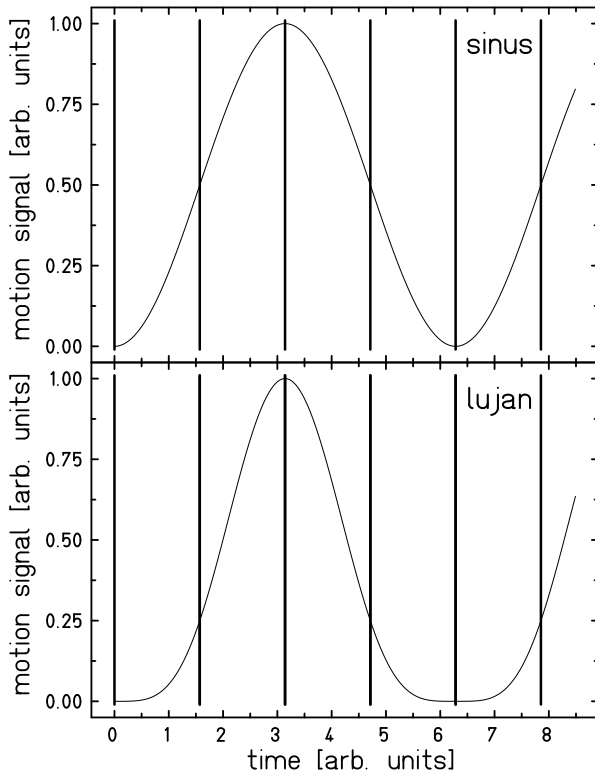


(d) Patient 4.

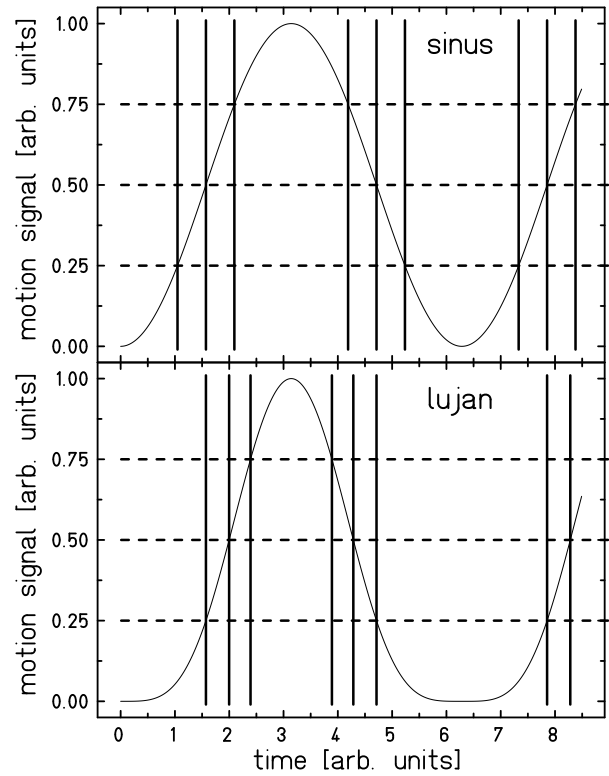


(e) Patient 5.

Figure 3.3.: Dose cuts of the nominal dose distributions for all five patients. The CTV served as target contour and is outlined in cyan. OARs are outlined in black. For some patients they partly overlap with the CTV. For patient 2 a gantry angle of -110° (with respect to the horizontal axis) for the fourth field would have resulted in traversing the heart. This has been avoided by choosing a gantry angle of -50° for the fourth field. The tissue directly adjacent to the CTV receives a dose level above the nominal fraction dose (pink areas). This can be explained when taking the differential α/β ratios of CTV and normal tissue into account.



(a) Phase based motion states.



(b) Amplitude based motion states.

Figure 3.4.: Phase based (Figure 3.4a) versus amplitude based (Figure 3.4b) motion state definition. For clarity only four motion states have been defined. Two simple periodic motions, a shifted and stretched sinus function and a Lujan type (\sin^4) function, have been chosen. In the phase based approach motion state determination is done based on the phase information (vertical lines). In the amplitude based approach the state is determined based on the motion amplitude (horizontal dashed lines). For clarity resulting motion state changes are again indicated by vertical lines. While in the phase based approach for this perfectly periodic motion the state definition over time does not depend on the shape of the motion, for the amplitude based approach there is a difference in state definition depending on the motion shape.

Both limitations in period and starting phases are artificial and many more combinations are possible. But this parameter choice is thought to reasonably cover the expected parameter space of a patient and thus be sufficient to show the range of possible dosimetric results when applying different motion mitigation techniques.

3.2.3 Analysis

The measures D_x and V_x are used to judge a dose distribution:

D_x : $x\%$ of the volume under consideration has received a dose of at least D_x ,

V_x : A dose of at least $x\%$ of the target dose has been received by the volume V_x .

For comparison of the different motion mitigation techniques, the V_{95} and the V_{107} of the CTV have been analyzed as a measure for target coverage and overdose of the CTV, respectively. This choice has been based on the ICRU recommendations (ICRU, 1993a). As an indicator for the homogeneity, the width of the dose fall-off has been assessed by evaluating the difference $D_5 - D_{95}$. The evaluation of these measures is exemplary shown in Figure 3.5 on the following page.

All measures have been evaluated for all four beam application techniques (interplay, LBT, BT, and RDBT). For each beam technique, like mentioned in Section 3.2.2, twelve motion parameters (four starting phases and three amplitudes) are simulated. Additionally, two different registration algorithms (rigid and non-rigid) are employed for dose calculation, while the MLUT calculation for all cases relies on rigid registration (see Section 3.2.1). Thus, in total 96 fraction dose distributions are simulated per patient.

For the calculation of cumulative treatment course doses four fraction doses have been added according to the linear-quadratic-linear model (compare to Section 1.2.1). Each of the four motion starting phases has been assigned to one fraction. Taking into account three different motion periods a total of $3^4 = 81$ combinations have been evaluated for each of the four beam delivery techniques and each of the two registration methods.

For each measure mean and standard deviation over all motion parameters are calculated per patient for fraction dose distributions as well as for cumulative treatment course dose distributions. Results for dose calculation based on the rigid and the non-rigid registration algorithm are reported separately. The mean values of all measures have been investigated for significant differences between different beam application techniques. The Tuckey-Kramer test at 5% significance level has been used.

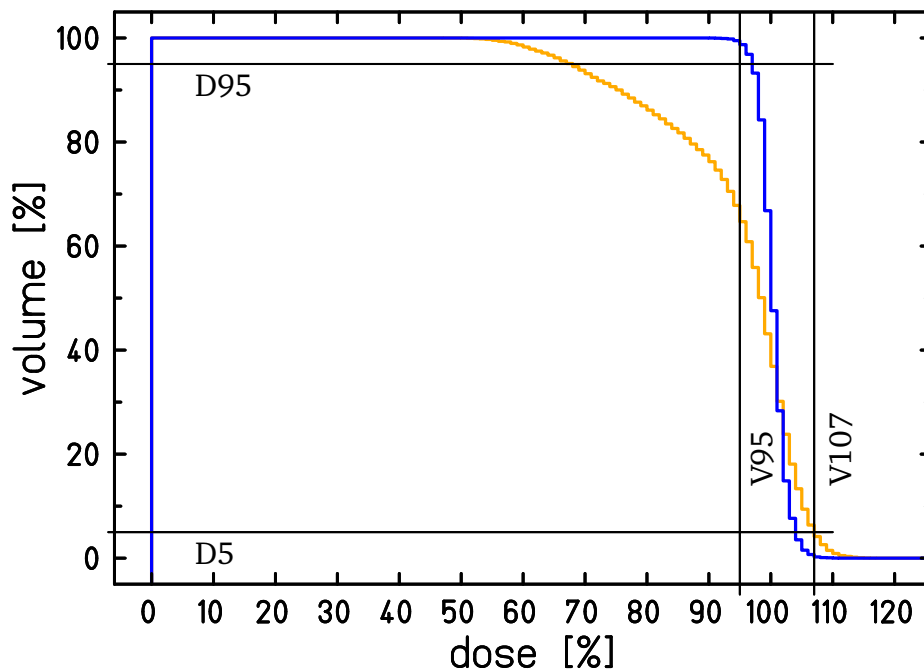


Figure 3.5.: Example of the analysis of V_{95} , V_{107} , and $D_5 - D_{95}$ comparing two different DVHs. The V_{95} and V_{107} are the volumes at the intersection of the vertical lines (at 95% and 107% dose level, respectively) and the according DVH curve. For the orange DVH $V_{95} = 64.7\%$ and $V_{107} = 4.2\%$, for the blue DVH $V_{95} = 98.7\%$ and $V_{107} = 0.2\%$. The D_5 is the dose at the intersection of the horizontal line at 5% volume level and the DVH curve. Accordingly, the D_{95} is the intersection of the horizontal line at 95% volume level and the DVH curve. The difference between these dose levels is the $D_5 - D_{95}$. For the orange DVH $D_5 - D_{95} = 39\%$ and for the red DVH $D_5 - D_{95} = 7\%$.

3.3 Results

Representative dose distributions for all techniques (motion period 4s, motion starting phases 0°, 90°, 180°, and 270°, rigid registration) for patient 5 are shown in Figure 3.6 on the next page.

Dose distributions for the other patients are shown in Figures A.1 to A.4 in the appendix.

The results of the V_{95} analysis are shown in Figure 3.7 on page 85. The mean values and standard deviations (SDs) of the V_{95} value for all patients are summarized in Tables A.1 to A.8 in the appendix. An overview concerning the significances in the differences of V_{95} for all application techniques is also provided there.

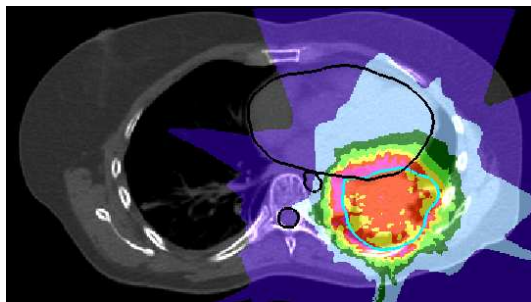
For all investigated patients the V_{95} is larger if BT or RDBT are used compared to interplay and LBT. Except for one case, when fraction doses based on non-rigid calculation are compared for RDBT and LBT, the mean values have been significantly better. The mean V_{95} values for the fraction dose were between 92.9% and 99.5% (90.5% to 97.6% for non-rigid registration) for BT and between 94.6% and 99.2% (86.8% to 97.1% for non-rigid registration) for RDBT. Significant differences between BT and RDBT in the V_{95} for the fraction doses could be observed only for non-rigid registration where BT performed significantly better for patients 2 and 3. For all investigated patients the mean V_{95} after a complete treatment course is at least at 95% (90.5% for non-rigid registration) when BT or RDBT are used. For the patients 1 and 3 also interplay and LBT show V_{95} values above that threshold. In contrast, for the patients 2, 4, and 5 the V_{95} drops if interplay or LBT are employed.

The V_{107} values for all investigated techniques are shown in Figure 3.8 on page 86. The mean V_{107} values and their SDs for all patients are summarized in Tables A.9 to A.16 along with the analysis results from significance analysis.

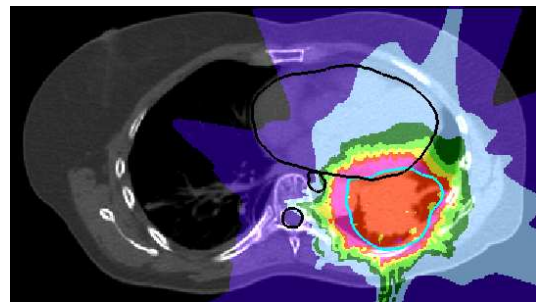
All application techniques show very low V_{107} values for patient 3. This patient shows only little tumor motion. In most of the cases, BT and RDBT perform significantly better than the other techniques. Especially conspicuous are the results for patient 2. V_{107} values for BT are significantly worse than for all other techniques for this patient. Although RDBT relies on the same position adaptation like BT, overdoses are significantly lower for RDBT compared to BT and all other application techniques.

The V_{107} after the complete treatment course are all below 3%, often even close to 0% except for patient 2 when treated with BT. For patients 1, 2, and 5 RDBT reaches significantly lower V_{107} than BT for a full treatment course.

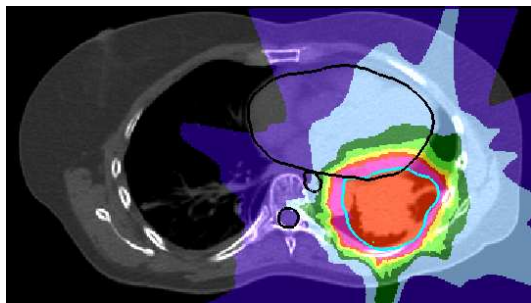
The $D_5 - D_{95}$ values for all investigated techniques are shown in Figure 3.9 on page 87. The mean values and SDs of the $D_5 - D_{95}$ values are summarized in Tables A.17 to A.24 in the appendix. Information about the significances of the differences between the investigated delivery techniques can also be found there.



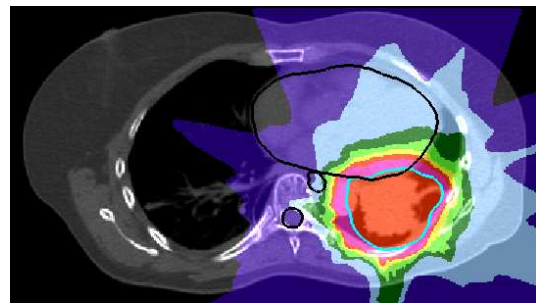
(a) Interplay.



(b) lateral beam tracking.



(c) Beam tracking.



(d) RDBT.

Figure 3.6.: Dose distributions for all four application techniques in patient 5. Cuts are drawn through iso-centre. Motion period of 4 s and motion starting phases of 0° , 90° , 180° , and 270° have been used. Dose calculation has been based on rigid registration. An improved homogeneity for BT and RDBT compared interplay and LBT can already be seen in these cuts.

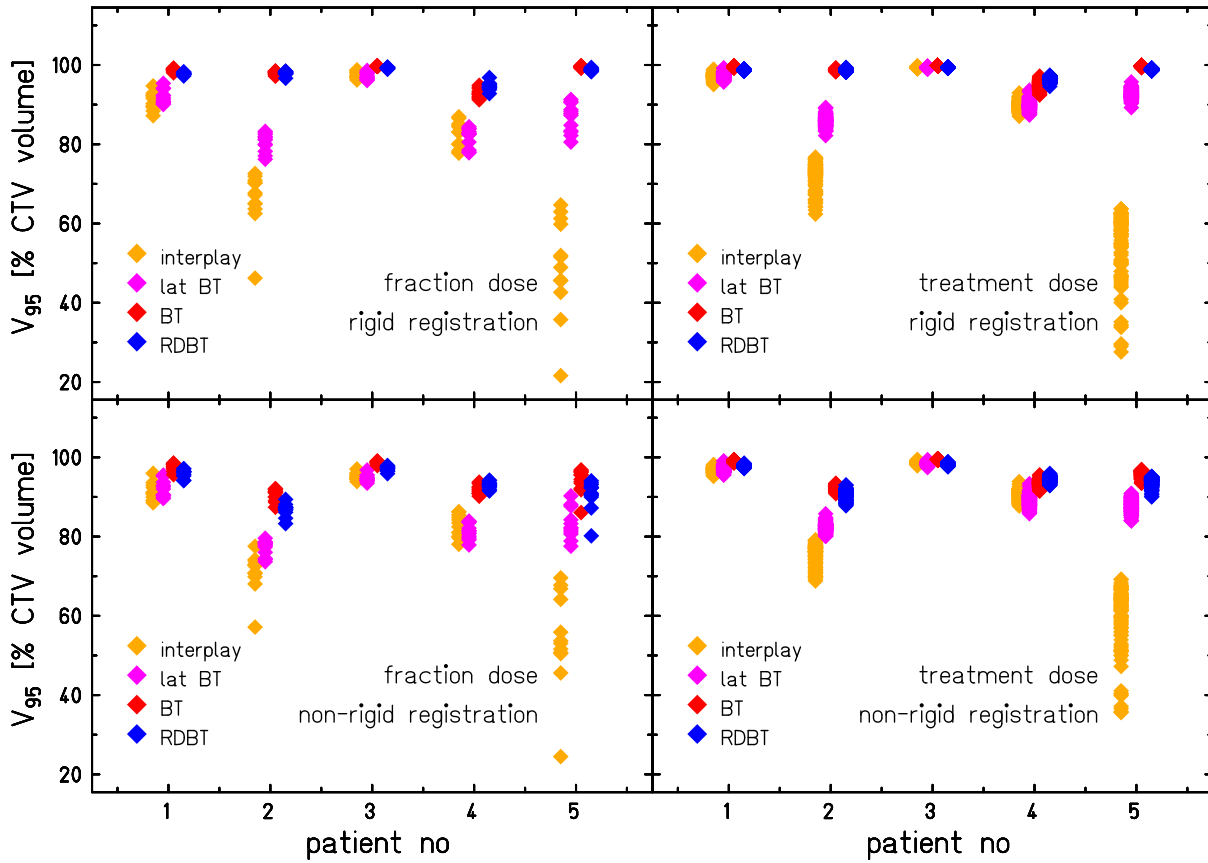


Figure 3.7.: V_{95} value as a measure for dose coverage of the CTV for rigid registration based dose calculation. Results for fraction dose and dose from a complete treatment course are shown separately. Also results from dose calculation based on rigid and non-rigid registration, respectively, are shown in different figures.

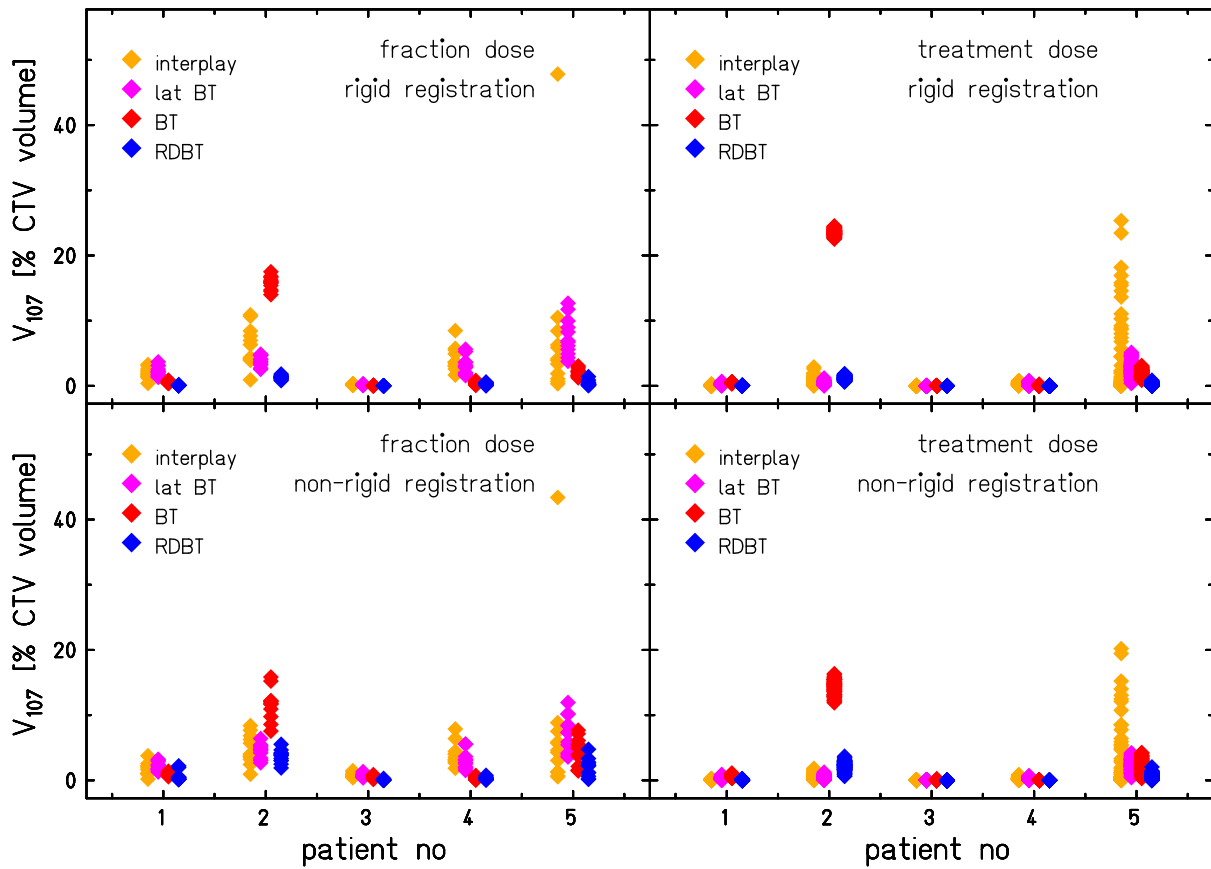


Figure 3.8.: V_{107} value as a measure for overdoses of the CTV. The V_{107} spread for BT is comparably low except for patient 2 where BT produced very pronounced overdoses. Only RDBT shows comparably low values for all patients and motion patterns.

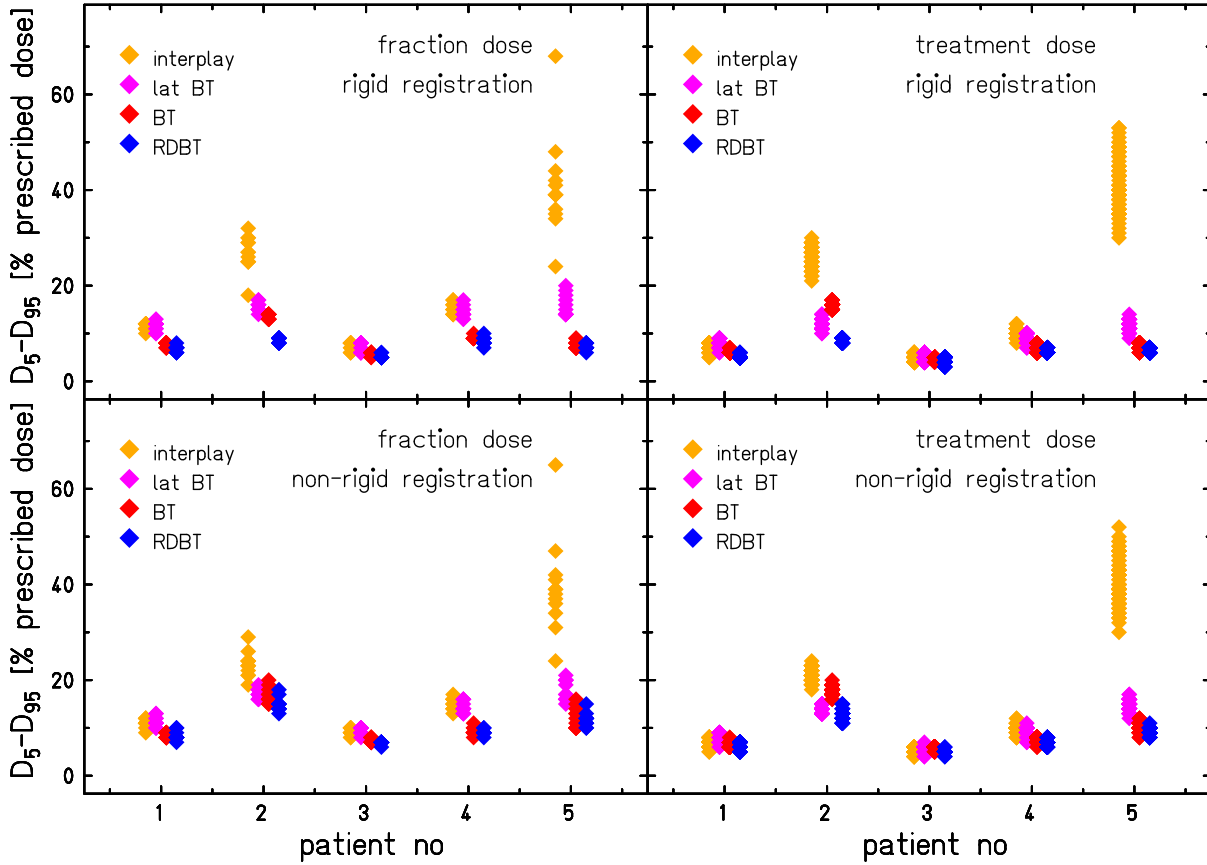


Figure 3.9.: $D_5 - D_{95}$ value as a measure for homogeneity of the CTV dose coverage. A small $D_5 - D_{95}$ indicates a steep DVH fall-off and thus a homogeneous dose distribution. The $D_5 - D_{95}$ for interplay and lateral BT strongly depends on the patient and its individual motion. BT and RDBT show a greater robustness against different patient characteristics.

The steepness of the dose volume histograms (DVHs), assessed by their $D_5 - D_{95}$ value, showed significantly lower values for RDBT than for interplay and LBT for all patients in all but one case (patient 3, rigid registration, complete treatment course). Also BT performed significantly better than LBT and interplay in most patients. RDBT significantly outperformed BT for patients 1, 2, 3, and 4 if doses for the complete treatment course are analyzed.

Results for the ranges of mean and maximal dose deposited to the OARs are shown in Tables A.25 to A.44.

3.4 Discussion

In this treatment planning study, the motion mitigation techniques LBT, BT, and RDBT have been compared for the treatment of lung tumors. For comparison, beam application without application of motion mitigation, i.e., interplay, has been simulated in addition. Rigid as well as non-rigid registrations have been used for dose calculation. Rigid registration has in both cases been used for the MLUT calculation to maintain the distance between beam positions after application of position adaptation. For direct comparison of the motion mitigation techniques, the simulations employing rigid registration are best suited as the results are not biased by different image registration algorithms used for beam application (via the MLUT) and dose calculation. Using the non-rigid registration for dose calculation offers some insights in the robustness of all MLUT related techniques (i.e., LBT, BT, and RDBT). Deviations between the rigid and the non-rigid registration algorithm impair the validity of the MLUT. This might be comparable to a clinical scenario where imperfect registrations will be a potential concern. However, for a direct comparison the quantitative differences between the algorithms would have to be assessed.

Prerequisite for the application of RDBT was a substantial reduction of the NLUT file size. Thus, a new NLUT format has been implemented. File size was dramatically reduce and is now in the order of MB. However, while minimizing the file size, the computational load for the real-time calculation of dose differences has been increased. The current therapy control system (TCS) at GSI is not fast enough to reliably perform the required dose calculations for typical irradiation speeds of some ms per beam position. However, the implementation has been optimized for the use in TRiP where operations are not time critical. It is expected that a dedicated implementation optimized for real-time performance can be fast enough for the application in the TCS.

Dose levels in the healthy tissue very close to the CTV exceed the prescribed dose. This can be understood if taking the differential α/β ratio into account.

Results after one fraction show that BT and RDBT typically exhibit superior values for V_{95} , V_{107} , and $D_5 - D_{95}$ compared to interplay and LBT. Patient 2 showed rather large overdoses when BT was used. The V_{107} was significantly worse for BT compared to all other application

techniques. As also LBT produces less overdose than BT, the overdoses are likely to be connected to the depth compensation. This patient exhibits two GTVs. A common CTV encompassing both GTVs was drawn in some slices. Overdoses were mainly apparent in the area between the GTVs. The transition between relatively dense GTV tissue and the lung tissue positioned centrally within the CTV for this patient might be challenging to handle for BT. Van de Water et al. simulated BT on heterogeneous phantoms and found that BT can produce dose inhomogeneities for heterogeneous targets (van de Water et al., 2009). The question if these results would also occur in patients could not be answered in their study. Patient 2 might be such a case due to the density gradient within the CTV and the observed overdoses might be comparable to the results reported by van de Water. However, as also patient 1, 3, and 4 have multiple GTVs and BT copes much better with that patients, the density gradients do not seem to be the only reason for the bad performance of BT. It is striking that RDBT, using the same MLUT that BT uses, copes very well with patient 2. This emphasizes the advantages of a closed-loop system. Overdoses can be detected by RDBT and particle numbers can be reduced for the respective beam positions. Although further patients showing similar anatomy should be analyzed first, this might be a hint that treatment volumes encompassing large density gradients can compromise the dose distributions obtained by BT.

For a complete treatment course consisting of four fractions BT and RDBT yield V_{95} values above 95% (above 90% for dose calculation based on non-rigid registration) for all patients. BT tends to show higher V_{95} when compared to RDBT. A study by Bert also compared different motion mitigation techniques for the treatment of lung cancer with carbon ions (Bert, 2006). Absorbed dose has been investigated. The V_{95} values for BT reported by Bert are worse than the ones obtained in this study. Mean V_{95} values as low as 75.7% have been reported for one patient. RDBT has been proposed to improve target coverage. A possible explanation for these different results might be the number of fields applied. While four fields have been used in this study one field was used by Bert. Knopf et al. reported more favorable dose distributions when more treatment fields were used for *re-scanning* (Knopf et al., 2010). It can be expected that dose deviations from the nominal treatment dose are also reduced for other beam application techniques when more fields are applied. While target coverage using BT in this study was already very good and no additional improvement could be observed when using RDBT, improvements from using RDBT when compared to BT were the reduction of overdoses assessed by the V_{107} value and the improved dose homogeneity assessed by the $D_5 - D_{95}$ value. When analyzing a complete treatment course both values were for most patients (3/4 for V_{107} , 4/5 for $D_5 - D_{95}$) significantly better when RDBT was used. These values have not been explicitly assessed in the study by Bert. However, from the DVHs shown, a clear trend to increased overdoses is apparent in that study. This trend disagrees with the result from this work. Besides the above mentioned differences in study design, also the differences in the implementation of RDBT itself might be a reason for the different results obtained.

This study also showed the importance of the energy adaptation. LBT results were often significantly worse than BT results. On the other hand patient 3 exhibiting only very small target motion showed comparably good results for LBT and even interplay. A subset of lung tumors might thus be treatable without motion mitigation. Also the combination of RDBT and LBT instead of BT might be an option worthwhile for investigation.

So far the real-time dose change calculation performed by RDBT considers absorbed doses only. Nevertheless results are often superior to BT even if biological dose calculation is assessed, as in this treatment planning study. This might be partly due to the fact that RDBT calculates overall dose changes relative to the nominal dose (see Section 2.2.1). In this relative quantity the effect of biological dosimetry is expected to partly cancel out. However, considering the nonlinear relationship between absorbed dose and biological dose, there will be a remaining error introduced and implementation of biological dosimetry might further improve RDBT performance. If taking into account the results from the experimental assessment of RDBT (see Chapter 2) where also underdoses could be significantly reduced, one might speculate that also the V_{95} values obtained by using RDBT would be superior to the ones obtained by BT when biological dosimetry would be included into RDBT.

Analysis of robustness of all motion mitigation techniques was not within the scope of this work. However, the results based on non-rigid registration for dose calculation and rigid registration for MLUT calculation might provide a glance on robustness of motion mitigation techniques. Quantitative analysis of the differences introduced by the different registration techniques and subsequent comparison to registration uncertainties expected in clinical radiotherapy would be needed. However, at least with the registration uncertainties introduced in these studies, BT and RDBT were still typically significantly better than interplay and LBT. Also significantly better performance of RDBT compared to BT especially in the V_{107} and $D_5 - D_{95}$ was still measured when non-rigid registration was used. However, dedicated treatment planning studies taking into account realistic uncertainties are indispensable to judge the robustness especially of very sophisticated techniques like BT and RDBT.

4 Dose compensated re-scanning

In the preceding chapters *real-time dose compensation* was always used in conjunction with *beam tracking* (BT) but this is not compulsive. In this chapter, a new method, called *real-time dose compensated re-scanning* (RDRS), is proposed. *Real-time dose compensation* is combined with several re-scans. Lateral or full BT can optionally be included.

Contents

4.1. Material & methods	92
4.1.1. Methodology	92
4.1.2. Measurements	94
4.1.3. Simulations	95
4.2. Results	95
4.2.1. Measurements	95
4.2.2. Simulations	99
4.3. Discussion	100

Different motion mitigation techniques are available with individual advantages and disadvantages. As tumor motion shows a large inter-patient variability it is likely that not only one motion mitigation technique turns out to be the universal solution but different patient and tumor characteristics demand different approaches. The introduced motion mitigation techniques *rescanning*, *gating*, and BT (with or without *real-time dose compensation*) can not only be used separately but might be combined. Combinations of these techniques can be superior compared to the application of one technique and some combinations have already been proposed in the literature. Van de Water et al. simulated BT with protons and concluded that proton BT should be combined with *re-scanning* to improve the method's robustness against uncertainties (van de Water et al., 2009). Furukawa et al. proposed a combination of *gating* and *re-scanning* for the treatment of moving tumors (Furukawa et al., 2010a). A clinical BT implementation should be combined with *gating* to trigger beam pauses in case unexpected motion, e.g., due to coughing, is detected (Bert and Durante, 2011).

Beam delivery techniques including re-scans are known to improve robustness (van de Water et al., 2009). But the application of RDRS possibly offers advantages beyond increased robustness. If employed without full BT, RDRS can be used to compensate also for dose changes that occur due to the lack of full BT. In this case, dose deposition is not only altered by nontranslational motion components but also by a lack of full Bragg peak position adaptation.

While lateral *beam tracking* (LBT), i.e., beam position adaptation only in the lateral plane ($\Delta x_i, \Delta y_i$), can be technically realized using the existing scanner magnets and a dedicated control software, longitudinal BT is technically more challenging and currently requires additional hardware, e.g., the double wedge system employed at GSI Helmholtzzentrum für Schwerionenforschung GmbH (GSI) (Saito et al., 2009). This in-room device is due to the need for additional hardware in the treatment room and the introduction of passive material in the beam proximal to the patient no a favorable clinical solution. Alternative solutions adapt the beam energy inside the beam line (Chaudhri et al., 2010). RDRS can be used together with LBT. The main motion direction should be in the lateral plane thus LBT can cover most of the motion influence. The missing depth compensation including the influence of nontranslational motion is compensated by RDRS.

RDRS functionality has been implemented at the GSI therapy control system (TCS) as well as in TRiP4D. Film measurements assessing RDRS in two dimensions as well as simulations for three dimensional treatment plans have been conducted and are described in the following sections.

4.1 Material & methods

4.1.1 Methodology

RDRS relies, like *real-time dose compensation combined with beam tracking* (RDBT), on real-time calculation of dose deviations between nominal dose and actually delivered dose. Thus, also for RDRS base parameters for the calculation of dose changes need to be precalculated. Calculation of dose compensation parameters D_m^{ik} for RDRS is with some adaptations done according to the method outlined in Section 2.2.1. For RDBT the dose contributions D_m^{ik} from a beam position i to another beam position k in a motion state m are calculated taking the target in motion state m as well as BT position adaptations $\Delta x_i, \Delta y_i, \Delta z_i$ for beam position i into account. RDRS can be used with full BT but might also be used with LBT or without BT at all. Thus, for D_m^{ik} calculations in RDRS the beam position i is only affected by (lateral) BT parameters if the respective method is applied during beam delivery.

For RDBT it is sufficient to calculate only dose contributions concerning later irradiated raster positions $k > i$. In RDRS, also dose changes to beam positions $k < i$ are accumulated as they are relevant for future re-scans. Consequently, the regarding dose compensation parameters are additionally calculated. It should be stated here that these additional parameters increase the NLUT size only if the initial implementation (see Section 2.2.1) is used. The size of the low memory NLUT introduced in Section 3.2.1 is not increased as its size does not depend on the number of beam positions in the treatment plan.

The possible lack of (lateral) BT in RDRS also implies that the Bragg peak position \vec{x}_{BP}^i might not coincide with the anatomical position \vec{x}_{ana}^i the Bragg peak is applied to in the reference state. Moreover, the Bragg peak might be closer to the anatomical position \vec{x}_{ana}^l of another beam position l . This is especially likely if RDRS is used without BT at all. In this case the corrected particle number N_{adapt}^l (see Equation 2.5 on page 56) of beam position l should be delivered (see Figure 4.1). Therefore, for the use without BT the NLUT is extended by a correlation table

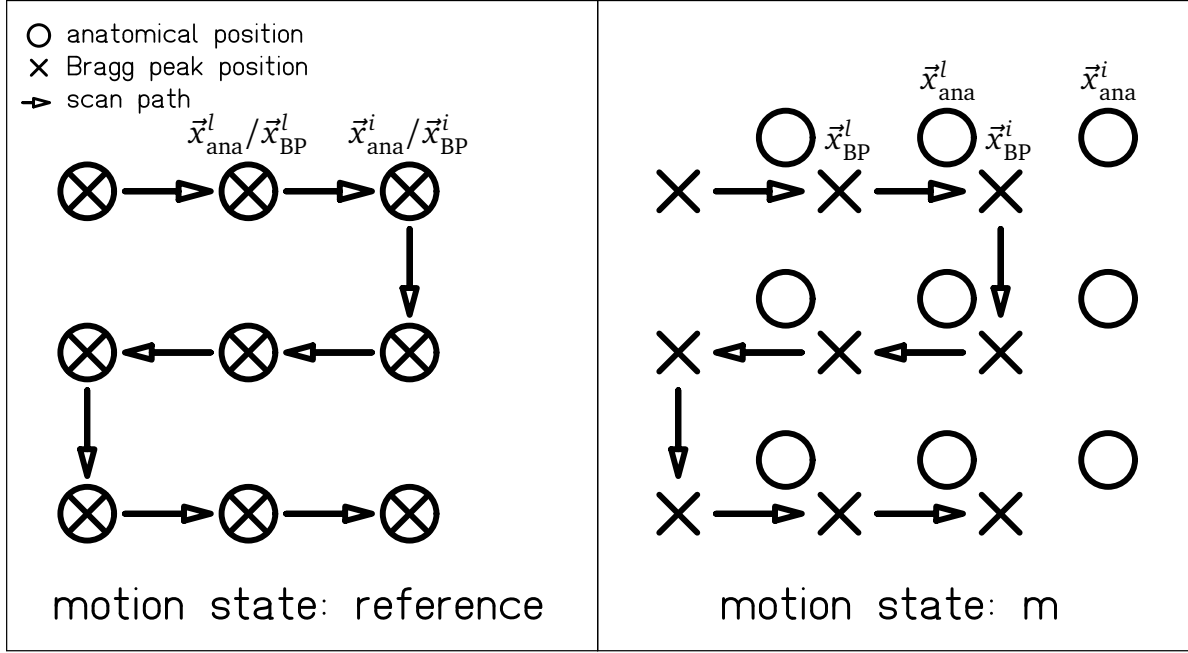


Figure 4.1.: Illustration of the necessity for the correlation table. Anatomical position \vec{x}_{ana}^i and according Bragg peak position \vec{x}_{BP}^i coincide for the reference motion state. Due to organ motion and the lack of BT in motion state m , the anatomical position \vec{x}_{ana}^l of beam position l is closer to the Bragg peak position \vec{x}_{BP}^i than the anatomical position \vec{x}_{ana}^i . Accordingly, if beam position i is to be irradiated in motion state m , the adapted particle number of beam position l , N_{adapt}^l , will be used for irradiation. For each beam position, the motion state dependent closest anatomical position is stored in the correlation table for all motion states.

from that the motion state dependent closest beam position can be obtained in real-time. This correlation table is currently implemented only in the TCS. Thus, for the presented experiments this correlation table has been used while the simulations have been performed without this correlation table.

In some cases the Bragg peak might be positioned outside the target volume due to the lack of full BT. In this case the minimal applicable particle number N_{min} is applied. Ideally beam positions can be skipped, but depending on the delivery system a certain minimal number of particles might have to be applied (see Section 2.2.1).

4.1.2 Measurements

Film measurements have been performed to verify the working principle of RDRS. RDRS measurements have been compared to *re-scanning* measurements. In these two dimensional film measurements the energy adaptation can not be assessed. RDRS combined with LBT is not an option since in two dimensions LBT results in complete motion compensation. Thus, for the film measurements RDRS has been applied without BT at all. RDRS has been used to account for dose changes from the current and from earlier re-scans and to lower the dose deposition to areas outside the target area. In comparison to *re-scanning*, there is no need to construct an internal target volume (ITV) despite the lack of BT. Also, in contrast to, e.g., *gating*, the full motion cycle is used for irradiation.

The target area (TA) has been a square of $6 \times 6 \text{ cm}^2$. Grid spacing was 2 mm in both directions with up-down-up scan path. Nominal particle number was 3×10^5 particles/beam position delivered in two target scans. 2 cm peak-to-peak motion in horizontal direction has been introduced by mounting the films on a motion table. Accordingly, a planning target area (PTA) has been constructed for *re-scanning* irradiations by adding internal margins (IM) encompassing the motion amplitude to the TA. The size of the *re-scanning* treatment plan thus was $8 \times 6 \text{ cm}^2$. No internal margins need to be applied for RDRS as the method compensates the lack of BT by the adaptation of particle numbers. The motion has been divided into 21 motion states and dose compensation parameters D_m^{ik} as well as a correlation table have been calculated. For *re-scanning* as well as RDRS 1, 3, 5, 7, 9, 11, and 15 re-scans have been measured. Target motion for all measurements was started in the same motion state for better comparability of the results.

Homogeneity as well as dose conformity of the films optical density (OD) have been assessed. To minimize the influence of setup uncertainties a 1 cm margin of the TA has been excluded from homogeneity analysis. The region of interest thus was $4 \times 4 \text{ cm}^2$. Homogeneity H has been calculated from the standard deviation $\text{OD}|_{\text{SD}}$ and mean value $\text{OD}|_{\text{mean}}$ of the OD distribution:

$$H = 1 - \frac{\text{OD}|_{\text{SD}}}{\text{OD}|_{\text{mean}}}. \quad (4.1)$$

The conformity of the distributions has been assessed by evaluating the integral OD in the TA ($6 \times 6 \text{ cm}^2$), OD_{TA} , and the integral OD of the complete irradiated area, OD_{all} . The conformity index (CI) is used for conformity assessment:

$$\text{CI} = \frac{\text{OD}_{\text{TA}}}{\text{OD}_{\text{all}}}. \quad (4.2)$$

The resulting mean CIs for RDRS and *re-scanning* from all measurements with different number of re-scans are tested by a two-sided t-test. Mean CIs and the p value are reported.

4.1.3 Simulations

Delivery of a treatment plan covering a three dimensional target volume with RDRS has been simulated using TRiP4D. RDRS has been used in conjunction with LBT. This combination, as described above, is considered to have the potential to supersede the energy compensation system needed for full BT as well as RDBT. Five re-scans have been used. In contrast to the TCS, the correlation table is not implemented in TRiP4D. Thus, particle number correction of the nominal beam position is applied.

For easier comparability with other motion mitigation techniques, simulations have been based on the time resolved computed tomography (4DCT) and setup used for the simulations in Section 2.2.3 that is shortly summarized:

- SPHERE treatment plan: spherical target volume with 22 mm radius,
- water phantom 4DCT with 25 motion states,
- target dose 1 Gy
- rotational motion between -14° and 10° ,
- 3.8 s motion period,
- ten different motion starting phases.

As all simulation input parameters were identical to those in the simulation of BT and RDBT conducted in Section 2.2.3, results can be directly compared. Dose cuts for one exemplary motion starting phase (0°) from static as well as BT, RDBT, and RDRS are presented. The dose volume histograms (DVHs) for all ten motion starting phases are compared for all investigated motion mitigation techniques with respect to over- and underdoses compared to the static irradiation.

4.2 Results

4.2.1 Measurements

The optical density distributions for all *re-scanning* and RDRS measurements as well as the static measurements are shown in Figure 4.2 on the next page and 4.3 on page 97. An increase in homogeneity for both methods can be seen. Also, the increasing mean OD of the RDRS measurements that is attributed to the compulsive delivery of a minimum number of particles can be seen.

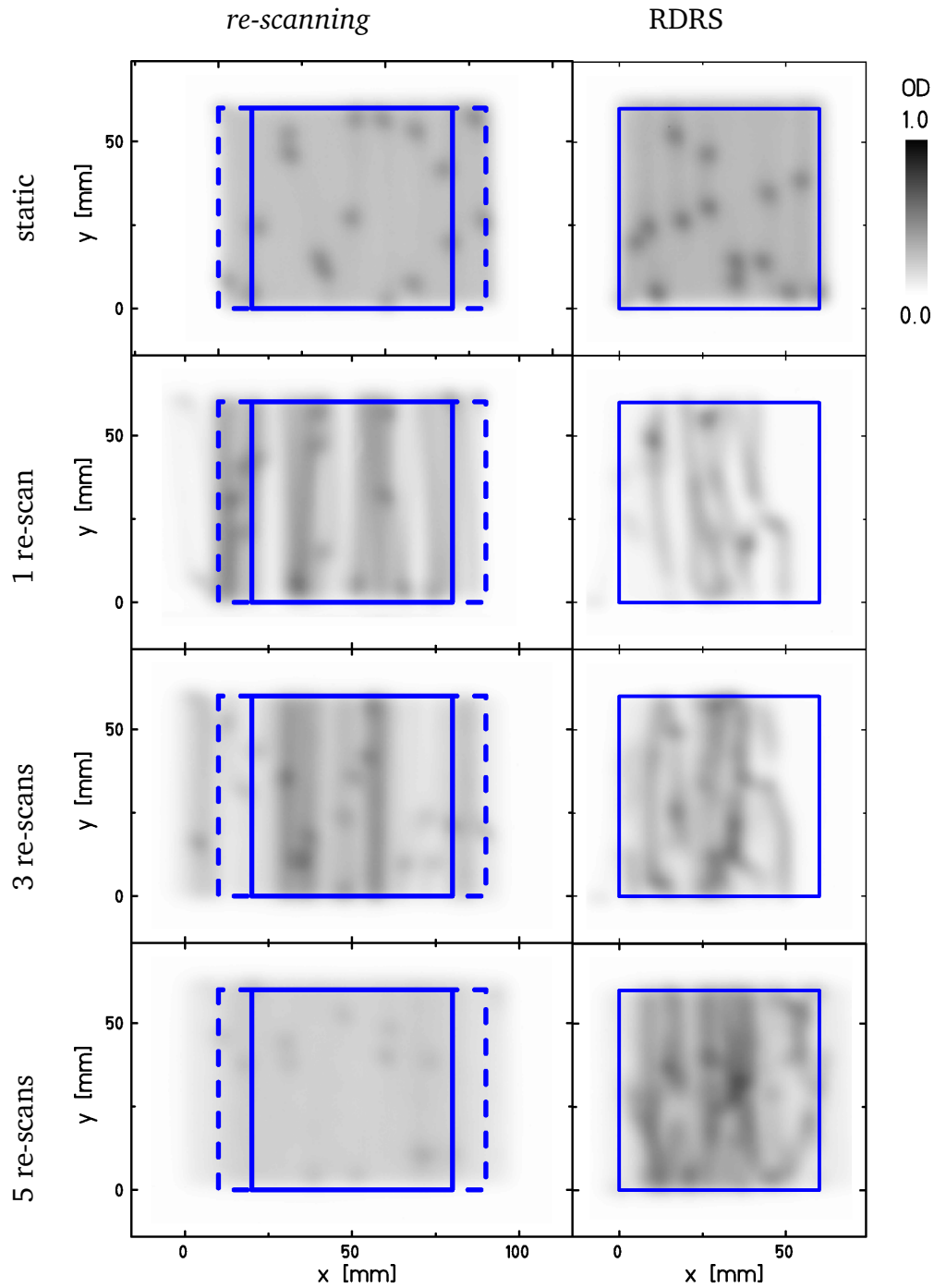


Figure 4.2.: Measured ODs represented by grayscale images. The target area is drawn in blue solid lines. Dashed lines indicate the internal margins that had to be added for *re-scanning*. In this figure, the static distributions as well as the distributions for 1, 3, and 5 re-scans are shown. The distributions for 7, 9, 11, and 15 re-scans can be found in Figure 4.3 on the facing page.

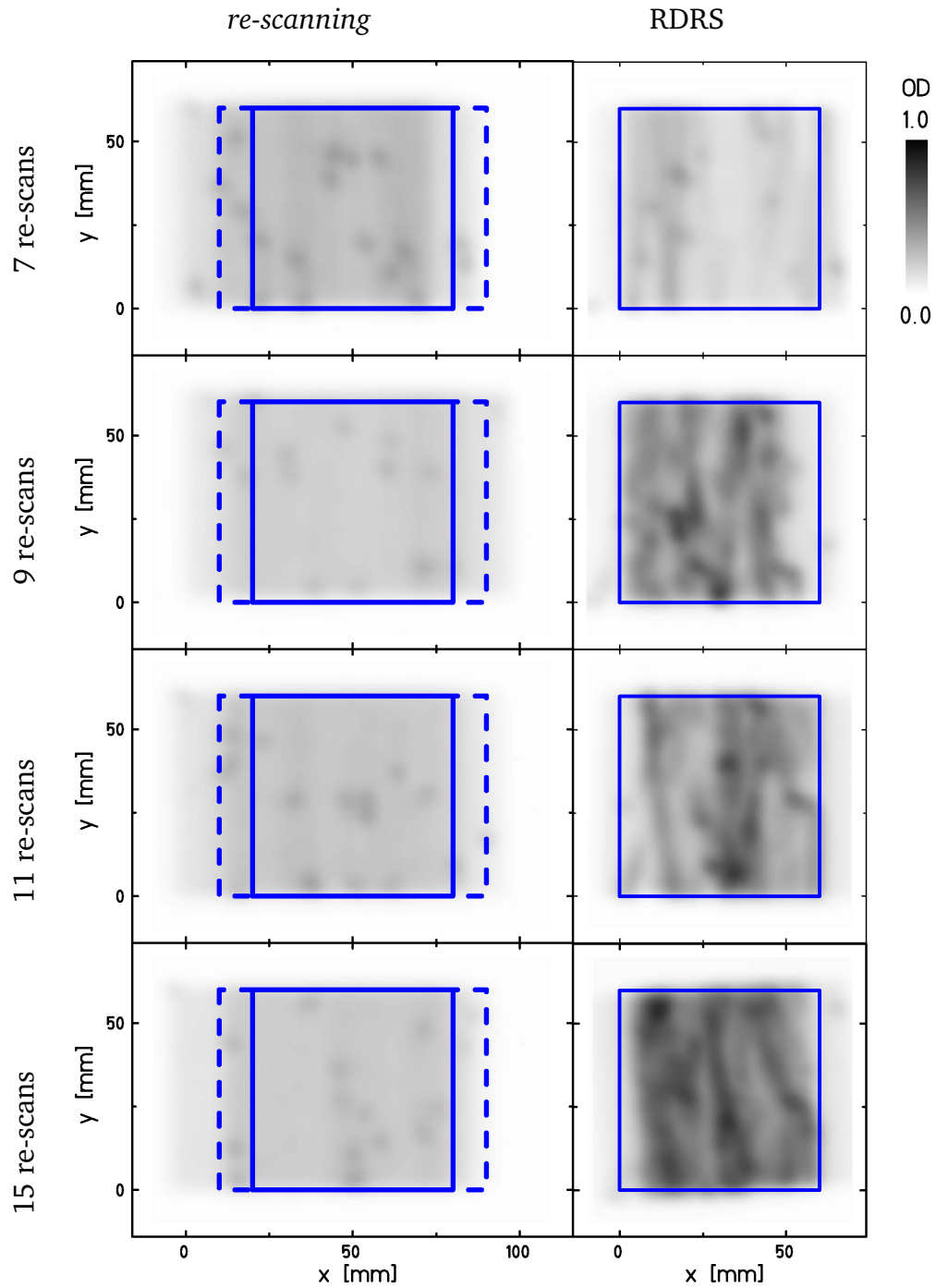


Figure 4.3.: Measured ODs represented by grayscale images. The target area is drawn in blue solid lines. Dashed lines indicate the internal margins that had to be added for *re-scanning*. In this figure, the distributions for 7, 9, 11, and 15 re-scans are shown. The static distributions as well as the distributions for 1, 3, and 5 re-scans can be found in Figure 4.2 on the facing page.

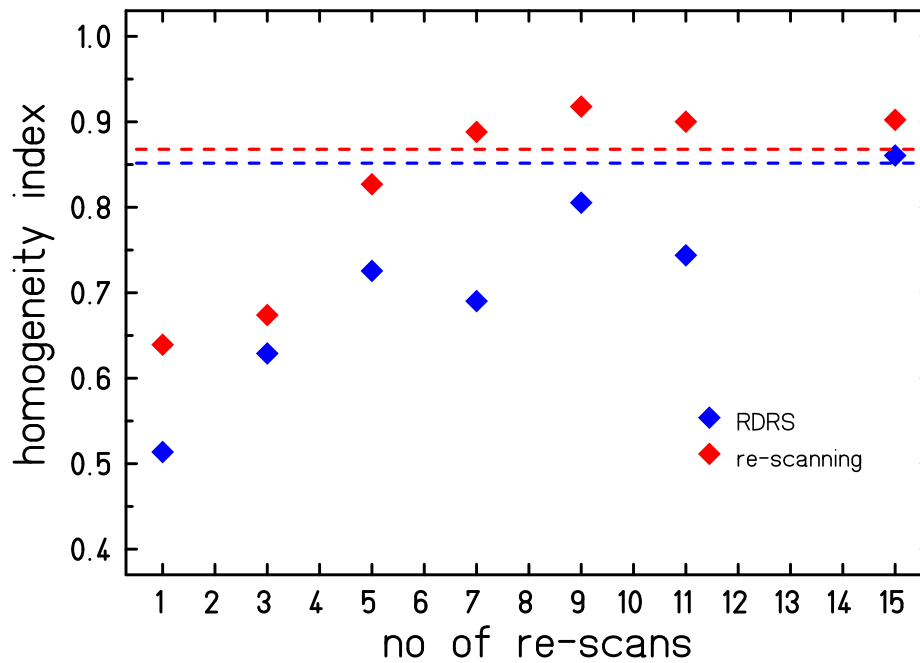


Figure 4.4.: Film homogeneity depending on the number of re-scans for RDRS as well as re-scanning. The homogeneity level of the static irradiation is given for both techniques as a dashed line.

Results of the homogeneity analysis are shown in Figure 4.4. Both methods show an increase of homogeneity with increasing number of re-scans. The homogeneity level of the respective static irradiation is achieved after seven re-scans for *re-scanning* and after 15 re-scans for RDRS. The homogeneity for *re-scanning* saturates at seven re-scans. As not more than 15 re-scans have been measured the saturation behavior for RDRS could not be investigated.

Conformity has been assessed by the CI. The result is presented in Table 4.1. The irradiations

Table 4.1.: Conformity of *re-scanning* and RDRS using the conformity index (CI). For both techniques the mean conformity from all seven measurements using different number of re-scans is given. The two-sided t-test has been used to assess the significance of the obtained mean conformity differences.

mean CI _{re-scanning} (SD)	mean CI _{RDRS} (SD)	p-value
59.7 (3.0)	90.6 (2.9)	1.1×10^{-7}

using RDRS have been significantly more conformal compared to the *re-scanning* irradiations. While on average only 59.7% of the integral OD have been measured within the TA in case of *re-scanning*, this number could be increased to 90.6% when RDRS has been used for dose delivery.

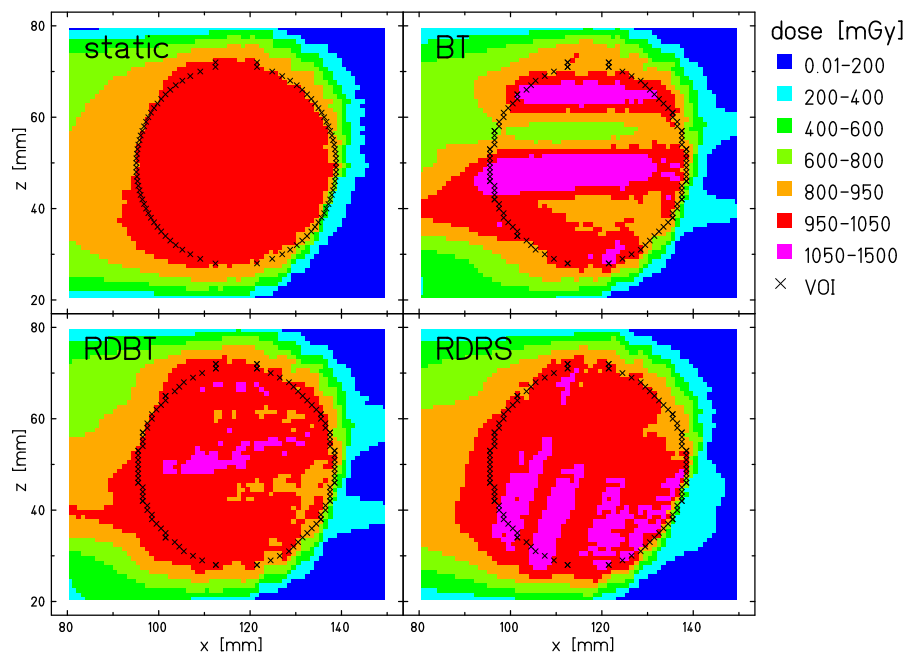


Figure 4.5.: Dose cuts through iso-centre. Static delivery as well as the motion mitigation techniques BT, RDBT, and RDRS are shown. For the motion mitigation techniques the cuts are from the simulation with motion starting phase at 0° .

4.2.2 Simulations

In Figure 4.5 dose cuts through the isocentre are shown. For BT, RDBT as well as RDRS the dose cuts with starting phase 0° are shown. Only BT shows in these cuts areas with doses below 800 mGy. RDRS shows less underdoses than BT. They are only apparent at the very distal part of the target volume. RDBT performs best in avoiding overdoses.

Figure 4.6 on the following page shows DVHs from simulations for different motion mitigation techniques. The SPHERE treatment plan introduced in Section 2.2.3 has been used. RDRS is preventing underdose for all starting phases very well. The prevention of underdoses for this setup is superior to BT and even RDBT. Overdoses are most effectively prevented using RDBT. But despite its lack of energy compensation, RDRS outperforms BT in preventing overdoses in the target volume.

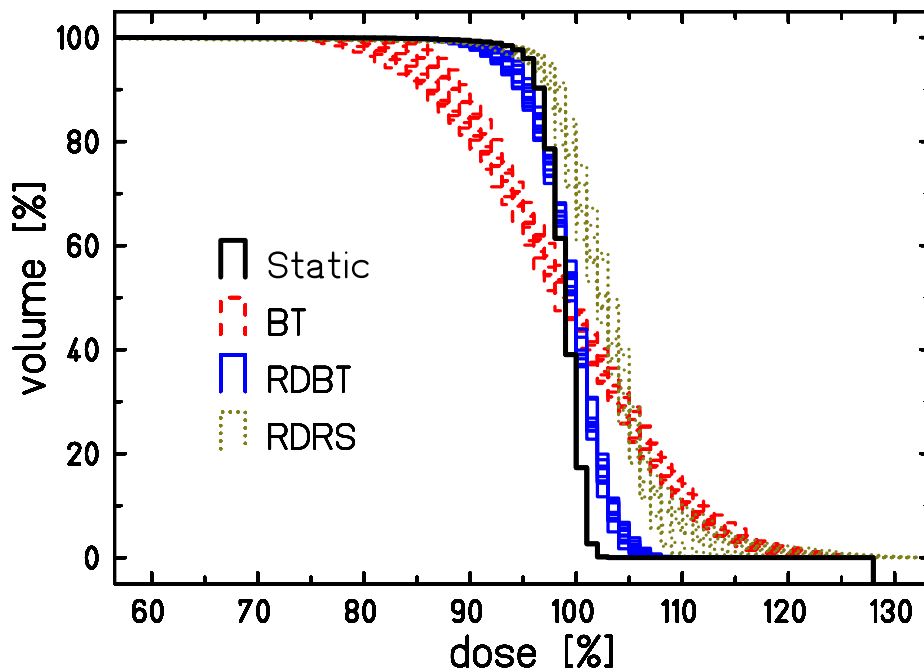


Figure 4.6.: DVHs for 10 different starting phases using RDRS. For comparison the earlier investigated techniques BT and RDBT are also shown (compare Section 2.3.2). RDRS in this setup exhibits the best prevention of underdoses for all techniques. Overdoses can be reduced compared to BT but are higher than in RDBT.

4.3 Discussion

Intrafractional tumor motion introduces a large variety of characteristics relevant for radiotherapy treatment of affected tumors. Tumor motion e.g., differs in amplitude, period, and reproducibility. As e.g., in the therapy of stationary tumors beam angles can be chosen for best organ at risk (OAR) sparing in the treatment of moving tumors the choice of a motion mitigation technique best suited to the actual tumor and its motion characteristic can improve e.g., target coverage, OAR sparing, and treatment time. The choice of a motion mitigation technique will not only be governed by the motion parameters. Additional hardware required by some of the most sophisticated motion mitigation techniques might not be available at all therapy centers. BT and RDBT require real-time energy adaptation systems. Currently no such system is clinically available. The motion mitigation technique RDRS introduced in this chapter does not rely on real-time energy adaptation. It's a pure software implementation and could thus in principle be implemented in any clinical center using scanned ion beam therapy. The only additional hardware requirement compared to irradiations of stationary tumors is a motion monitoring system. All introduced motion mitigation techniques but *re-scanning* explicitly rely on motion monitoring. Also for *re-scanning* a clinical implementation is very likely to include a motion monitoring system, e.g., for beam pausing in case of unexpected motion. Also more elaborate methods of

re-scanning have been proposed that rely on motion monitoring, e.g., to avoid synchronization between motion period and iso-energy slice (IES) irradiation time (Furukawa et al., 2007; Seco et al., 2009).

RDRS has been implemented into the GSI TCS as well as into TRiP treatment planning for Particles (TRiP). At the moment the correlation table is only implemented into the TCS. As in the simulations performed in TRiP RDRS has been used in conjunction with LBT the need for this correlation table is expected to be lower.

In film measurements RDRS has been compared to *re-scanning*. In the OD distributions dark spots can be seen already in the static irradiations. They are thus not caused by the motion mitigation techniques. Possible causes for these dark spots are the intensity control system of the TCS. These spots compromise the homogeneity values. Both techniques showed an increasing homogeneity with increasing number of re-scans. In case of *re-scanning* the homogeneity is even better than in the static case if the re-scan number is seven or larger. This can be explained when taking into account that also the influence of the dark spots is averaged with increasing re-scan number. The homogeneity of RDRS is biased by the need of delivering a minimal number of particles at each spot.

RDRS has proven to be very advantageous in terms of conformity. The CI could significantly be improved from 59.7% when *re-scanning* was used to 90.6% when RDRS was used. The conformity of a treatment technique in case of a clinical application is directly connected to healthy tissue sparing. An ITV needs to be constructed when *re-scanning* is used what intrinsically implies dose delivery to surrounding areas. The relative fraction of dose delivered to the target depends among other factors on the relation between target size and motion amplitude.

Besides affecting the films homogeneity the additional dose delivery also increased the mean dose with increasing number of re-scans for RDRS. This is because the current beam delivery system at GSI is not capable of skipping single beam positions. Thus, a minimal fraction of 10% had to be applied even if the current beam position already received enough dose or was even not within the TA. Thus, also the dose delivered to areas outside the TA is increased by this effect. Functionality to skip beam positions can in principle be implemented to the TCS. It is anticipated that this would further improve homogeneity, mean dose, and dose conformity of RDRS.

Simulations for a three dimensional treatment plan showed that the RDRS technique combined with LBT has the potential to improve dose coverage of the target volume compared to BT and at the same time reduce the hardware requirements for beam application compared to BT as no real-time energy compensation is needed.

The proposed RDRS technique would be especially advantageous for a tumor exhibiting a large target motion. Especially if no real-time energy adaptation is available and thus BT and RDBT can not be used, RDRS could be used. It could provide a higher tumor conformity com-

pared to *re-scanning* and at the same time use the full accelerator duty cycle in contrast to *gating*.

For the assessment of the efficacy of RDRS for clinical treatments, treatment planning studies are indispensable.

5 Discussion and perspectives

After the implementation of *real-time dose compensation* has been assessed in experiments and simulations, this chapter is intended to provide a summarizing discussion. Also, possible directions of future research will be outlined.

Modern radiotherapy methods like intensity modulated radiotherapy (IMRT) and scanned particle techniques allow one to shape the treatment field very conformally to the tumor. Dose to healthy tissue and, especially, organs at risk (OARs) can be kept very low. Both techniques use an overlay of many small beams, called beamlets in IMRT and pencil beams in scanned particle therapy. Thus, the treatment field for these intensity modulation techniques is not constant over the treatment time. When transferring these techniques to the therapy of intrafractionally moving tumors, interference effects occur if the treatment field changes on a time scale comparable to the time scale of tumor motion. These interference effects are known as *interplay*. To avoid or reduce the dose deteriorations introduced by these interferences two principle approaches in beam delivery are conceivable:

- beam application speed is changed to another time scale compared to tumor motion,
- motion mitigation techniques are applied to mitigate the perturbing effect of motion on the dose distribution.

In principle, the irradiation speed could be dramatically reduced. This would not only have the disadvantage of a prolonged treatment time but also smear out the dose distribution to an area encompassing the entire motion trajectory. Dose homogeneity would only be reached by abandoning tumor conformity. Hence, deceleration of the application speed is not an acceptable solution. A dramatic increase of the application speed, on the other hand, would lead to a quasi-static irradiation of the tumor, as intrafractional tumor motion within the irradiation time would become negligible. Up to now, no beam delivery system is able to deliver typical treatment doses precisely to a tumor volume on a time scale where organ motion is negligible. However, technical development towards accelerated dose delivery has been reported in the literature. Furukawa et al. report that a physical dose of 1 Gy could be delivered to a sphere with 60 mm radius within 20 s (Furukawa et al., 2010b). Pedroni et al. estimate a treatment time of 6.5 s for dose delivery to a volume of one liter comprising 21 iso-energy slices (IESs) in continuous scanning mode (Pedroni et al., 2004). Although these treatment times are much shorter than typical current treatment times, they are still on the same time scale as tumor motion. Thus, currently, the application of motion mitigation techniques is the only feasible option to treat intrafractionally moving tumors with intensity modulation techniques.

Various motion mitigation techniques have been proposed. Some of them are already in clinical use. *Re-scanning* relies on statistical averaging of different interplay patterns leading to a homogeneous overall dose by repeated delivery of treatment fields. This method is relatively robust against uncertainties if synchronization effects between target motion and beam delivery can be avoided. Methods to address the problem of synchronization have been proposed (Furukawa et al., 2007; Seco et al., 2009). *Re-scanning* compromises tumor conformity, as margins covering the whole motion trajectory need to be used. *Gating* restricts dose delivery to a subset of the tumor trajectory and, thus, achieves reduction of the target motion occurring during beam delivery. *Beam tracking* (BT) adapts the beam positions to the tumor motion and can, thus, in principle, maintain full tumor conformity.

Knowing the specific advantages and drawbacks of each motion mitigation technique, treatments of moving tumors could be tailored to individual patient characteristics. *Re-scanning* might be the method of choice if a tumor exhibits only small or hardly-reproducible motion because *re-scanning* is very robust and the severity of its main disadvantage, loss of tumor conformity, scales with the tumor motion amplitude. *Gating* is currently already used in IMRT treatments (Keall et al., 2006) as well as in passive particle beam delivery (Miyamoto et al., 2003). The tumor motion during beam application is reduced to the residual motion within the gating window. Accordingly, the severity of interplay patterns is reduced. It can be further reduced by combining *gating* with *re-scanning* (Furukawa et al., 2010a). BT techniques have so far only been applied clinically in photon therapy (Ozhasoglu et al., 2008). BT in photon therapy is realized by adapting the lateral beam position to the tumor motion. The application of BT in scanned particle therapy involves additional complexity as the range sensitivity of ion beams is much larger compared to photon beams. This sensitivity necessitates the implementation of a fast beam energy adaptation system for three dimensional adaptation of the Bragg peak position. Even if fast energy adaptation is available, dose distributions can be compromised if non-translational motion occurs. Non-translational motion can change the tumor geometry relative to the pathway of the beam even if three dimensional BT is applied. These dose deteriorations are not predictable due to the limited accuracy of a priori knowledge concerning patient motion. A *real-time dose compensation* functionality can be implemented to assess, based on measured motion, and compensate dose changes occurring during beam application by adapting the nominal particle numbers applied at each beam position. Such a method is considered to be a closed-loop method as the results of the ongoing dose delivery are fed back to the therapy control system (TCS) and are used to adapt the ongoing delivery process. Such an approach has been proposed by Bert (Bert, 2006) but has not been implemented into the TCS prior to this work. A closed-loop approach for real-time dose adaptation in photon therapy has been proposed by Lu et al. (Lu et al., 2009). Their implementation is based on the TomoTherapy system (see Section 1.3 on page 28) and adapts dose deposition based on accumulated dose delivery and estimation of future dose delivery.

Within the scope of this work, *real-time dose compensation combined with beam tracking* (RDBT) has been implemented into the GSI Helmholtzzentrum für Schwerionenforschung GmbH (GSI) TCS. Its functionality has been experimentally verified in water phantom measurements (see Chapter 2). Rotational motion was introduced (total rotation angle of -24°) by a dedicated motion table. Nominal dose was 1 Gy, and different simple geometric shapes were used as target volumes. Average under- and overdoses in BT for the different target volumes have been measured to be between 27 mGy and 68 mGy. These could be reduced to 12 mGy to 37 mGy by using RDBT. The efficacy of RDBT was thus experimentally verified. However, the experimental conditions are not easily transferrable to a clinical scenario. A relatively large rotation was used that covers a worst case scenario rather than a typical tumor motion. The heterogeneous density distribution of a patient, especially in the lung region, was also not adequately represented by the employed water phantom. While relative biological effectiveness (RBE) weighted dose needs to be used for radiotherapy, measurements could only assess absorbed dose. Therefore, treatment planning studies were conducted in Chapter 3.

Treatment planning studies, based on time resolved computed tomography (4DCT) data from five lung cancer patients, were conducted as a first step to answer the question which tumor characteristics require which level of BT complexity. Therefore, the techniques lateral *beam tracking* (LBT), BT and RDBT have been compared for scanned carbon therapy. For comparison, beam application without motion mitigation has additionally been simulated. The study was based on a fractionation scheme applied in passive carbon radiotherapy at the National Institute of Radiological Sciences (NIRS) (Miyamoto et al., 2007). Different measures were used to evaluate the dose distributions for all application techniques. Dose coverage of the clinical target volume (CTV) was assessed by V_{95} ¹, the overdose level was assessed by the V_{107} value and the $D_5 - D_{95}$ ² value has been used as a measure for dose homogeneity. BT and RDBT have typically delivered significantly superior dose distributions compared to LBT and beam application without motion mitigation. RDBT typically outperformed BT when the V_{107} and the $D_5 - D_{95}$ value were measured. The V_{95} values for both techniques were on average above 95% for all patients. These results are different from the results reported by Bert (Bert, 2006). Bert found unacceptably low V_{95} values for some patients when BT was applied. While the RDBT results reported by Bert typically offered excellent V_{95} the over-dose level was increased when using RDBT. The patients in the current study covered a tumor motion range from 1 mm to 25 mm. Patient 3 exhibiting a motion amplitude of only 1 mm showed good target coverage even when treated without motion mitigation. For such patients treatment without motion mitigation can be justified. At MD Anderson Cancer Center (MDACC) lung cancer patients with very low tumor motion have already been treated with scanned proton beams without application of one of the introduced motion mitigation techniques. Dose coverage in patients with larger motion

¹ V_{95} : The volume that receives at least 95% of the prescribed dose.

² D_5 : 5% of the volume received a dose of at least D_5 .

amplitude was not satisfying if interplay or LBT were used. Thus, at least for the applied fractionation scheme and field setup there are lung cancer patients whose motion characteristics suggest the necessity for energy compensation if BT methods are supposed to be used. In one case, patient 2, BT produced a high level of over-doses that was not measured when RDBT was used. These over-doses in BT might be connected to density gradients apparent within the CTV of this patient. Similar effects for heterogeneous phantoms have been reported by van de Water et al. (van de Water et al., 2009).

In Chapter 4, a new motion mitigation technique, called *real-time dose compensated re-scanning* (RDRS), is proposed. It combines *real-time dose compensation* with several re-scans. BT can be optionally used with this method. Also, the application of BT in less than three dimensions, e.g., LBT, can be used with this method. Besides increased robustness due to the effect of the re-scans, this method also compensates for dose changes introduced by missing or limited BT. Thus, this method might supersede the technically challenging implementation of real-time energy adaptation in a clinical environment. Film irradiations for twodimensional treatment plans as well as simulations using threedimensional treatment plans have been performed. For the film irradiations, the mean conformity to the target area (TA) could be increased from 59.7 when *re-scanning* was used to 90.6 when RDRS without BT was used. Homogeneity comparable to the static irradiation could be obtained with less re-scans by *re-scanning* than by RDRS. Simulations using a water phantom showed a substantial reduction of under-doses when RDRS combined with LBT was used compared to BT and even compared to RDBT. Over-dose level has been reduced in comparison to BT but was not as low as the over-dose level obtained applying RDBT. It should be emphasized that among these three methods only RDRS did not rely on real-time energy adaptation. Installation of a real-time energy adaptation system is expected to be one of the most critical steps in transferring BT into a clinical environment. However, only an initial assessment of RDRS could be presented in this work. Further measurements and simulations are needed to assess the clinical efficacy of RDRS. Especially, treatment planning studies like those conducted in this work comparing LBT, BT, and RDBT would be desirable.

In order to transfer any of the introduced motion mitigation techniques to a clinical environment several steps are needed. They encompass hardware and software upgrades as well as workflow changes. Some of the required steps are outlined here:

Motion monitoring: In a clinical environment, all motion mitigation techniques will require monitoring of the tumor motion. Several techniques are available. A review has been published by Evans et al. (Evans, 2008). A comparison of the correlation of different surrogate signals with tumor motion has been investigated by Steidl (Steidl, 2011).

4D treatment planning: In order to treat mobile tumors, dedicated 4D treatment planning is necessary. Methods have been proposed for photon (Keall, 2004; Keall et al., 2005) as well as for particle treatments (Rietzel et al., 2005a; Bert and Rietzel, 2007).

TCS: The TCS needs to be extended. For BT and related techniques, the ability for real-time adaptation of the Bragg peak position needs to be implemented. The interlock system needs to be upgraded, e.g., to cover irregular patient motion.

Quality assurance: Quality assurance for moving tumors is more complex than for stationary tumors. The application of motion phantoms might be considered (Serban et al., 2008; Steidl, 2011). A method for BT quality assurance has been proposed by Saito et al. (Saito et al., 2010).

The implementations to the TCS and to TRreatment planning for Particles (TRiP) presented in this work show a possible way towards clinical 4D treatment planning and 4D treatment delivery. The treatment planning studies are important to assess the necessity of motion mitigation for different motion characteristics. They should, in the future, be extended by robustness analysis.

However, 4D treatment planning, especially for scanned particle beams, is a relatively new field and many developments can be expected in the future. So far, 4D treatment planning typically encompasses the optimization of a 3D treatment plan. In case of BT as well as RDBT, compensation parameters aiming to preserve the 3D optimized dose distribution are precalculated. That means that the motion and the anatomic information of the other 4DCT states is not exploited in the optimization process. This has already been stated by Bert et al. (Bert and Durante, 2011). In photon therapy, methods incorporating the full 4DCT information into the optimization process have been proposed, e.g., by Nohadani et al. (Nohadani et al., 2010). A real 4D optimization might also improve scanned particle delivery for moving tumors. One method for 4D optimization and beam delivery is proposed here. It is called motion synchronized delivery (MSD). For photon therapy dose-rate regulated tracking (DRRT) has been proposed (Yi et al., 2008). The basic ideas of both approaches are comparable.

One of the major problems in treatment plan optimization for moving targets is the missing a priori knowledge concerning the patient's motion trajectory. Even in the case where the 4DCT information is still valid at time of treatment delivery the exact breathing trajectory, i.e., the exact time sequence of the motion states is in general not known. Thus, the correlation between a beam position and the motion state it will be irradiated in is unknown.

For MSD, a treatment plan is optimized taking a nominal patient motion trajectory, e.g., obtained during the imaging session, into account. At the time of treatment delivery, the assumed correlation between beam positions and motion states is likely not to be valid any more. Instead of trying to adapt the patient motion to the treatment plan, in MSD, the beam delivery is adapted to the patient motion. This can be achieved by incorporating multiple beam pauses into the nominal 4D treatment plan. At the end of each nominal motion state a beam pause is scheduled. Thus in each motion state m_i a fraction t_i^p of the nominal length t_i is reserved for a beam pause while the remaining time $t_i^b = t_i - t_i^p$ is used for irradiation of N_i beam positions.

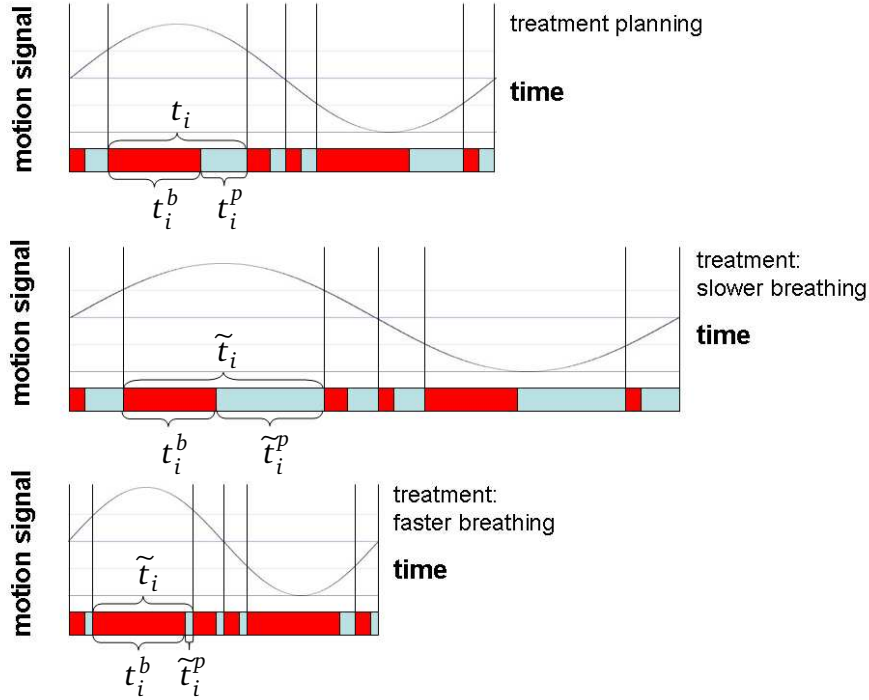


Figure 5.1.: Sketch of the working principle of motion synchronized delivery. Beam-on time (t_i^b , red) as well as one nominal pause (t_i^p , light blue) per motion state are scheduled in treatment planning. At time of treatment delivery the pause duration \tilde{t}_i^p is prolonged in case of slower breathing or shortened in case of faster breathing. In both cases the beam-on time t_i^b can be kept constant and thus delivery of the nominal amount of beam positions in that motion state can be achieved and the nominal correlation between beam positions and motion state can thus be maintained. Although not explicitly shown here, frequency changes within one treatment session can also be handled.

During beam delivery, the length of this beam pause is adapted to the patient motion. It is likely that the time \tilde{t}_i spent in the motion state m_i during therapy differs from t_i assumed in treatment planning. In case $\tilde{t}_i > t_i$ the beam pause is prolonged $\tilde{t}_i^p > t_i^p$. Vice versa the beam pause is shortened $\tilde{t}_i^p < t_i^p$ if the patient spends less time in the motion state m_i , i.e., $\tilde{t}_i < t_i$. In both cases, $\tilde{t}_i = t_i^b + \tilde{t}_i^p$ is valid, and the nominal number of beam positions N_i can be irradiated in the motion state m_i . Thus, the correlation between motion state and beam positions can be preserved. DRRT also relies on real-time adaptation of the beam delivery to maintain correlations. Instead of introducing beam pauses, the dose rate is adapted.

A sketch of the working principle of MSD is shown in Figure 5.1. Although not shown in that figure, changes of the breathing speed during therapy can also be handled as the length of each pause is adapted separately. Some issues need to be solved before such a method could be applied. While frequency changes within certain limits can easily be dealt with, amplitude changes are more difficult to handle. Optimization including all motion states is not yet implemented for scanned particle therapy but seems achievable for the proposed method, since the basic routines

for 3D optimization can be applied due to the preserved correlation between motion state and beam positions.



6 Conclusions

Scanned particle therapy provides very conformal irradiations of stationary tumors. With this technique, the tumor is covered with thousands or even ten thousands of beam positions. An optimized amount of particles is delivered to each of these beam positions employing a narrow pencil beam. By using heavier ions, an elevated biological effectiveness can be exploited in addition to physical advantages of ions compared to photons. An increasing number of clinical centers use scanned particle radiotherapy. Irradiations have so far been restricted to tumor locations not exhibiting considerable intrafractional motion, as interference effects between dynamic beam application and tumor motion deteriorate resulting dose distributions.

Several motion mitigation techniques to overcome these dose deteriorations are currently investigated. *Beam tracking* (BT) is one of these methods. The idea of BT is to adapt the pencil beam positions to the changing tumor position. A dose distribution optimized for a static tumor can, in principle, be preserved if target motion is purely translational. In the case of nontranslational motion, e.g., rotations and deformations, the tumor geometry with respect to the pencil beam's path is altered. This leads to changes in the overall dose distribution, even if each pencil beam position is adapted to the changed target position.

Real-time dose compensation combined with beam tracking (RDBT) was proposed to mitigate these dose changes in real-time during dose delivery. In this work such a functionality has been implemented into the therapy control system (TCS) at GSI Helmholtzzentrum für Schwerionenforschung GmbH (GSI) as well as into the GSI treatment planning software TRreatment planning for Particles (TRiP). The implemented functionality has been verified in dedicated experiments. A significant reduction of dose changes compared to a static reference irradiation has been measured when RDBT was used for motion mitigation compared to BT. Dose distributions were reconstructed using a 4D extension of TRiP. Reconstructed dose differences were in good agreement with those experimentally obtained.

The clinical benefit of RDBT has been assessed in treatment planning studies. Scanned carbon ion therapy courses, comprising four fractions with four treatment fields each, have been simulated based on time resolved computed tomography (4DCT) data of five lung cancer patients. A range of different tumor motion parameters has been used. For most patients, overdose (3 out of 5 patients) was significantly reduced and dose homogeneity (4 out of 5 patients) was significantly improved when RDBT was used compared to all other techniques. BT and RDBT were superior to lateral *beam tracking* (LBT) and beam application without motion mitigation. Differences between the investigated motion mitigation techniques were small for one patient exhibiting only a very small tumor motion.

A method combining *real-time dose compensation* with several re-scans, called *real-time dose compensated re-scanning* (RDRS), has been proposed. In conjunction with LBT this method should have the potential to supersede the technically complex real-time energy adaptation needed for BT. Film experiments comparing RDRS and *re-scanning*, i.e., a motion mitigation technique using repeated dose delivery to average under- and overdoses, as well as simulations comparing RDRS, RDBT and BT have been performed. The RDRS film measurements showed a significantly improved sparing of areas surrounding the target area compared to *re-scanning*. In simulations, RDRS showed a better prevention of underdoses when compared to BT and RDBT. The level of overdose was reduced using RDRS compared to BT but not as low as achieved by RDBT. Further assessment of this technique, preferably using patient data, will be needed to explore the clinical efficacy of RDRS.

A Results treatment planning studies

Results of the treatment planning studies that were not presented in the text are shown here.

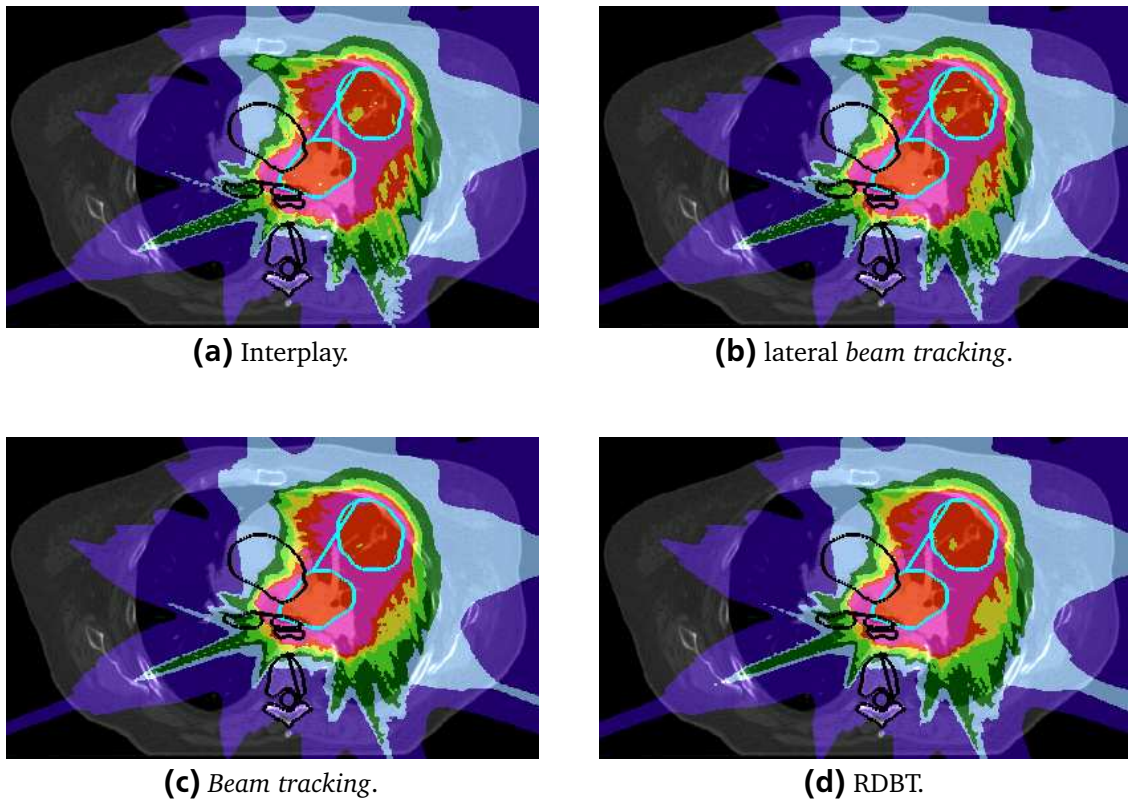
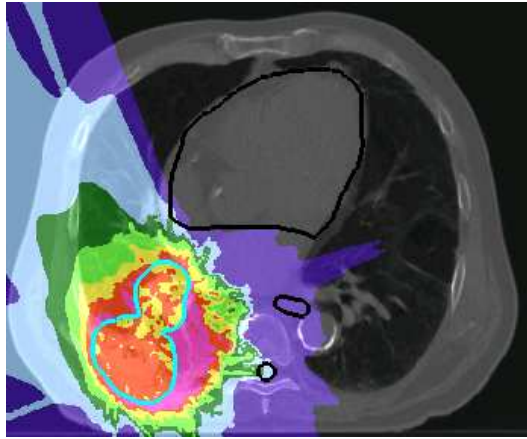
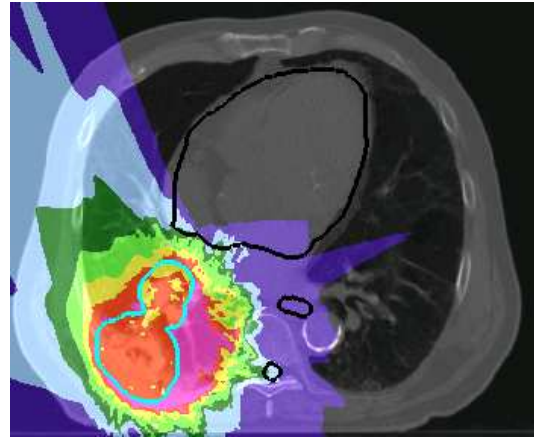


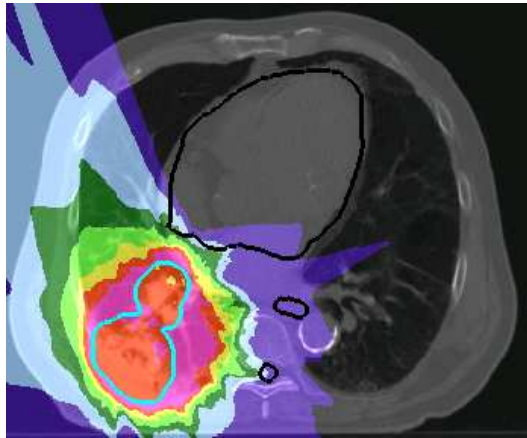
Figure A.1.: Dose distributions for all four application techniques in patient 1. Cuts are drawn through iso-centre. The line connecting the CTVs is a display artifact. Motion period of 4 s and motion starting phases of 0° , 90° , 180° , and 270° have been used. Dose calculation has been based on rigid registration. BT and RDBT deliver a more homogeneous dose distribution than interplay and LBT.



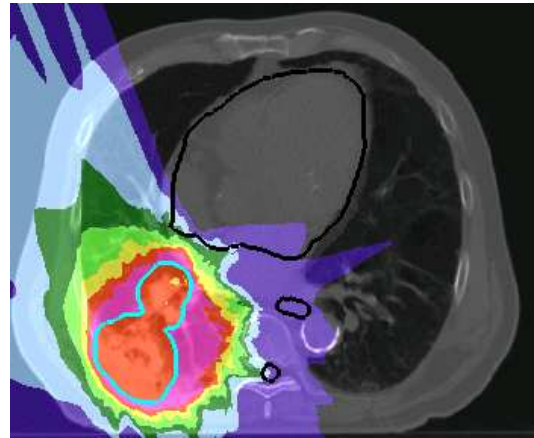
(a) Interplay.



(b) lateral beam tracking.

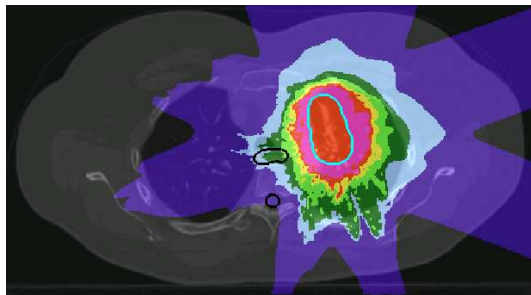


(c) Beam tracking.

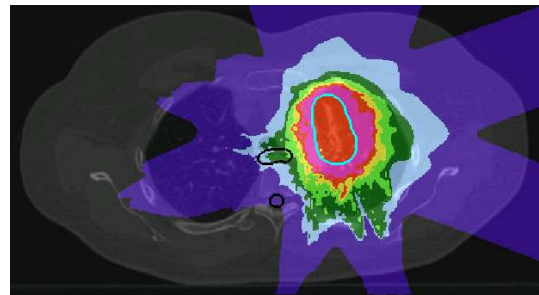


(d) RDBT.

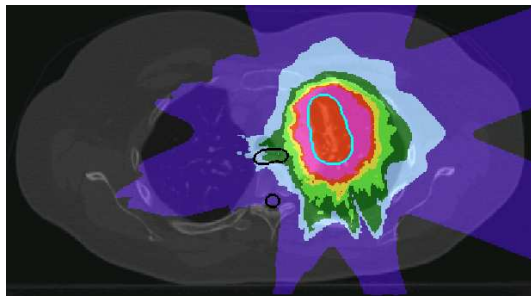
Figure A.2.: Dose distributions for all four application techniques in patient 2. Cuts are drawn through iso-centre. Motion period of 4s and motion starting phases of 0° , 90° , 180° , and 270° have been used. Dose calculation has been based on rigid registration. BT and RDBT deliver a more homogeneous dose distribution than interplay and LBT.



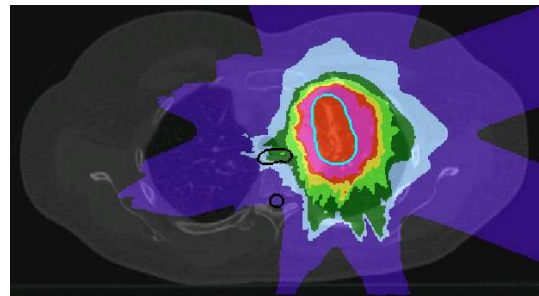
(a) Interplay.



(b) lateral beam tracking.

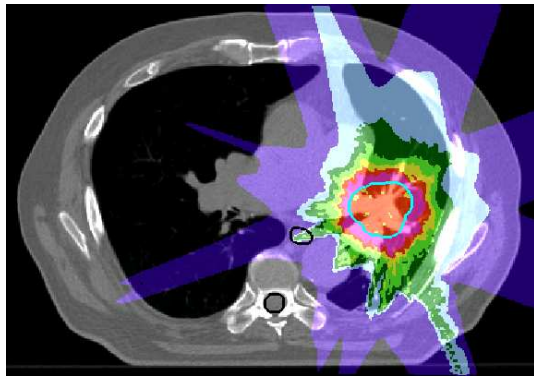


(c) Beam tracking.

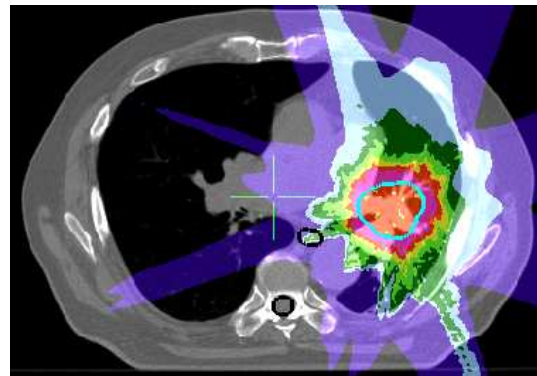


(d) RDBT.

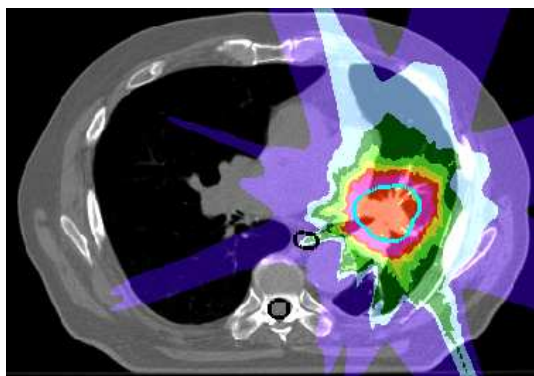
Figure A.3.: Dose distributions for all four application techniques in patient 3. Cuts are drawn through iso-centre. Motion period of 4 s and motion starting phases of 0° , 90° , 180° , and 270° have been used. Dose calculation has been based on rigid registration. Tumor motion for patient 3 was very small. Differences in dose distributions can hardly be seen.



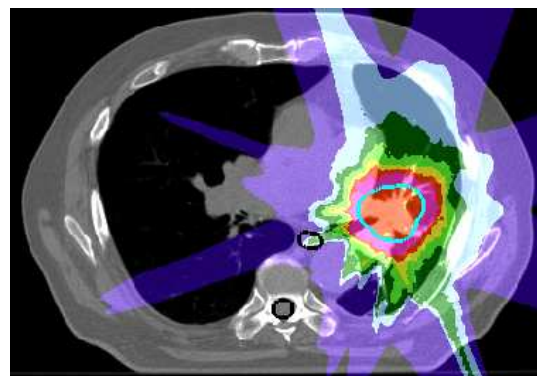
(a) Interplay.



(b) lateral beam tracking.



(c) Beam tracking.



(d) RDBT.

Figure A.4.: Dose distributions for all four application techniques in patient 4. Cuts are drawn through iso-centre. Motion period of 4s and motion starting phases of 0° , 90° , 180° , and 270° have been used. Dose calculation has been based on rigid registration. BT and RDBT deliver a more homogeneous dose distribution than interplay and LBT.

Table A.1.: Mean and standard deviations of V_{95} for all patients when rigid registration is used for dose calculation. Results of the fraction doses are shown here.

patient no	V_{95} mean (standard deviation) [% CTV volume]			
	interplay	lateral BT	BT	RDBT
1	90.9 (2.1)	92.0 (1.7)	98.8 (0.3)	97.8 (0.3)
2	66.1 (7.1)	80.5 (2.3)	98.0 (0.4)	97.9 (0.5)
3	97.5 (0.8)	97.3 (0.8)	99.7 (0.0)	99.2 (0.2)
4	82.3 (3.4)	81.7 (2.4)	92.9 (1.1)	94.6 (1.0)
5	49.4 (12.5)	86.6 (3.6)	99.5 (0.2)	98.8 (0.3)

Table A.2.: Overview of the significance of V_{95} differences between the application techniques using rigid registration. Results are for the treatment of one fraction. The V_{95} results of two techniques showed significant differences for the patients whose numbers is given in the corresponding cell while a "-" indicates no significant differences for that patient.

	interplay	LBT	BT	RDBT
interplay	-	-/2/-/-/5	1/2/3/4/5	1/2/3/4/5
LBT	-/2/-/-/5	-	1/2/3/4/5	1/2/3/4/5
BT	1/2/3/4/5	1/2/3/4/5	-	-/-/-/-/-
RDBT	1/2/3/4/5	1/2/3/4/5	-/-/-/-/-	-

Table A.3.: Mean and standard deviations of V_{95} for all patients when rigid registration is used for dose calculation. Results for the complete treatment course are shown.

patient no	V_{95} mean (standard deviation) [% CTV volume]			
	interplay	lateral BT	BT	RDBT
1	97.2 (0.7)	97.4 (0.7)	99.5 (0.1)	98.7 (0.1)
2	71.5 (3.6)	85.8 (1.4)	98.8 (0.2)	98.7 (0.3)
3	99.4 (0.1)	99.3 (0.2)	99.8 (0.0)	99.3 (0.1)
4	89.8 (1.1)	89.9 (1.2)	95.0 (0.9)	96.3 (0.6)
5	53.2 (9.3)	92.7 (1.2)	99.8 (0.1)	98.9 (0.2)

Table A.4.: Overview of the significance of V_{95} differences between the application techniques using rigid registration. Results for the complete treatment course are shown. The Tuckey-Kramer test at 5% significance level has been used. The V_{95} results of two techniques showed significant differences for the patients whose numbers is given in the corresponding cell while a "-" indicates no significant differences for that patient.

	interplay	LBT	BT	RDBT
interplay	-	1/2/-/-/5	1/2/3/4/5	1/2/3/4/5
LBT	1/2/-/-/5	-	1/2/3/4/5	1/2/3/4/5
BT	1/2/3/4/5	1/2/3/4/5	-	1/-/3/4/-
RDBT	1/2/3/4/5	1/2/3/4/5	1/-/3/4/-	-

Table A.5.: Mean and standard deviations of V_{95} for all patients when non-rigid registration is used for dose calculation while MLUT calculation is done using the rigid registration. Results are for the treatment of one fraction.

patient no	V_{95} mean (standard deviation) [% CTV volume]			
	interplay	lateral BT	BT	RDBT
1	91.3 (2.2)	91.9 (2.1)	97.6 (0.9)	95.8 (1.2)
2	71.0 (5.0)	77.1 (2.0)	90.5 (1.5)	86.8 (1.6)
3	95.1 (0.8)	94.7 (0.9)	98.7 (0.3)	97.1 (0.6)
4	82.7 (2.7)	81.2 (1.9)	91.8 (1.1)	93.0 (0.8)
5	54.5 (12.3)	83.2 (3.8)	94.1 (3.0)	90.6 (3.8)

Table A.6.: Overview of the significance of V_{95} differences between the application techniques using non-rigid registration for dose calculation. MLUT calculation has been performed based on rigid registration. Results are for the treatment of one fraction. The Tuckey-Kramer test at 5% significance level has been used. The V_{95} results of two techniques showed significant differences for the patients whose numbers is given in the corresponding cell while a "-" indicates no significant differences for that patient.

	interplay	LBT	BT	RDBT
interplay	-	-/2/-/-/5	1/2/3/4/5	1/2/3/4/5
LBT	-/2/-/-/5	-	1/2/3/4/5	1/2/3/4/-
BT	1/2/3/4/5	1/2/3/4/5	-	-/2/3/-/-
RDBT	1/2/3/4/5	1/2/3/4/-	-/2/3/-/-	-

Table A.7.: Mean and standard deviations of V_{95} for all patients when non-rigid registration is used for dose calculation while MLUT calculation is done using the rigid registration. Results for the complete treatment course are shown here.

patient no	V_{95} mean (standard deviation) [% CTV volume]			
	interplay	lateral BT	BT	RDBT
1	96.7 (0.7)	97.2 (0.7)	99.1 (0.2)	97.8 (0.3)
2	75.1 (2.7)	82.3 (1.1)	92.3 (0.6)	90.5 (1.1)
3	98.6 (0.3)	98.4 (0.4)	99.5 (0.1)	98.3 (0.3)
4	90.4 (1.3)	89.1 (1.4)	93.5 (0.8)	94.4 (0.7)
5	58.6 (8.7)	87.7 (1.7)	95.8 (0.8)	93.6 (1.2)

Table A.8.: Overview of the significance of V_{95} differences between the application techniques using non-rigid registration for dose calculation. MLUT calculation has been performed based on rigid registration. Results for the complete treatment course are shown here. The Tuckey-Kramer test at 5% significance level has been used. The V_{95} results of two techniques showed significant differences for the patients whose numbers is given in the corresponding cell while a "-" indicates no significant differences for that patient.

	interplay	LBT	BT	RDBT
interplay	-	1/2/3/4/5	1/2/3/4/5	1/2/3/4/5
LBT	1/2/3/4/5	-	1/2/3/4/5	1/2/3/4/5
BT	1/2/3/4/5	1/2/3/4/5	-	1/2/3/4/5
RDBT	1/2/3/4/5	1/2/3/4/5	1/2/3/4/5	-

Table A.9.: Mean and standard deviations of V_{107} for all patients when rigid registration is used for dose calculation. Results are for the treatment of one fraction.

patient no	V_{107} mean (standard deviation) [% CTV volume]			
	interplay	lateral BT	BT	RDBT
1	2.0 (0.8)	2.3 (0.7)	0.6 (0.2)	0.1 (0.0)
2	6.0 (3.0)	3.9 (0.8)	15.8 (1.0)	1.3 (0.3)
3	0.2 (0.1)	0.2 (0.1)	0.0 (0.0)	0.0 (0.0)
4	4.1 (1.8)	3.1 (1.3)	0.4 (0.2)	0.3 (0.2)
5	7.9 (13.0)	7.5 (2.9)	2.0 (0.6)	0.4 (0.4)

Table A.10.: Overview of the significance of V_{107} differences between the application techniques using rigid registration. Results are for the treatment of one fraction. The Tuckey-Kramer test at 5% significance level has been used. The V_{107} results of two techniques showed significant differences for the patients whose numbers is given in the corresponding cell while a "-" indicates no significant differences for that patient.

	interplay	LBT	BT	RDBT
interplay	-	-/2/-/-/-	1/2/3/4/-	1/2/3/4/5
LBT	-/2/-/-/-	-	1/2/3/4/-	1/2/3/4/-
BT	1/2/3/4/-	1/2/3/4/-	-	-/2/-/-/-
RDBT	1/2/3/4/5	1/2/3/4/-	-/2/-/-/-	-

Table A.11.: Mean and standard deviations of V_{107} for all patients when rigid registration is used for dose calculation. Results for the complete treatment course are shown.

patient no	V_{107} mean (standard deviation) [% CTV volume]			
	interplay	lateral BT	BT	RDBT
1	0.1 (0.1)	0.3 (0.1)	0.5 (0.1)	0.0 (0.0)
2	0.7 (0.6)	0.4 (0.2)	23.5 (0.5)	1.2 (0.3)
3	0.0 (0.0)	0.0 (0.0)	0.0 (0.0)	0.0 (0.0)
4	0.3 (0.2)	0.2 (0.2)	0.0 (0.0)	0.0 (0.0)
5	3.2 (5.7)	2.6 (1.1)	1.9 (0.6)	0.2 (0.2)

Table A.12.: Overview of the significance of V_{107} differences between the application techniques using rigid registration. Results for the complete treatment course are shown. The Tuckey-Kramer test at 5% significance level has been used. The V_{107} results of two techniques showed significant differences for the patients whose numbers is given in the corresponding cell while a "-" indicates no significant differences for that patient.

	interplay	LBT	BT	RDBT
interplay	-	1/2/-/4/-	1/2/3/4/5	1/2/3/4/5
LBT	1/2/-/4/-	-	1/2/-/4/-	1/2/-/4/5
BT	1/2/3/4/5	1/2/-/4/-	-	1/2/-/-/5
RDBT	1/2/3/4/5	1/2/-/4/5	1/2/-/-/5	-

Table A.13.: Mean and standard deviations of V_{107} for all patients when non-rigid registration is used for dose calculation. The MLUTs are calculated based on rigid registration. Results are for the treatment of one fraction.

patient no	V_{107} mean (standard deviation) [% CTV volume]			
	interplay	lateral BT	BT	RDBT
1	1.7 (0.9)	2.1 (0.7)	0.9 (0.3)	0.4 (0.6)
2	4.7 (2.3)	4.4 (1.1)	11.6 (2.4)	3.7 (1.0)
3	0.8 (0.3)	0.7 (0.3)	0.4 (0.2)	0.1 (0.1)
4	3.9 (1.7)	3.1 (1.3)	0.3 (0.2)	0.3 (0.2)
5	7.3 (11.7)	7.2 (2.7)	4.2 (2.2)	2.0 (1.4)

Table A.14.: Overview of the significance of V_{107} differences between the application techniques using non-rigid registration for dose calculation. MLUTs are calculated according to rigid registration. Results are for the treatment of one fraction. The Tuckey-Kramer test at 5% significance level has been used. The V_{107} results of two techniques showed significant differences for the patients whose numbers is given in the corresponding cell while a "-" indicates no significant differences for that patient.

	interplay	LBT	BT	RDBT
interplay	-	-/-/-/-/-	1/2/3/4/-	1/-/3/4/-
LBT	-/-/-/-/-	-	1/2/3/4/-	1/-/3/4/-
BT	1/2/3/4/-	1/2/3/4/-	-	-/2/3/-/-
RDBT	1/-/3/4/-	1/-/3/4/-	-/2/3/-/-	-

Table A.15.: Mean and standard deviations of V_{107} for all patients when non-rigid registration is used for dose calculation. The MLUTs are calculated based on rigid registration. Results for the complete treatment course are shown here.

patient no	V_{107} mean (standard deviation) [% CTV volume]			
	interplay	lateral BT	BT	RDBT
1	0.1 (0.1)	0.3 (0.2)	0.7 (0.2)	0.0 (0.1)
2	0.5 (0.4)	0.4 (0.2)	14.3 (1.1)	2.2 (0.7)
3	0.0 (0.0)	0.0 (0.0)	0.0 (0.0)	0.0 (0.0)
4	0.3 (0.2)	0.2 (0.2)	0.0 (0.0)	0.0 (0.0)
5	2.5 (4.6)	2.3 (0.9)	2.2 (1.0)	0.5 (0.4)

Table A.16.: Overview of the significance of V_{107} differences between the application techniques using non-rigid registration for dose calculation. MLUTs are calculated according to rigid registration. Results for the complete treatment course are shown here. The Tuckey-Kramer test at 5% significance level has been used. The V_{107} results of two techniques showed significant differences for the patients whose numbers is given in the corresponding cell while a "-" indicates no significant differences for that patient.

	interplay	LBT	BT	RDBT
interplay	-	1/-/-/4/-	1/2/3/4/-	-/2/3/4/5
LBT	1/-/-/4/-	-	1/2/3/4/-	1/2/3/4/5
BT	1/2/3/4/-	1/2/3/4/-	-	1/2/3/-/5
RDBT	-/2/3/4/5	1/2/3/4/5	1/2/3/-/5	-

Table A.17.: Mean and standard deviations of $D_5 - D_{95}$ for all patients when rigid registration is used for dose calculation. Results are for the treatment of one fraction.

patient no	$D_5 - D_{95}$ mean (standard deviation) [% prescribed dose]			
	interplay	lateral BT	BT	RDBT
1	11.4 (0.7)	11.6 (0.9)	7.8 (0.5)	6.8 (0.6)
2	26.9 (3.6)	15.6 (0.9)	13.6 (0.5)	8.7 (0.5)
3	7.3 (0.9)	7.2 (1.0)	5.8 (0.4)	5.2 (0.4)
4	15.2 (1.1)	14.5 (1.2)	9.1 (0.3)	8.4 (0.8)
5	40.8 (10.4)	15.8 (2.2)	7.7 (0.8)	7.2 (0.6)

Table A.18.: Overview of the significance of $D_5 - D_{95}$ differences between the application techniques using rigid registration. Results are for the treatment of one fraction. The Tuckey-Kramer test at 5% significance level has been used. The $D_5 - D_{95}$ results of two techniques showed significant differences for the patients whose numbers is given in the corresponding cell while a "-" indicates no significant differences for that patient.

	interplay	LBT	BT	RDBT
interplay	-	-/2/-/-/5	1/2/3/4/5	1/2/3/4/5
LBT	-/2/-/-/5	-	1/-/3/4/5	1/2/3/4/5
BT	1/2/3/4/5	1/-/3/4/5	-	1/2/-/-/-
RDBT	1/2/3/4/5	1/2/3/4/5	1/2/-/-/-	-

Table A.19.: Mean and standard deviations of $D_5 - D_{95}$ for all patients when rigid registration is used for dose calculation. Results for the complete treatment course are shown.

patient no	$D_5 - D_{95}$ mean (standard deviation) [% prescribed dose]			
	interplay	lateral BT	BT	RDBT
1	7.1 (0.8)	7.9 (0.7)	6.0 (0.2)	5.1 (0.3)
2	26.1 (2.1)	11.9 (0.8)	15.9 (0.5)	8.8 (0.4)
3	4.5 (0.7)	4.8 (0.9)	5.0 (0.2)	4.4 (0.6)
4	10.2 (0.8)	9.2 (0.8)	7.3 (0.8)	6.3 (0.5)
5	41.1 (5.3)	11.7 (0.9)	7.2 (0.6)	6.5 (0.5)

Table A.20.: Overview of the significance of $D_5 - D_{95}$ differences between the application techniques using rigid registration. Results for the complete treatment course are shown. The Tuckey-Kramer test at 5% significance level has been used. The $D_5 - D_{95}$ results of two techniques showed significant differences for the patients whose numbers is given in the corresponding cell while a "-" indicates no significant differences for that patient.

	interplay	LBT	BT	RDBT
interplay	-	1/2/-/4/5	1/2/3/4/5	1/2/-/4/5
LBT	1/2/-/4/5	-	1/2/-/4/5	1/2/3/4/5
BT	1/2/3/4/5	1/2/-/4/5	-	1/2/3/4/-
RDBT	1/2/-/4/5	1/2/3/4/5	1/2/3/4/-	-

Table A.21.: Mean and SDs of $D_5 - D_{95}$ for all patients when non-rigid registration is used for dose calculation. MLUT calculation was based on rigid registration. Results are for the treatment of one fraction.

patient no	$D_5 - D_{95}$ mean (standard deviation) [% prescribed dose]			
	interplay	lateral BT	BT	RDBT
1	11.1 (0.9)	11.2 (1.1)	8.6 (0.5)	8.2 (0.7)
2	23.2 (2.6)	17.2 (1.0)	16.8 (1.5)	14.8 (1.4)
3	9.2 (0.8)	9.5 (0.7)	7.5 (0.5)	6.9 (0.3)
4	15.1 (1.2)	14.3 (1.2)	9.2 (0.8)	9.1 (0.5)
5	39.4 (9.9)	18.1 (2.1)	12.0 (2.2)	11.8 (1.4)

Table A.22.: Overview of the significance of $D_5 - D_{95}$ differences between the application techniques using non-rigid registration for dose calculation and rigid registration for MLUT calculation. Results are for the treatment of one fraction. The Tuckey-Kramer test at 5% significance level has been used. The $D_5 - D_{95}$ results of two techniques showed significant differences for the patients whose numbers is given in the corresponding cell while a "-" indicates no significant differences for that patient.

	interplay	LBT	BT	RDBT
interplay	-	-/2/-/-/5	1/2/3/4/5	1/2/3/4/5
LBT	-/2/-/-/5	-	1/-/3/4/5	1/2/3/4/5
BT	1/2/3/4/5	1/-/3/4/5	-	-/2/-/-/-
RDBT	1/2/3/4/5	1/2/3/4/5	-/2/-/-/-	-

Table A.23.: Mean and SDs of $D_5 - D_{95}$ for all patients when non-rigid registration is used for dose calculation. MLUT calculation was based on rigid registration. Results for the complete treatment course are shown here.

patient no	$D_5 - D_{95}$ mean (standard deviation) [% prescribed dose]			
	interplay	lateral BT	BT	RDBT
1	7.0 (0.7)	8.0 (0.7)	6.6 (0.5)	6.3 (0.6)
2	21.1 (1.3)	14.0 (0.6)	17.7 (0.8)	12.5 (0.9)
3	5.7 (0.6)	5.8 (0.5)	6.0 (0.2)	5.0 (0.2)
4	9.9 (0.7)	9.4 (0.7)	7.6 (0.5)	7.0 (0.6)
5	40.1 (4.6)	14.7 (1.0)	9.9 (0.9)	9.2 (0.6)

Table A.24.: Overview of the significance of $D_5 - D_{95}$ differences between the application techniques using non-rigid registration for dose calculation and rigid registration for MLUT calculation. Results for the complete treatment course are shown here. The Tuckey-Kramer test at 5% significance level has been used. The $D_5 - D_{95}$ results of two techniques showed significant differences for the patients whose numbers is given in the corresponding cell while a "-" indicates no significant differences for that patient.

	interplay	LBT	BT	RDBT
interplay	-	1/2/-/4/5	1/2/3/4/5	1/2/3/4/5
LBT	1/2/-/4/5	-	1/2/3/4/5	1/2/3/4/5
BT	1/2/3/4/5	1/2/3/4/5	-	1/2/3/4/-
RDBT	1/2/3/4/5	1/2/3/4/5	1/2/3/4/-	-

Table A.25.: Minimum and maximum of the mean as well as the maximum fraction OAR doses for patient 1 with rigid registration based dose calculation. Results are for the treatment of one fraction.

OAR	mean dose _{min}	mean dose _{max}	max dose _{min}	max dose _{max}
carina	7.5 Gy (RBE)	7.8 Gy (RBE)	12.0 Gy (RBE)	12.9 Gy (RBE)
spinal cord	0.2 Gy (RBE)	0.2 Gy (RBE)	2.0 Gy (RBE)	2.8 Gy (RBE)
esophagus	3.0 Gy (RBE)	3.0 Gy (RBE)	11.5 Gy (RBE)	12.9 Gy (RBE)
heart	1.0 Gy (RBE)	1.1 Gy (RBE)	11.3 Gy (RBE)	12.2 Gy (RBE)
vertebral bodies	1.6 Gy (RBE)	1.7 Gy (RBE)	10.1 Gy (RBE)	11.7 Gy (RBE)

(a) Interplay

OAR	mean dose _{min}	mean dose _{max}	max dose _{min}	max dose _{max}
carina	7.7 Gy (RBE)	7.9 Gy (RBE)	11.9 Gy (RBE)	13.0 Gy (RBE)
spinal cord	0.2 Gy (RBE)	0.2 Gy (RBE)	1.6 Gy (RBE)	2.7 Gy (RBE)
esophagus	2.9 Gy (RBE)	3.0 Gy (RBE)	11.5 Gy (RBE)	12.6 Gy (RBE)
heart	1.1 Gy (RBE)	1.1 Gy (RBE)	11.5 Gy (RBE)	12.4 Gy (RBE)
vertebral bodies	1.6 Gy (RBE)	1.7 Gy (RBE)	10.2 Gy (RBE)	11.5 Gy (RBE)

(b) lateral BT

OAR	mean dose _{min}	mean dose _{max}	max dose _{min}	max dose _{max}
carina	7.8 Gy (RBE)	7.9 Gy (RBE)	11.5 Gy (RBE)	12.4 Gy (RBE)
spinal cord	0.2 Gy (RBE)	0.2 Gy (RBE)	1.6 Gy (RBE)	2.2 Gy (RBE)
esophagus	3.0 Gy (RBE)	3.0 Gy (RBE)	11.1 Gy (RBE)	11.6 Gy (RBE)
heart	1.1 Gy (RBE)	1.1 Gy (RBE)	10.9 Gy (RBE)	11.2 Gy (RBE)
vertebral bodies	1.6 Gy (RBE)	1.6 Gy (RBE)	9.9 Gy (RBE)	10.6 Gy (RBE)

(c) BT

OAR	mean dose _{min}	mean dose _{max}	max dose _{min}	max dose _{max}
carina	7.7 Gy (RBE)	7.8 Gy (RBE)	11.0 Gy (RBE)	12.0 Gy (RBE)
spinal cord	0.2 Gy (RBE)	0.2 Gy (RBE)	1.7 Gy (RBE)	2.6 Gy (RBE)
esophagus	3.0 Gy (RBE)	3.0 Gy (RBE)	10.8 Gy (RBE)	11.8 Gy (RBE)
heart	1.1 Gy (RBE)	1.1 Gy (RBE)	10.6 Gy (RBE)	11.1 Gy (RBE)
vertebral bodies	1.7 Gy (RBE)	1.7 Gy (RBE)	10.0 Gy (RBE)	10.7 Gy (RBE)

(d) RDBT

Table A.26.: Minimum and maximum of the fraction mean dose as well as minimum and maximum of the maximal fraction dose for various OARs for patient 2 when dose calculation was based on rigid registration. Interplay, lateral BT, BT and RDBT have been used for Tables A.27a, A.27b, A.27c and A.27d, respectively.

OAR	mean dose _{min}	mean dose _{max}	max dose _{min}	max dose _{max}
spinal cord	0.5 Gy (RBE)	0.8 Gy (RBE)	3.6 Gy (RBE)	5.9 Gy (RBE)
esophagus	0.2 Gy (RBE)	0.2 Gy (RBE)	1.0 Gy (RBE)	2.1 Gy (RBE)
heart	0.0 Gy (RBE)	0.0 Gy (RBE)	4.4 Gy (RBE)	5.4 Gy (RBE)

(a) Interplay

OAR	mean dose _{min}	mean dose _{max}	max dose _{min}	max dose _{max}
spinal cord	0.5 Gy (RBE)	0.9 Gy (RBE)	3.8 Gy (RBE)	5.8 Gy (RBE)
esophagus	0.2 Gy (RBE)	0.2 Gy (RBE)	1.1 Gy (RBE)	1.2 Gy (RBE)
heart	0.1 Gy (RBE)	0.1 Gy (RBE)	4.7 Gy (RBE)	5.7 Gy (RBE)

(b) lateral BT

OAR	mean dose _{min}	mean dose _{max}	max dose _{min}	max dose _{max}
spinal cord	0.5 Gy (RBE)	0.5 Gy (RBE)	2.7 Gy (RBE)	3.8 Gy (RBE)
esophagus	0.2 Gy (RBE)	0.2 Gy (RBE)	1.0 Gy (RBE)	1.0 Gy (RBE)
heart	0.1 Gy (RBE)	0.1 Gy (RBE)	4.3 Gy (RBE)	5.3 Gy (RBE)

(c) BT

OAR	mean dose _{min}	mean dose _{max}	max dose _{min}	max dose _{max}
spinal cord	0.5 Gy (RBE)	0.5 Gy (RBE)	2.9 Gy (RBE)	4.1 Gy (RBE)
esophagus	0.2 Gy (RBE)	0.2 Gy (RBE)	1.0 Gy (RBE)	1.0 Gy (RBE)
heart	0.1 Gy (RBE)	0.1 Gy (RBE)	4.2 Gy (RBE)	4.9 Gy (RBE)

(d) RDBT

Table A.27.: Minimum and maximum of the fraction mean dose as well as minimum and maximum of the maximal fraction dose for various OARs for patient 3 when dose calculation was based on rigid registration. Interplay, lateral BT, BT and RDBT have been used for Tables A.28a, A.28b, A.28c, and A.28d, respectively.

OAR	mean dose _{min}	mean dose _{max}	max dose _{min}	max dose _{max}
spinal cord	0.4 Gy (RBE)	0.4 Gy (RBE)	4.3 Gy (RBE)	5.7 Gy (RBE)
esophagus	3.3 Gy (RBE)	3.3 Gy (RBE)	11.7 Gy (RBE)	13.0 Gy (RBE)
heart	0.0 Gy (RBE)	0.0 Gy (RBE)	0.0 Gy (RBE)	0.0 Gy (RBE)
carina	0.0 Gy (RBE)	0.0 Gy (RBE)	0.0 Gy (RBE)	0.0 Gy (RBE)

(a) Interplay

OAR	mean dose _{min}	mean dose _{max}	max dose _{min}	max dose _{max}
spinal cord	0.4 Gy (RBE)	0.4 Gy (RBE)	4.3 Gy (RBE)	5.7 Gy (RBE)
esophagus	3.2 Gy (RBE)	3.3 Gy (RBE)	11.8 Gy (RBE)	13.0 Gy (RBE)
heart	0.0 Gy (RBE)	0.0 Gy (RBE)	0.0 Gy (RBE)	0.0 Gy (RBE)
carina	0.0 Gy (RBE)	0.0 Gy (RBE)	0.0 Gy (RBE)	0.0 Gy (RBE)

(b) lateral BT

OAR	mean dose _{min}	mean dose _{max}	max dose _{min}	max dose _{max}
spinal cord	0.4 Gy (RBE)	0.4 Gy (RBE)	4.4 Gy (RBE)	4.7 Gy (RBE)
esophagus	3.2 Gy (RBE)	3.3 Gy (RBE)	11.4 Gy (RBE)	11.8 Gy (RBE)
heart	0.0 Gy (RBE)	0.0 Gy (RBE)	0.0 Gy (RBE)	0.0 Gy (RBE)
carina	0.0 Gy (RBE)	0.0 Gy (RBE)	0.0 Gy (RBE)	0.0 Gy (RBE)

(c) BT

OAR	mean dose _{min}	mean dose _{max}	max dose _{min}	max dose _{max}
spinal cord	0.4 Gy (RBE)	0.4 Gy (RBE)	4.4 Gy (RBE)	5.0 Gy (RBE)
esophagus	3.2 Gy (RBE)	3.3 Gy (RBE)	11.4 Gy (RBE)	11.9 Gy (RBE)
heart	0.0 Gy (RBE)	0.0 Gy (RBE)	0.0 Gy (RBE)	0.0 Gy (RBE)
carina	0.0 Gy (RBE)	0.0 Gy (RBE)	0.0 Gy (RBE)	0.0 Gy (RBE)

(d) RDBT

Table A.28.: Minimum and maximum of the fraction mean dose as well as minimum and maximum of the maximal fraction dose for various OARs for patient 4 when dose calculation was based on rigid registration. Interplay, lateral BT, BT and RDBT have been used for Tables A.29a, A.29b, A.29c, and A.29d, respectively.

OAR	mean dose _{min}	mean dose _{max}	max dose _{min}	max dose _{max}
esophagus	0.2 Gy (RBE)	0.2 Gy (RBE)	5.9 Gy (RBE)	7.8 Gy (RBE)
spinal cord	0.0 Gy (RBE)	0.0 Gy (RBE)	0.1 Gy (RBE)	0.2 Gy (RBE)
heart	0.0 Gy (RBE)	0.0 Gy (RBE)	0.0 Gy (RBE)	0.0 Gy (RBE)

(a) Interplay

OAR	mean dose _{min}	mean dose _{max}	max dose _{min}	max dose _{max}
esophagus	0.3 Gy (RBE)	0.3 Gy (RBE)	6.2 Gy (RBE)	8.1 Gy (RBE)
spinal cord	0.0 Gy (RBE)	0.0 Gy (RBE)	0.1 Gy (RBE)	0.1 Gy (RBE)
heart	0.0 Gy (RBE)	0.0 Gy (RBE)	0.0 Gy (RBE)	0.0 Gy (RBE)

(b) lateral BT

OAR	mean dose _{min}	mean dose _{max}	max dose _{min}	max dose _{max}
esophagus	0.3 Gy (RBE)	0.3 Gy (RBE)	5.1 Gy (RBE)	5.8 Gy (RBE)
spinal cord	0.0 Gy (RBE)	0.0 Gy (RBE)	0.1 Gy (RBE)	0.1 Gy (RBE)
heart	0.0 Gy (RBE)	0.0 Gy (RBE)	0.0 Gy (RBE)	0.0 Gy (RBE)

(c) BT

OAR	mean dose _{min}	mean dose _{max}	max dose _{min}	max dose _{max}
esophagus	0.3 Gy (RBE)	0.3 Gy (RBE)	5.4 Gy (RBE)	6.4 Gy (RBE)
spinal cord	0.0 Gy (RBE)	0.0 Gy (RBE)	0.1 Gy (RBE)	0.1 Gy (RBE)
heart	0.0 Gy (RBE)	0.0 Gy (RBE)	0.0 Gy (RBE)	0.0 Gy (RBE)

(d) RDBT

Table A.29.: Minimum and maximum of the fraction mean dose as well as minimum and maximum of the maximal fraction dose for various OARs for patient 5 when dose calculation was based on rigid registration. Interplay, lateral BT, BT and RDBT have been used for Tables A.30a, A.30b, A.30c, and A.30d, respectively.

OAR	mean dose _{min}	mean dose _{max}	max dose _{min}	max dose _{max}
spinal cord	0.4 Gy (RBE)	0.5 Gy (RBE)	3.5 Gy (RBE)	6.1 Gy (RBE)
esophagus	1.2 Gy (RBE)	1.9 Gy (RBE)	8.2 Gy (RBE)	10.5 Gy (RBE)
heart	2.1 Gy (RBE)	2.2 Gy (RBE)	10.7 Gy (RBE)	13.3 Gy (RBE)
carina	0.7 Gy (RBE)	1.7 Gy (RBE)	7.5 Gy (RBE)	10.3 Gy (RBE)

(a) Interplay

OAR	mean dose _{min}	mean dose _{max}	max dose _{min}	max dose _{max}
spinal cord	0.4 Gy (RBE)	0.4 Gy (RBE)	3.0 Gy (RBE)	4.3 Gy (RBE)
esophagus	1.1 Gy (RBE)	1.3 Gy (RBE)	8.7 Gy (RBE)	9.8 Gy (RBE)
heart	2.4 Gy (RBE)	2.5 Gy (RBE)	11.3 Gy (RBE)	13.6 Gy (RBE)
carina	0.2 Gy (RBE)	0.3 Gy (RBE)	4.6 Gy (RBE)	6.0 Gy (RBE)

(b) lateral BT

OAR	mean dose _{min}	mean dose _{max}	max dose _{min}	max dose _{max}
spinal cord	0.4 Gy (RBE)	0.4 Gy (RBE)	2.2 Gy (RBE)	2.8 Gy (RBE)
esophagus	1.0 Gy (RBE)	1.0 Gy (RBE)	7.4 Gy (RBE)	8.1 Gy (RBE)
heart	2.4 Gy (RBE)	2.4 Gy (RBE)	10.6 Gy (RBE)	11.4 Gy (RBE)
carina	0.1 Gy (RBE)	0.2 Gy (RBE)	3.7 Gy (RBE)	4.7 Gy (RBE)

(c) BT

OAR	mean dose _{min}	mean dose _{max}	max dose _{min}	max dose _{max}
spinal cord	0.4 Gy (RBE)	0.4 Gy (RBE)	2.2 Gy (RBE)	3.3 Gy (RBE)
esophagus	1.0 Gy (RBE)	1.1 Gy (RBE)	7.6 Gy (RBE)	8.5 Gy (RBE)
heart	2.4 Gy (RBE)	2.4 Gy (RBE)	10.4 Gy (RBE)	11.4 Gy (RBE)
carina	0.2 Gy (RBE)	0.2 Gy (RBE)	3.8 Gy (RBE)	4.6 Gy (RBE)

(d) RDBT

Table A.30.: Minimum and maximum of the mean as well as the maximum fraction dose for various OARs for patient 1 when dose calculation was based on non-rigid registration.

OAR	mean dose _{min}	mean dose _{max}	max dose _{min}	max dose _{max}
carina	7.5 Gy (RBE)	7.8 Gy (RBE)	12.0 Gy (RBE)	12.9 Gy (RBE)
spinal cord	0.2 Gy (RBE)	0.2 Gy (RBE)	2.0 Gy (RBE)	2.8 Gy (RBE)
esophagus	3.0 Gy (RBE)	3.0 Gy (RBE)	11.5 Gy (RBE)	12.9 Gy (RBE)
heart	1.0 Gy (RBE)	1.1 Gy (RBE)	11.3 Gy (RBE)	12.2 Gy (RBE)
vertebral bodies	1.6 Gy (RBE)	1.7 Gy (RBE)	10.1 Gy (RBE)	11.7 Gy (RBE)

(a) Interplay

OAR	mean dose _{min}	mean dose _{max}	max dose _{min}	max dose _{max}
carina	7.7 Gy (RBE)	7.9 Gy (RBE)	11.9 Gy (RBE)	13.0 Gy (RBE)
spinal cord	0.2 Gy (RBE)	0.2 Gy (RBE)	1.6 Gy (RBE)	2.7 Gy (RBE)
esophagus	2.9 Gy (RBE)	3.0 Gy (RBE)	11.5 Gy (RBE)	12.6 Gy (RBE)
heart	1.1 Gy (RBE)	1.1 Gy (RBE)	11.5 Gy (RBE)	12.4 Gy (RBE)
vertebral bodies	1.6 Gy (RBE)	1.7 Gy (RBE)	10.2 Gy (RBE)	11.5 Gy (RBE)

(b) lateral BT

OAR	mean dose _{min}	mean dose _{max}	max dose _{min}	max dose _{max}
carina	7.8 Gy (RBE)	7.9 Gy (RBE)	11.5 Gy (RBE)	12.4 Gy (RBE)
spinal cord	0.2 Gy (RBE)	0.2 Gy (RBE)	1.6 Gy (RBE)	2.2 Gy (RBE)
esophagus	3.0 Gy (RBE)	3.0 Gy (RBE)	11.1 Gy (RBE)	11.6 Gy (RBE)
heart	1.1 Gy (RBE)	1.1 Gy (RBE)	10.9 Gy (RBE)	11.2 Gy (RBE)
vertebral bodies	1.6 Gy (RBE)	1.6 Gy (RBE)	9.9 Gy (RBE)	10.6 Gy (RBE)

(c) BT

OAR	mean dose _{min}	mean dose _{max}	max dose _{min}	max dose _{max}
carina	7.7 Gy (RBE)	7.8 Gy (RBE)	11.0 Gy (RBE)	12.0 Gy (RBE)
spinal cord	0.2 Gy (RBE)	0.2 Gy (RBE)	1.7 Gy (RBE)	2.6 Gy (RBE)
esophagus	3.0 Gy (RBE)	3.0 Gy (RBE)	10.8 Gy (RBE)	11.8 Gy (RBE)
heart	1.1 Gy (RBE)	1.1 Gy (RBE)	10.6 Gy (RBE)	11.1 Gy (RBE)
vertebral bodies	1.7 Gy (RBE)	1.7 Gy (RBE)	10.0 Gy (RBE)	10.7 Gy (RBE)

(d) RDBT

Table A.31.: Minimum and maximum of the fraction mean dose as well as minimum and maximum of the maximal fraction dose for various OARs for patient 2 when dose calculation was based on non-rigid registration. Interplay, lateral BT, BT and RDBT have been used for Tables A.32a, A.32b, A.32c, and A.32d, respectively.

OAR	mean dose _{min}	mean dose _{max}	max dose _{min}	max dose _{max}
spinal cord	0.5 Gy (RBE)	0.7 Gy (RBE)	3.4 Gy (RBE)	5.0 Gy (RBE)
esophagus	0.2 Gy (RBE)	0.2 Gy (RBE)	1.1 Gy (RBE)	2.5 Gy (RBE)
heart	0.0 Gy (RBE)	0.0 Gy (RBE)	3.6 Gy (RBE)	4.5 Gy (RBE)

(a) Interplay

OAR	mean dose _{min}	mean dose _{max}	max dose _{min}	max dose _{max}
spinal cord	0.5 Gy (RBE)	0.7 Gy (RBE)	3.4 Gy (RBE)	5.1 Gy (RBE)
esophagus	0.2 Gy (RBE)	0.2 Gy (RBE)	1.0 Gy (RBE)	2.4 Gy (RBE)
heart	0.1 Gy (RBE)	0.1 Gy (RBE)	4.7 Gy (RBE)	5.5 Gy (RBE)

(b) lateral BT

OAR	mean dose _{min}	mean dose _{max}	max dose _{min}	max dose _{max}
spinal cord	0.4 Gy (RBE)	0.5 Gy (RBE)	2.2 Gy (RBE)	3.8 Gy (RBE)
esophagus	0.2 Gy (RBE)	0.2 Gy (RBE)	1.0 Gy (RBE)	1.2 Gy (RBE)
heart	0.1 Gy (RBE)	0.1 Gy (RBE)	4.1 Gy (RBE)	4.7 Gy (RBE)

(c) BT

OAR	mean dose _{min}	mean dose _{max}	max dose _{min}	max dose _{max}
spinal cord	0.4 Gy (RBE)	0.5 Gy (RBE)	2.4 Gy (RBE)	4.0 Gy (RBE)
esophagus	0.2 Gy (RBE)	0.2 Gy (RBE)	1.0 Gy (RBE)	1.5 Gy (RBE)
heart	0.1 Gy (RBE)	0.1 Gy (RBE)	4.0 Gy (RBE)	4.5 Gy (RBE)

(d) RDBT

Table A.32.: Minimum and maximum of the fraction mean dose as well as minimum and maximum of the maximal fraction dose for various OARs for patient 3 when dose calculation was based on non-rigid registration. Interplay, lateral BT, BT and RDBT have been used for Tables A.33a, A.33b, A.33c, and A.33d, respectively.

OAR	mean dose _{min}	mean dose _{max}	max dose _{min}	max dose _{max}
spinal cord	0.4 Gy (RBE)	0.4 Gy (RBE)	4.4 Gy (RBE)	5.7 Gy (RBE)
esophagus	3.3 Gy (RBE)	3.3 Gy (RBE)	12.1 Gy (RBE)	13.0 Gy (RBE)
heart	0.0 Gy (RBE)	0.0 Gy (RBE)	0.0 Gy (RBE)	0.0 Gy (RBE)
carina	0.0 Gy (RBE)	0.0 Gy (RBE)	0.0 Gy (RBE)	0.0 Gy (RBE)

(a) Interplay

OAR	mean dose _{min}	mean dose _{max}	max dose _{min}	max dose _{max}
spinal cord	0.4 Gy (RBE)	0.4 Gy (RBE)	4.4 Gy (RBE)	5.7 Gy (RBE)
esophagus	3.3 Gy (RBE)	3.4 Gy (RBE)	12.1 Gy (RBE)	12.9 Gy (RBE)
heart	0.0 Gy (RBE)	0.0 Gy (RBE)	0.0 Gy (RBE)	0.0 Gy (RBE)
carina	0.0 Gy (RBE)	0.0 Gy (RBE)	0.0 Gy (RBE)	0.0 Gy (RBE)

(b) lateral BT

OAR	mean dose _{min}	mean dose _{max}	max dose _{min}	max dose _{max}
spinal cord	0.4 Gy (RBE)	0.4 Gy (RBE)	4.3 Gy (RBE)	4.8 Gy (RBE)
esophagus	3.3 Gy (RBE)	3.3 Gy (RBE)	11.6 Gy (RBE)	12.1 Gy (RBE)
heart	0.0 Gy (RBE)	0.0 Gy (RBE)	0.0 Gy (RBE)	0.0 Gy (RBE)
carina	0.0 Gy (RBE)	0.0 Gy (RBE)	0.0 Gy (RBE)	0.0 Gy (RBE)

(c) BT

OAR	mean dose _{min}	mean dose _{max}	max dose _{min}	max dose _{max}
spinal cord	0.4 Gy (RBE)	0.4 Gy (RBE)	4.2 Gy (RBE)	5.0 Gy (RBE)
esophagus	3.2 Gy (RBE)	3.3 Gy (RBE)	11.4 Gy (RBE)	11.9 Gy (RBE)
heart	0.0 Gy (RBE)	0.0 Gy (RBE)	0.0 Gy (RBE)	0.0 Gy (RBE)
carina	0.0 Gy (RBE)	0.0 Gy (RBE)	0.0 Gy (RBE)	0.0 Gy (RBE)

(d) RDBT

Table A.33.: Minimum and maximum of the fraction mean dose as well as minimum and maximum of the maximal fraction dose for various OARs for patient 4 when dose calculation was based on non-rigid registration. Interplay, lateral BT, BT and RDBT have been used for Tables A.34a, A.34b, A.34c, and A.34d, respectively.

OAR	mean dose _{min}	mean dose _{max}	max dose _{min}	max dose _{max}
esophagus	0.2 Gy (RBE)	0.2 Gy (RBE)	5.8 Gy (RBE)	8.1 Gy (RBE)
spinal cord	0.0 Gy (RBE)	0.0 Gy (RBE)	0.1 Gy (RBE)	0.1 Gy (RBE)
heart	0.0 Gy (RBE)	0.0 Gy (RBE)	0.0 Gy (RBE)	0.0 Gy (RBE)

(a) Interplay

OAR	mean dose _{min}	mean dose _{max}	max dose _{min}	max dose _{max}
esophagus	0.3 Gy (RBE)	0.3 Gy (RBE)	5.5 Gy (RBE)	8.3 Gy (RBE)
spinal cord	0.0 Gy (RBE)	0.0 Gy (RBE)	0.1 Gy (RBE)	0.1 Gy (RBE)
heart	0.0 Gy (RBE)	0.0 Gy (RBE)	0.0 Gy (RBE)	0.0 Gy (RBE)

(b) lateral BT

OAR	mean dose _{min}	mean dose _{max}	max dose _{min}	max dose _{max}
esophagus	0.3 Gy (RBE)	0.3 Gy (RBE)	5.0 Gy (RBE)	6.5 Gy (RBE)
spinal cord	0.0 Gy (RBE)	0.0 Gy (RBE)	0.1 Gy (RBE)	0.1 Gy (RBE)
heart	0.0 Gy (RBE)	0.0 Gy (RBE)	0.0 Gy (RBE)	0.0 Gy (RBE)

(c) BT

OAR	mean dose _{min}	mean dose _{max}	max dose _{min}	max dose _{max}
esophagus	0.3 Gy (RBE)	0.3 Gy (RBE)	5.3 Gy (RBE)	6.8 Gy (RBE)
spinal cord	0.0 Gy (RBE)	0.0 Gy (RBE)	0.1 Gy (RBE)	0.1 Gy (RBE)
heart	0.0 Gy (RBE)	0.0 Gy (RBE)	0.0 Gy (RBE)	0.0 Gy (RBE)

(d) RDBT

Table A.34.: Minimum and maximum of the fraction mean dose as well as minimum and maximum of the maximal fraction dose for various OARs for patient 5 when dose calculation was based on non-rigid registration. Interplay, lateral BT, BT and RDBT have been used for Tables A.35a, A.35b, A.35c, and A.35d, respectively.

OAR	mean dose _{min}	mean dose _{max}	max dose _{min}	max dose _{max}
spinal cord	0.4 Gy (RBE)	0.4 Gy (RBE)	2.6 Gy (RBE)	5.6 Gy (RBE)
esophagus	1.2 Gy (RBE)	1.8 Gy (RBE)	8.8 Gy (RBE)	10.5 Gy (RBE)
heart	2.1 Gy (RBE)	2.2 Gy (RBE)	10.2 Gy (RBE)	12.9 Gy (RBE)
carina	0.4 Gy (RBE)	0.9 Gy (RBE)	5.9 Gy (RBE)	7.9 Gy (RBE)

(a) Interplay

OAR	mean dose _{min}	mean dose _{max}	max dose _{min}	max dose _{max}
spinal cord	0.4 Gy (RBE)	0.4 Gy (RBE)	2.5 Gy (RBE)	4.2 Gy (RBE)
esophagus	1.0 Gy (RBE)	1.2 Gy (RBE)	8.0 Gy (RBE)	11.5 Gy (RBE)
heart	2.3 Gy (RBE)	2.4 Gy (RBE)	11.1 Gy (RBE)	12.5 Gy (RBE)
carina	0.0 Gy (RBE)	0.1 Gy (RBE)	1.0 Gy (RBE)	4.0 Gy (RBE)

(b) lateral BT

OAR	mean dose _{min}	mean dose _{max}	max dose _{min}	max dose _{max}
spinal cord	0.3 Gy (RBE)	0.4 Gy (RBE)	1.9 Gy (RBE)	2.8 Gy (RBE)
esophagus	0.9 Gy (RBE)	1.0 Gy (RBE)	7.2 Gy (RBE)	9.4 Gy (RBE)
heart	2.3 Gy (RBE)	2.3 Gy (RBE)	10.7 Gy (RBE)	12.1 Gy (RBE)
carina	0.0 Gy (RBE)	0.1 Gy (RBE)	1.1 Gy (RBE)	3.7 Gy (RBE)

(c) BT

OAR	mean dose _{min}	mean dose _{max}	max dose _{min}	max dose _{max}
spinal cord	0.3 Gy (RBE)	0.4 Gy (RBE)	2.0 Gy (RBE)	2.9 Gy (RBE)
esophagus	0.9 Gy (RBE)	1.1 Gy (RBE)	7.4 Gy (RBE)	9.8 Gy (RBE)
heart	2.2 Gy (RBE)	2.3 Gy (RBE)	10.6 Gy (RBE)	12.4 Gy (RBE)
carina	0.0 Gy (RBE)	0.1 Gy (RBE)	0.9 Gy (RBE)	3.7 Gy (RBE)

(d) RDBT

Table A.35.: Minimum and maximum of the mean as well as the maximum total OAR doses for patient 1 with rigid registration based dose calculation. Results for the total treatment course are shown here.

OAR	mean dose _{min}	mean dose _{max}	max dose _{min}	max dose _{max}
carina	19.7 Gy (RBE)	20.3 Gy (RBE)	29.9 Gy (RBE)	33.6 Gy (RBE)
spinal cord	0.6 Gy (RBE)	0.6 Gy (RBE)	4.2 Gy (RBE)	5.3 Gy (RBE)
esophagus	7.7 Gy (RBE)	7.8 Gy (RBE)	29.8 Gy (RBE)	33.2 Gy (RBE)
heart	2.5 Gy (RBE)	2.5 Gy (RBE)	28.2 Gy (RBE)	31.2 Gy (RBE)
vertebral bodies	3.9 Gy (RBE)	4.0 Gy (RBE)	25.9 Gy (RBE)	28.7 Gy (RBE)

(a) Interplay

OAR	mean dose _{min}	mean dose _{max}	max dose _{min}	max dose _{max}
carina	20.3 Gy (RBE)	20.6 Gy (RBE)	30.2 Gy (RBE)	33.8 Gy (RBE)
spinal cord	0.6 Gy (RBE)	0.6 Gy (RBE)	4.1 Gy (RBE)	5.4 Gy (RBE)
esophagus	7.6 Gy (RBE)	7.6 Gy (RBE)	29.4 Gy (RBE)	32.0 Gy (RBE)
heart	2.7 Gy (RBE)	2.7 Gy (RBE)	28.7 Gy (RBE)	31.7 Gy (RBE)
vertebral bodies	4.0 Gy (RBE)	4.0 Gy (RBE)	26.2 Gy (RBE)	29.3 Gy (RBE)

(b) lateral BT

OAR	mean dose _{min}	mean dose _{max}	max dose _{min}	max dose _{max}
carina	20.6 Gy (RBE)	20.7 Gy (RBE)	30.8 Gy (RBE)	33.6 Gy (RBE)
spinal cord	0.6 Gy (RBE)	0.6 Gy (RBE)	3.9 Gy (RBE)	4.8 Gy (RBE)
esophagus	7.6 Gy (RBE)	7.6 Gy (RBE)	29.6 Gy (RBE)	31.6 Gy (RBE)
heart	2.7 Gy (RBE)	2.7 Gy (RBE)	28.2 Gy (RBE)	29.7 Gy (RBE)
vertebral bodies	3.9 Gy (RBE)	3.9 Gy (RBE)	26.5 Gy (RBE)	27.6 Gy (RBE)

(c) BT

OAR	mean dose _{min}	mean dose _{max}	max dose _{min}	max dose _{max}
carina	20.2 Gy (RBE)	20.3 Gy (RBE)	29.4 Gy (RBE)	32.0 Gy (RBE)
spinal cord	0.6 Gy (RBE)	0.6 Gy (RBE)	4.0 Gy (RBE)	5.1 Gy (RBE)
esophagus	7.6 Gy (RBE)	7.7 Gy (RBE)	28.6 Gy (RBE)	31.3 Gy (RBE)
heart	2.6 Gy (RBE)	2.7 Gy (RBE)	27.6 Gy (RBE)	29.3 Gy (RBE)
vertebral bodies	4.1 Gy (RBE)	4.1 Gy (RBE)	26.6 Gy (RBE)	28.3 Gy (RBE)

(d) RDBT

Table A.36.: Minimum and maximum of the total mean dose as well as minimum and maximum of the maximal total dose for various OARs for patient 2 when dose calculation was based on rigid registration. Results for the complete treatment course are shown here. Interplay, lateral BT, BT and RDBT have been used for Tables A.37a, A.37b, A.37c, and A.37d, respectively.

OAR	mean dose _{min}	mean dose _{max}	max dose _{min}	max dose _{max}
spinal cord	1.5 Gy (RBE)	1.8 Gy (RBE)	8.1 Gy (RBE)	10.2 Gy (RBE)
esophagus	0.6 Gy (RBE)	0.6 Gy (RBE)	2.8 Gy (RBE)	3.6 Gy (RBE)
heart	0.1 Gy (RBE)	0.1 Gy (RBE)	8.2 Gy (RBE)	10.0 Gy (RBE)

(a) Interplay

OAR	mean dose _{min}	mean dose _{max}	max dose _{min}	max dose _{max}
spinal cord	1.5 Gy (RBE)	1.8 Gy (RBE)	8.3 Gy (RBE)	10.4 Gy (RBE)
esophagus	0.6 Gy (RBE)	0.6 Gy (RBE)	2.8 Gy (RBE)	2.8 Gy (RBE)
heart	0.2 Gy (RBE)	0.2 Gy (RBE)	9.4 Gy (RBE)	11.0 Gy (RBE)

(b) lateral BT

OAR	mean dose _{min}	mean dose _{max}	max dose _{min}	max dose _{max}
spinal cord	1.2 Gy (RBE)	1.3 Gy (RBE)	6.5 Gy (RBE)	7.9 Gy (RBE)
esophagus	0.6 Gy (RBE)	0.6 Gy (RBE)	2.6 Gy (RBE)	2.6 Gy (RBE)
heart	0.2 Gy (RBE)	0.2 Gy (RBE)	9.1 Gy (RBE)	10.3 Gy (RBE)

(c) BT

OAR	mean dose _{min}	mean dose _{max}	max dose _{min}	max dose _{max}
spinal cord	1.3 Gy (RBE)	1.3 Gy (RBE)	6.8 Gy (RBE)	8.0 Gy (RBE)
esophagus	0.6 Gy (RBE)	0.6 Gy (RBE)	2.6 Gy (RBE)	2.7 Gy (RBE)
heart	0.2 Gy (RBE)	0.2 Gy (RBE)	9.1 Gy (RBE)	10.1 Gy (RBE)

(d) RDBT

Table A.37.: Minimum and maximum of the total mean dose as well as minimum and maximum of the maximal total dose for various OARs for patient 3 when dose calculation was based on rigid registration. Results for the complete treatment course are shown here. Interplay, lateral BT, BT and RDBT have been used for Tables A.38a, A.38b, A.38c, and A.38d, respectively.

OAR	mean dose _{min}	mean dose _{max}	max dose _{min}	max dose _{max}
spinal cord	1.0 Gy (RBE)	1.0 Gy (RBE)	9.2 Gy (RBE)	10.8 Gy (RBE)
esophagus	8.2 Gy (RBE)	8.3 Gy (RBE)	30.9 Gy (RBE)	34.0 Gy (RBE)
heart	0.0 Gy (RBE)	0.0 Gy (RBE)	0.0 Gy (RBE)	0.0 Gy (RBE)
carina	0.0 Gy (RBE)	0.0 Gy (RBE)	0.0 Gy (RBE)	0.0 Gy (RBE)

(a) Interplay

OAR	mean dose _{min}	mean dose _{max}	max dose _{min}	max dose _{max}
spinal cord	1.0 Gy (RBE)	1.0 Gy (RBE)	9.3 Gy (RBE)	10.9 Gy (RBE)
esophagus	8.3 Gy (RBE)	8.4 Gy (RBE)	31.1 Gy (RBE)	34.0 Gy (RBE)
heart	0.0 Gy (RBE)	0.0 Gy (RBE)	0.0 Gy (RBE)	0.0 Gy (RBE)
carina	0.0 Gy (RBE)	0.0 Gy (RBE)	0.0 Gy (RBE)	0.0 Gy (RBE)

(b) lateral BT

OAR	mean dose _{min}	mean dose _{max}	max dose _{min}	max dose _{max}
spinal cord	0.9 Gy (RBE)	0.9 Gy (RBE)	9.4 Gy (RBE)	9.9 Gy (RBE)
esophagus	8.1 Gy (RBE)	8.1 Gy (RBE)	30.7 Gy (RBE)	32.2 Gy (RBE)
heart	0.0 Gy (RBE)	0.0 Gy (RBE)	0.0 Gy (RBE)	0.0 Gy (RBE)
carina	0.0 Gy (RBE)	0.0 Gy (RBE)	0.0 Gy (RBE)	0.0 Gy (RBE)

(c) BT

OAR	mean dose _{min}	mean dose _{max}	max dose _{min}	max dose _{max}
spinal cord	0.9 Gy (RBE)	0.9 Gy (RBE)	9.3 Gy (RBE)	10.2 Gy (RBE)
esophagus	8.1 Gy (RBE)	8.1 Gy (RBE)	30.2 Gy (RBE)	32.2 Gy (RBE)
heart	0.0 Gy (RBE)	0.0 Gy (RBE)	0.0 Gy (RBE)	0.0 Gy (RBE)
carina	0.0 Gy (RBE)	0.0 Gy (RBE)	0.0 Gy (RBE)	0.0 Gy (RBE)

(d) RDBT

Table A.38.: Minimum and maximum of the total mean dose as well as minimum and maximum of the maximal total dose for various OARs for patient 4 when dose calculation was based on rigid registration. Results for the complete treatment course are shown here. Interplay, lateral BT, BT and RDBT have been used for Tables A.39a, A.39b, A.39c, and A.39d, respectively.

OAR	mean dose _{min}	mean dose _{max}	max dose _{min}	max dose _{max}
esophagus	0.6 Gy (RBE)	0.6 Gy (RBE)	11.0 Gy (RBE)	14.2 Gy (RBE)
spinal cord	0.0 Gy (RBE)	0.0 Gy (RBE)	0.5 Gy (RBE)	0.5 Gy (RBE)
heart	0.0 Gy (RBE)	0.0 Gy (RBE)	0.0 Gy (RBE)	0.0 Gy (RBE)

(a) Interplay

OAR	mean dose _{min}	mean dose _{max}	max dose _{min}	max dose _{max}
esophagus	0.7 Gy (RBE)	0.7 Gy (RBE)	11.1 Gy (RBE)	13.7 Gy (RBE)
spinal cord	0.0 Gy (RBE)	0.0 Gy (RBE)	0.4 Gy (RBE)	0.5 Gy (RBE)
heart	0.0 Gy (RBE)	0.0 Gy (RBE)	0.0 Gy (RBE)	0.0 Gy (RBE)

(b) lateral BT

OAR	mean dose _{min}	mean dose _{max}	max dose _{min}	max dose _{max}
esophagus	0.7 Gy (RBE)	0.7 Gy (RBE)	10.2 Gy (RBE)	11.4 Gy (RBE)
spinal cord	0.0 Gy (RBE)	0.0 Gy (RBE)	0.4 Gy (RBE)	0.4 Gy (RBE)
heart	0.0 Gy (RBE)	0.0 Gy (RBE)	0.0 Gy (RBE)	0.0 Gy (RBE)

(c) BT

OAR	mean dose _{min}	mean dose _{max}	max dose _{min}	max dose _{max}
esophagus	0.7 Gy (RBE)	0.7 Gy (RBE)	10.5 Gy (RBE)	12.2 Gy (RBE)
spinal cord	0.0 Gy (RBE)	0.0 Gy (RBE)	0.4 Gy (RBE)	0.5 Gy (RBE)
heart	0.0 Gy (RBE)	0.0 Gy (RBE)	0.0 Gy (RBE)	0.0 Gy (RBE)

(d) RDBT

Table A.39.: Minimum and maximum of the total mean dose as well as minimum and maximum of the maximal total dose for various OARs for patient 5 when dose calculation was based on rigid registration. Results for the complete treatment course are shown here. Interplay, lateral BT, BT and RDBT have been used for Tables A.40a, A.40b, A.40c, and A.40d, respectively.

OAR	mean dose _{min}	mean dose _{max}	max dose _{min}	max dose _{max}
spinal cord	1.1 Gy (RBE)	1.2 Gy (RBE)	6.9 Gy (RBE)	11.5 Gy (RBE)
esophagus	3.4 Gy (RBE)	3.9 Gy (RBE)	19.8 Gy (RBE)	25.5 Gy (RBE)
heart	5.0 Gy (RBE)	5.3 Gy (RBE)	26.8 Gy (RBE)	33.1 Gy (RBE)
carina	2.5 Gy (RBE)	3.5 Gy (RBE)	17.7 Gy (RBE)	23.3 Gy (RBE)

(a) Interplay

OAR	mean dose _{min}	mean dose _{max}	max dose _{min}	max dose _{max}
spinal cord	1.0 Gy (RBE)	1.1 Gy (RBE)	6.4 Gy (RBE)	7.7 Gy (RBE)
esophagus	2.7 Gy (RBE)	3.0 Gy (RBE)	18.5 Gy (RBE)	23.9 Gy (RBE)
heart	5.9 Gy (RBE)	6.0 Gy (RBE)	28.8 Gy (RBE)	33.2 Gy (RBE)
carina	0.5 Gy (RBE)	0.6 Gy (RBE)	10.1 Gy (RBE)	12.1 Gy (RBE)

(b) lateral BT

OAR	mean dose _{min}	mean dose _{max}	max dose _{min}	max dose _{max}
spinal cord	0.9 Gy (RBE)	1.0 Gy (RBE)	5.4 Gy (RBE)	6.2 Gy (RBE)
esophagus	2.4 Gy (RBE)	2.4 Gy (RBE)	17.4 Gy (RBE)	18.9 Gy (RBE)
heart	5.8 Gy (RBE)	5.8 Gy (RBE)	29.1 Gy (RBE)	30.3 Gy (RBE)
carina	0.4 Gy (RBE)	0.4 Gy (RBE)	8.3 Gy (RBE)	10.0 Gy (RBE)

(c) BT

OAR	mean dose _{min}	mean dose _{max}	max dose _{min}	max dose _{max}
spinal cord	1.0 Gy (RBE)	1.0 Gy (RBE)	5.7 Gy (RBE)	6.8 Gy (RBE)
esophagus	2.5 Gy (RBE)	2.5 Gy (RBE)	17.9 Gy (RBE)	19.9 Gy (RBE)
heart	5.7 Gy (RBE)	5.7 Gy (RBE)	28.2 Gy (RBE)	29.6 Gy (RBE)
carina	0.4 Gy (RBE)	0.4 Gy (RBE)	8.5 Gy (RBE)	9.8 Gy (RBE)

(d) RDBT

Table A.40.: Minimum and maximum of the mean as well as the maximum total dose for various OARs for patient 1 when dose calculation was based on non-rigid registration. Results for the complete treatment course are shown here.

OAR	mean dose _{min}	mean dose _{max}	max dose _{min}	max dose _{max}
carina	19.7 Gy (RBE)	20.3 Gy (RBE)	29.9 Gy (RBE)	33.6 Gy (RBE)
spinal cord	0.6 Gy (RBE)	0.6 Gy (RBE)	4.2 Gy (RBE)	5.3 Gy (RBE)
esophagus	7.7 Gy (RBE)	7.8 Gy (RBE)	29.8 Gy (RBE)	33.2 Gy (RBE)
heart	2.5 Gy (RBE)	2.5 Gy (RBE)	28.2 Gy (RBE)	31.2 Gy (RBE)
vertebral bodies	3.9 Gy (RBE)	4.0 Gy (RBE)	25.9 Gy (RBE)	28.7 Gy (RBE)

(a) Interplay

OAR	mean dose _{min}	mean dose _{max}	max dose _{min}	max dose _{max}
carina	20.3 Gy (RBE)	20.6 Gy (RBE)	30.2 Gy (RBE)	33.8 Gy (RBE)
spinal cord	0.6 Gy (RBE)	0.6 Gy (RBE)	4.1 Gy (RBE)	5.4 Gy (RBE)
esophagus	7.6 Gy (RBE)	7.6 Gy (RBE)	29.4 Gy (RBE)	32.0 Gy (RBE)
heart	2.7 Gy (RBE)	2.7 Gy (RBE)	28.7 Gy (RBE)	31.7 Gy (RBE)
vertebral bodies	4.0 Gy (RBE)	4.0 Gy (RBE)	26.2 Gy (RBE)	29.3 Gy (RBE)

(b) lateral BT

OAR	mean dose _{min}	mean dose _{max}	max dose _{min}	max dose _{max}
carina	20.6 Gy (RBE)	20.7 Gy (RBE)	30.8 Gy (RBE)	33.6 Gy (RBE)
spinal cord	0.6 Gy (RBE)	0.6 Gy (RBE)	3.9 Gy (RBE)	4.8 Gy (RBE)
esophagus	7.6 Gy (RBE)	7.6 Gy (RBE)	29.6 Gy (RBE)	31.6 Gy (RBE)
heart	2.7 Gy (RBE)	2.7 Gy (RBE)	28.2 Gy (RBE)	29.7 Gy (RBE)
vertebral bodies	3.9 Gy (RBE)	3.9 Gy (RBE)	26.5 Gy (RBE)	27.6 Gy (RBE)

(c) BT

OAR	mean dose _{min}	mean dose _{max}	max dose _{min}	max dose _{max}
carina	20.2 Gy (RBE)	20.3 Gy (RBE)	29.4 Gy (RBE)	32.0 Gy (RBE)
spinal cord	0.6 Gy (RBE)	0.6 Gy (RBE)	4.0 Gy (RBE)	5.1 Gy (RBE)
esophagus	7.6 Gy (RBE)	7.7 Gy (RBE)	28.6 Gy (RBE)	31.3 Gy (RBE)
heart	2.6 Gy (RBE)	2.7 Gy (RBE)	27.6 Gy (RBE)	29.3 Gy (RBE)
vertebral bodies	4.1 Gy (RBE)	4.1 Gy (RBE)	26.6 Gy (RBE)	28.3 Gy (RBE)

(d) RDBT

Table A.41.: Minimum and maximum of the total mean dose as well as minimum and maximum of the maximal total dose for various OARs for patient 2 when dose calculation was based on non-rigid registration. Results for the complete treatment course are shown here. Interplay, lateral BT, BT and RDBT have been used for Tables A.42a, A.42b, A.42c, and A.42d, respectively.

OAR	mean dose _{min}	mean dose _{max}	max dose _{min}	max dose _{max}
spinal cord	1.4 Gy (RBE)	1.5 Gy (RBE)	7.6 Gy (RBE)	9.3 Gy (RBE)
esophagus	0.6 Gy (RBE)	0.6 Gy (RBE)	2.8 Gy (RBE)	4.0 Gy (RBE)
heart	0.1 Gy (RBE)	0.1 Gy (RBE)	7.4 Gy (RBE)	8.7 Gy (RBE)

(a) Interplay

OAR	mean dose _{min}	mean dose _{max}	max dose _{min}	max dose _{max}
spinal cord	1.4 Gy (RBE)	1.6 Gy (RBE)	7.6 Gy (RBE)	9.4 Gy (RBE)
esophagus	0.6 Gy (RBE)	0.7 Gy (RBE)	2.8 Gy (RBE)	4.2 Gy (RBE)
heart	0.2 Gy (RBE)	0.2 Gy (RBE)	9.0 Gy (RBE)	10.5 Gy (RBE)

(b) lateral BT

OAR	mean dose _{min}	mean dose _{max}	max dose _{min}	max dose _{max}
spinal cord	1.2 Gy (RBE)	1.2 Gy (RBE)	5.0 Gy (RBE)	7.5 Gy (RBE)
esophagus	0.6 Gy (RBE)	0.6 Gy (RBE)	2.5 Gy (RBE)	2.7 Gy (RBE)
heart	0.2 Gy (RBE)	0.2 Gy (RBE)	8.3 Gy (RBE)	9.3 Gy (RBE)

(c) BT

OAR	mean dose _{min}	mean dose _{max}	max dose _{min}	max dose _{max}
spinal cord	1.2 Gy (RBE)	1.2 Gy (RBE)	5.1 Gy (RBE)	7.6 Gy (RBE)
esophagus	0.6 Gy (RBE)	0.6 Gy (RBE)	2.5 Gy (RBE)	2.9 Gy (RBE)
heart	0.2 Gy (RBE)	0.2 Gy (RBE)	8.4 Gy (RBE)	9.2 Gy (RBE)

(d) RDBT

Table A.42.: Minimum and maximum of the total mean dose as well as minimum and maximum of the maximal total dose for various OARs for patient 3 when dose calculation was based on non-rigid registration. Results for the complete treatment course are shown here. Interplay, lateral BT, BT and RDBT have been used for Tables A.43a, A.43b, A.43c, and A.43d, respectively.

OAR	mean dose _{min}	mean dose _{max}	max dose _{min}	max dose _{max}
spinal cord	1.0 Gy (RBE)	1.0 Gy (RBE)	9.2 Gy (RBE)	10.9 Gy (RBE)
esophagus	8.3 Gy (RBE)	8.4 Gy (RBE)	30.9 Gy (RBE)	33.6 Gy (RBE)
heart	0.0 Gy (RBE)	0.0 Gy (RBE)	0.0 Gy (RBE)	0.0 Gy (RBE)
carina	0.0 Gy (RBE)	0.0 Gy (RBE)	0.0 Gy (RBE)	0.0 Gy (RBE)

(a) Interplay

OAR	mean dose _{min}	mean dose _{max}	max dose _{min}	max dose _{max}
spinal cord	1.0 Gy (RBE)	1.0 Gy (RBE)	9.3 Gy (RBE)	10.9 Gy (RBE)
esophagus	8.3 Gy (RBE)	8.4 Gy (RBE)	31.0 Gy (RBE)	33.6 Gy (RBE)
heart	0.0 Gy (RBE)	0.0 Gy (RBE)	0.0 Gy (RBE)	0.0 Gy (RBE)
carina	0.0 Gy (RBE)	0.0 Gy (RBE)	0.0 Gy (RBE)	0.0 Gy (RBE)

(b) lateral BT

OAR	mean dose _{min}	mean dose _{max}	max dose _{min}	max dose _{max}
spinal cord	0.9 Gy (RBE)	1.0 Gy (RBE)	9.2 Gy (RBE)	9.9 Gy (RBE)
esophagus	8.2 Gy (RBE)	8.2 Gy (RBE)	30.7 Gy (RBE)	32.6 Gy (RBE)
heart	0.0 Gy (RBE)	0.0 Gy (RBE)	0.0 Gy (RBE)	0.0 Gy (RBE)
carina	0.0 Gy (RBE)	0.0 Gy (RBE)	0.0 Gy (RBE)	0.0 Gy (RBE)

(c) BT

OAR	mean dose _{min}	mean dose _{max}	max dose _{min}	max dose _{max}
spinal cord	0.9 Gy (RBE)	1.0 Gy (RBE)	9.1 Gy (RBE)	10.2 Gy (RBE)
esophagus	8.1 Gy (RBE)	8.2 Gy (RBE)	30.1 Gy (RBE)	32.5 Gy (RBE)
heart	0.0 Gy (RBE)	0.0 Gy (RBE)	0.0 Gy (RBE)	0.0 Gy (RBE)
carina	0.0 Gy (RBE)	0.0 Gy (RBE)	0.0 Gy (RBE)	0.0 Gy (RBE)

(d) RDBT

Table A.43.: Minimum and maximum of the total mean dose as well as minimum and maximum of the maximal total dose for various OARs for patient 4 when dose calculation was based on non-rigid registration. Results for the complete treatment course are shown here. Interplay, lateral BT, BT and RDBT have been used for Tables A.44a, A.44b, A.44c, and A.44d, respectively.

OAR	mean dose _{min}	mean dose _{max}	max dose _{min}	max dose _{max}
esophagus	0.6 Gy (RBE)	0.6 Gy (RBE)	10.5 Gy (RBE)	14.0 Gy (RBE)
spinal cord	0.0 Gy (RBE)	0.0 Gy (RBE)	0.4 Gy (RBE)	0.4 Gy (RBE)
heart	0.0 Gy (RBE)	0.0 Gy (RBE)	0.0 Gy (RBE)	0.0 Gy (RBE)

(a) Interplay

OAR	mean dose _{min}	mean dose _{max}	max dose _{min}	max dose _{max}
esophagus	0.7 Gy (RBE)	0.7 Gy (RBE)	10.9 Gy (RBE)	14.9 Gy (RBE)
spinal cord	0.0 Gy (RBE)	0.0 Gy (RBE)	0.3 Gy (RBE)	0.3 Gy (RBE)
heart	0.0 Gy (RBE)	0.0 Gy (RBE)	0.0 Gy (RBE)	0.0 Gy (RBE)

(b) lateral BT

OAR	mean dose _{min}	mean dose _{max}	max dose _{min}	max dose _{max}
esophagus	0.7 Gy (RBE)	0.7 Gy (RBE)	9.9 Gy (RBE)	12.6 Gy (RBE)
spinal cord	0.0 Gy (RBE)	0.0 Gy (RBE)	0.3 Gy (RBE)	0.3 Gy (RBE)
heart	0.0 Gy (RBE)	0.0 Gy (RBE)	0.0 Gy (RBE)	0.0 Gy (RBE)

(c) BT

OAR	mean dose _{min}	mean dose _{max}	max dose _{min}	max dose _{max}
esophagus	0.7 Gy (RBE)	0.7 Gy (RBE)	10.3 Gy (RBE)	13.8 Gy (RBE)
spinal cord	0.0 Gy (RBE)	0.0 Gy (RBE)	0.2 Gy (RBE)	0.3 Gy (RBE)
heart	0.0 Gy (RBE)	0.0 Gy (RBE)	0.0 Gy (RBE)	0.0 Gy (RBE)

(d) RDBT

Table A.44.: Minimum and maximum of the total mean dose as well as minimum and maximum of the maximal total dose for various OARs for patient 5 when dose calculation was based on non-rigid registration. Results for the complete treatment course are shown here. Interplay, lateral BT, BT and RDBT have been used for Tables A.45a, A.45b, A.45c, and A.45d, respectively.

OAR	mean dose _{min}	mean dose _{max}	max dose _{min}	max dose _{max}
spinal cord	1.0 Gy (RBE)	1.1 Gy (RBE)	7.6 Gy (RBE)	11.4 Gy (RBE)
esophagus	3.1 Gy (RBE)	3.7 Gy (RBE)	19.9 Gy (RBE)	23.5 Gy (RBE)
heart	5.1 Gy (RBE)	5.3 Gy (RBE)	27.0 Gy (RBE)	32.6 Gy (RBE)
carina	1.2 Gy (RBE)	1.8 Gy (RBE)	14.9 Gy (RBE)	18.1 Gy (RBE)

(a) Interplay

OAR	mean dose _{min}	mean dose _{max}	max dose _{min}	max dose _{max}
spinal cord	1.0 Gy (RBE)	1.1 Gy (RBE)	5.8 Gy (RBE)	7.8 Gy (RBE)
esophagus	2.5 Gy (RBE)	2.7 Gy (RBE)	17.3 Gy (RBE)	23.9 Gy (RBE)
heart	5.7 Gy (RBE)	5.7 Gy (RBE)	28.7 Gy (RBE)	32.8 Gy (RBE)
carina	0.2 Gy (RBE)	0.3 Gy (RBE)	4.8 Gy (RBE)	7.9 Gy (RBE)

(b) lateral BT

OAR	mean dose _{min}	mean dose _{max}	max dose _{min}	max dose _{max}
spinal cord	1.0 Gy (RBE)	1.0 Gy (RBE)	4.7 Gy (RBE)	5.6 Gy (RBE)
esophagus	2.2 Gy (RBE)	2.3 Gy (RBE)	16.1 Gy (RBE)	21.0 Gy (RBE)
heart	5.5 Gy (RBE)	5.5 Gy (RBE)	28.6 Gy (RBE)	30.7 Gy (RBE)
carina	0.2 Gy (RBE)	0.3 Gy (RBE)	4.4 Gy (RBE)	7.4 Gy (RBE)

(c) BT

OAR	mean dose _{min}	mean dose _{max}	max dose _{min}	max dose _{max}
spinal cord	1.0 Gy (RBE)	1.0 Gy (RBE)	5.1 Gy (RBE)	6.2 Gy (RBE)
esophagus	2.3 Gy (RBE)	2.4 Gy (RBE)	16.8 Gy (RBE)	22.2 Gy (RBE)
heart	5.4 Gy (RBE)	5.4 Gy (RBE)	27.6 Gy (RBE)	31.2 Gy (RBE)
carina	0.2 Gy (RBE)	0.3 Gy (RBE)	4.4 Gy (RBE)	7.0 Gy (RBE)

(d) RDBT

Bibliography

- Alpen, E. L. (1998). *Radiation Biophysics*. Academic Press, 2nd edition.
- Amaldi, U. (2004). CNAO-the Italian centre for light-ion therapy. *Radiotherapy and Oncology*, 73(Supplement 2):S191–S201.
- Andersen, H. H. and Ziegler, J. F. (1977). *Hydrogen: Stopping Powers and Ranges in All Elements*. Pergamon Press, 1st edition.
- Balter, J. M., Lam, K. L., McGinn, C. J., Lawrence, T. S., and Haken, R. K. T. (1998). Improvement of CT-based treatment-planning models of abdominal targets using static exhale imaging. *International Journal of Radiation Oncology*Biology*Physics*, 41(4):939–943.
- Barkas, W. H. (1963). *Nuclear research emulsions. Techniques and theory*. Academic Press, 1st edition.
- Bartlett, M. S. (1937). Properties of sufficiency and statistical tests. *Proceedings of The Royal Society of London. Series A, Mathematical and Physical Sciences*, 160:268–282.
- Bert, C. (2006). *Bestrahlungsplanung für bewegte Zielvolumina in der Tumorthherapie mit gescanntem Kohlenstoffstrahl*. Dissertation, TU Darmstadt.
- Bert, C. and Durante, M. (2011). Motion in radiotherapy: particle therapy. *Physics in Medicine and Biology*, 56(16):R113.
- Bert, C., Gemmel, A., Chaudhri, N., Lüchtenborg, R., Saito, N., Durante, M., and Rietzel, E. (2009a). Rescanning to mitigate the impact of motion in scanned particle therapy. *GSI Scientific Report 2008*, page 397.
- Bert, C., Gemmel, A., Saito, N., and Rietzel, E. (2009b). Gated irradiation with scanned particle beams. *International Journal of Radiation Oncology*Biology*Physics*, 73(4):1270–1275.
- Bert, C., Groezinger, S. O., and Rietzel, E. (2008). Quantification of interplay effects of scanned particle beams and moving targets. *Physics in Medicine and Biology*, 53(9):2253–2265.
- Bert, C., Metheany, K. G., Doppke, K., and Chen, G. T. (2005). A phantom evaluation of a stereo-vision surface imaging system for radiotherapy patient setup. *Medical Physics*, 32(9):2753–2762.

-
- Bert, C. and Rietzel, E. (2007). 4D treatment planning for scanned ion beams. *Radiation Oncology*, 2(24).
- Bert, C., Saito, N., Schmidt, A., Chaudhri, N., Schardt, D., and Rietzel, E. (2007). Target motion tracking with a scanned particle beam. *Medical Physics*, 34(12):4768–4771.
- Bethe, H. (1930). Zur Theorie des Durchgangs schneller Korpuskularstrahlung durch Materie. *Annalen der Physik*, 5(5):325–400.
- Brock, K. K. (2010). Results of a multi-institution deformable registration accuracy study (MIDRAS). *International Journal of Radiation Oncology*Biology*Physics*, 76(2):583–596.
- Brock, K. K., Dawson, L. A., Sharpe, M. B., Moseley, D. J., and Jaffray, D. A. (2006). Feasibility of a novel deformable image registration technique to facilitate classification, targeting, and monitoring of tumor and normal tissue. *International Journal of Radiation Oncology*Biology*Physics*, 64(4):1245–1254.
- Bucci, M. K., Bevan, A., and Roach, M. (2005). Advances in radiation therapy: Conventional to 3D, to IMRT, to 4D, and beyond. *CA: A Cancer Journal for Clinicians*, 55(2):117–134.
- Chaudhri, N., Saito, N., Bert, C., Franczak, B., Steidl, P., Durante, M., Rietzel, E., and Schardt, D. (2010). Ion-optical studies for a range adaptation method in ion beam therapy using a static wedge degrader combined with magnetic beam deflection. *Physics in Medicine and Biology*, 55(12):3499–3513.
- Combs, S. E., Jakel, O., Haberer, T., and Debus, J. (2010). Particle therapy at the Heidelberg Ion Therapy Center (HIT) - Integrated research-driven university-hospital-based radiation oncology service in Heidelberg, Germany. *Radiotherapy and Oncology*, 95(1):41–44.
- Cui, Y., Dy, J. G., Sharp, G. C., Alexander, B., and Jiang, S. B. (2007). Multiple template-based fluoroscopic tracking of lung tumor mass without implanted fiducial markers. *Physics in Medicine and Biology*, 52(20):6229–6242.
- Eckermann, M., Hillbrand, M., Herbst, M., and Rinecker, H. (2011). Scanning proton beam radiotherapy under functional apnea. In *Proceedings of the PTCOG 50*. PTCOG 50.
- Edge, S. B., Byrd, D. R., Compton, C. C., Fritz, A. G., Greene, F. L., and Trotti, A., editors (2009). *AJCC Cancer Staging Manual*. Springer, 7th edition.
- Elsässer, T. and Scholz, M. (2007). Cluster effects within the local effect model. *Radiation Research*, 167(3):319–329.
- Elsässer, T., Weyrather, W. K., Friedrich, T., Durante, M., Iancu, G., Kramer, M., Kragl, G., Brons, S., Winter, M., Weber, K. J., and Scholz, M. (2010). Quantification of the relative biological effectiveness for ion beam radiotherapy: direct experimental comparison of proton and carbon

-
- ion beams and a novel approach for treatment planning. *International Journal of Radiation Oncology*Biology*Physics*, 78(4):1177–1183.
- Engelsman, M. and Bert, C. (2011). Precision and Uncertainties in Proton Therapy for Moving Targets. In Paganetti, H., editor, *Proton Therapy Physics*. Taylor & Francis.
- Enghardt, W., Crespo, P., Fiedler, F., Hinz, R., Parodi, K., Pawelke, J., and Poenisch, F. (2004). Charged hadron tumour therapy monitoring by means of PET. *Nuclear Instruments and Methods A*, 525(1-2):284–288.
- Erridge, S. C., Seppenwoolde, Y., Muller, S. H., Jaeger, K. D., Belderbos, J. S. A., Boersma, L. J., and Lebesque, J. V. (2003). Portal imaging to assess set-up errors, tumor motion and tumor shrinkage during conformal radiotherapy of non-small cell lung cancer. *Radiotherapy and Oncology*, 66(1):75–85.
- Evans, P. M. (2008). Anatomical imaging for radiotherapy. *Physics in Medicine and Biology*, 53(12):R151–R191.
- Flint-Richter, P. and Sadetzki, S. (2007). Genetic predisposition for the development of radiation-associated meningioma: an epidemiological study. *The Lancet Oncology*, 8(5):403–410.
- Freund, L. (1897). Ein mit Röntgenstrahlen behandelter Fall von Naevus pigmentosus piliferus. *Wiener Medizinische Wochenschrift*, 47:428–434.
- Friedrich, T. (2011). Internal communication.
- Friedrich, T., Scholz, U., Elsässer, T., Durante, M., and Scholz, M. (2012). Calculation of the biological effects of ion beams based on the microscopic spatial damage distribution pattern. *International Journal of Radiation Oncology*Biology*Physics*, 88(1–2):103–107.
- Furukawa, T., Inaniwa, T., Sato, S., Shirai, T., Mori, S., Takeshita, E., Mizushima, K., Himukai, T., and Noda, K. (2010a). Moving target irradiation with fast rescanning and gating in particle therapy. *Medical Physics*, 37(9):4874–4879.
- Furukawa, T., Inaniwa, T., Sato, S., Shirai, T., Takei, Y., Takeshita, E., Mizushima, K., Iwata, Y., Himukai, T., Mori, S., Fukuda, S., Minohara, S., Takada, E., Murakami, T., and Noda, K. (2010b). Performance of the NIRS fast scanning system for heavy-ion radiotherapy. *Medical Physics*, 37(11):5672–5682.
- Furukawa, T., Inaniwa, T., Sato, S., Tomitani, T., Minohara, S., Noda, K., and Kanai, T. (2007). Design study of a raster scanning system for moving target irradiation in heavy-ion radiotherapy. *Medical Physics*, 34(3):1085–1097.

-
- Grözinger, S. O. (2004). *Volume Conformal Irradiation of Moving Target Volumes with Scanned Ion Beams*. Dissertation, TU Darmstadt.
- Grözinger, S. O., Li, Q., Rietzel, E., Haberer, T., and Kraft, G. (2004). 3D online compensation of target motion with scanned particle beam. *Radiotherapy and Oncology*, 73(Supplement 2):S77–S79.
- Haberer, T., Becher, W., Schardt, D., and Kraft, G. (1993). Magnetic scanning system for heavy ion therapy. *Nuclear Instruments and Methods A*, 330:296–305.
- Haberer, T., Debus, J., Eickhoff, H., Jakel, O., Schulz-Ertner, D., and Weber, U. (2004). The Heidelberg Ion Therapy Center. *Radiotherapy and Oncology*, 73(Supplement 2):S186–S190.
- Hall, E. J. and Giaccia, A. J. (2006). *Radiobiology for the radiologist*. Lippincott Williams & Wilkins, 6. edition.
- Hanley, J., Debois, M. M., Mah, D., Mageras, G. S., Raben, A., Rosenzweig, K., Mychalczak, B., Schwartz, L. H., Gloeggler, P. J., and W, L. (1999). Deep inspiration breath-hold technique for lung tumors: the potential value of target immobilization and reduced lung density in dose escalation. *International Journal of Radiation Oncology*Biology*Physics*, 45(3):603–611.
- Hof, H., Herfarth, K. K., Münter, M. W., Hoess, A., Motsch, J., Wannenmacher, M., and Debus, J. (2003). Stereotactic single-dose radiotherapy of stage I non-small-cell lung cancer (NSCLC). *International Journal of Radiation Oncology*Biology*Physics*, 56(2):335–341.
- Husmann, G., Kaatsch, P., Katalinic, A., Bertz, J., Haberland, J., Kraywinkel, K., and Wolf, U. (2010). Krebs in Deutschland 2005/2006 Häufigkeiten und Trends.
- ICRU (1993a). Prescribing, Recording, and Reporting Photon Beam Therapy. Report 50.
- ICRU (1993b). Stopping powers and ranges for protons and alpha particles. Report 49.
- ICRU (1999). Prescribing, Recording and Reporting Photon Beam Therapy (Supplement to ICRU Report 50). Report 62.
- ICRU (2007). ICRU Report 78: Prescribing, Recording, and Reporting Proton-Beam Therapy. *Journal of the ICRU*, 7(2).
- IMRT Collaborative Working Group (2001). Intensity-modulated radiotherapy: current status and issues of interest. *International Journal of Radiation Oncology*Biology*Physics*, 51(4):880–914.
- Inaniwa, T., Kanematsu, N., Furukawa, T., and Hasegawa, A. (2011). A robust algorithm of intensity modulated proton therapy for critical tissue. *Physics in Medicine and Biology*, 56(15):4749–4770.

-
- Jiang, S. B., Pope, C., Jarrah, K. M. A., Kung, J. H., Bortfeld, T., and Chen, G. T. Y. (2003). An experimental investigation on intra-fractional organ motion effects in lung IMRT treatments. *Physics in Medicine and Biology*, 48(12):1773–1784.
- Kanai, T., Kanematsu, N., Minohara, S., Komori, M., Torikoshi, M., Asakura, H., Ikeda, N., Uno, T., and Takei, Y. (2006). Commissioning of a conformal irradiation system for heavy-ion radiotherapy using a layer-stacking method. *Medical Physics*, 33(8):2989–2997.
- Karger, C. P., Debus, J., Kuhn, S., and Hartmann, G. H. (2001). Three-dimensional accuracy and interfractional reproducibility of patient fixation and positioning using a stereotactic head mask system. *International Journal of Radiation Oncology*Biology*Physics*, 49(5):1493–1504.
- Karger, C. P., Jaekel, O., and Hartmann, G. H. (1999). A system for three-dimensional dosimetric verification of treatment plans in intensity-modulated radiotherapy with heavy ions. *Medical Physics*, 26(10):2125–2132.
- Karger, C. P., Peschke, P., Sanchez-Brandelik, R., Scholz, M., and Debus, J. (2006). Radiation tolerance of the rat spinal cord after 6 and 18 fractions of photons and carbon ions: Experimental results and clinical implications. *International Journal of Radiation Oncology*Biology*Physics*, 66(5):1488–1497.
- Keall, P., Vedam, S., George, R., Bartee, C., Siebers, J., Lerma, F., Weiss, E., and Chung, T. (2006). The clinical implementation of respiratory-gated intensity-modulated radiotherapy. *Medical Dosimetry*, 31(2):152–162.
- Keall, P. J. (2004). 4-dimensional computed tomography imaging and treatment planning. *Seminars in Radiation Oncology*, 14(1):81–90.
- Keall, P. J., Joshi, S., Vedam, S. S., Siebers, J. V., Kini, V. R., and Mohan, R. (2005). Four-dimensional radiotherapy planning for DMLC-based respiratory motion tracking. *Medical Physics*, 32(4):942–951.
- Keall, P. J., Kini, V. R., Vedam, S. S., and Mohan, R. (2001). Motion adaptive x-ray therapy: a feasibility study. *Physics in Medicine and Biology*, 46(1):1–10.
- Kiefer, J. and Straaten, H. (1986). A model of ion track structure based on classical collision dynamics. *Physics in Medicine and Biology*, 31(11):1201–1209.
- Kilby, W., Dooley, J. R., Kuduvalli, G., Sayeh, S., and C. R. Maurer, J. (2010). The Cyberknife® Robotic Radiosurgery System in 2010. *Technology in Cancer Research and Treatment*, 9(5):433–452.

-
- Kimura, T., Hirokawa, Y., Murakami, Y., Tsujimura, M., Nakashima, T., Ohno, Y., Kenjo, M., Kaneyasu, Y., Wadasaki, K., and Ito, K. (2004). Reproducibility of organ position using voluntary breath-hold method with spirometer for extracranial stereotactic radiotherapy. *International Journal of Radiation Oncology*Biology*Physics*, 60(4):1307–1313.
- Knopf, A., Hug, E., and Lomax, A. (2010). Scanned proton radiotherapy for mobile targets - which plan characteristics require rescanning, which maybe not? In *Proceedings of the XVIth ICCR*. XVIth ICCR.
- Koehler, A., Schneider, R., and Sisterson, J. (1975). Range modulators for protons and heavy ions. *Nuclear Instruments and Methods*, 131(3):437–440.
- Koehler, A. M., Schneider, R. J., , and Sisterson, J. M. (1977). Flattening of proton dose distributions for large-field radiotherapy. *Medical Physics*, 4(4):297–301.
- Krämer, M., Jaekel, O., Haberer, T., Kraft, G., Schardt, D., and Weber, U. (2000). Treatment planning for heavy-ion radiotherapy: physical beam model and dose optimization. *Physics in Medicine and Biology*, 45(11):3299–3317.
- Krämer, M. and Kraft, G. (1994). Calculations of heavy-ion track structure. *Radiation and Environmental Biophysics*, 33(2):91–109.
- Krämer, M. and Scholz, M. (2000). Treatment planning for heavy-ion radiotherapy: calculation and optimization of biologically effective dose. *Physics in Medicine and Biology*, 45(11):3319–3330.
- Krämer, M. and Scholz, M. (2006). Rapid calculation of biological effects in ion radiotherapy. *Physics in Medicine and Biology*, 51(8):1959–1970.
- Krämer, M., Weyrather, W. K., and Scholz, M. (2003). The increased biological effectiveness of heavy charged particles: from radiobiology to treatment planning. *Technology in Cancer Research and Treatment*, 2(5):427–436.
- Kubo, H. D. and Hill, B. C. (1996). Respiration gated radiotherapy treatment: a technical study. *Physics in Medicine and Biology*, 41(1):83–91.
- Langen, K. M. and Jones, D. T. L. (2001). Organ motion and its management. *International Journal of Radiation Oncology*Biology*Physics*, 50(1):265–278.
- Li, T., Thorndyke, B., Schreibmann, E., Yang, Y., and Xing, L. (2006). Model-based image reconstruction for four-dimensional PET. *Medical Physics*, 33(5):1288–1298.
- Lindhard, J., Scharff, M., and Schiott, H. E. (1963). Range concepts and heavy ion ranges. *Kongelige Danske Videnskab Selskab Mat-fys Medd*, 33(14):1–42.

-
- Liu, H. H., Balter, P., Tutt, T., Choi, B., Zhang, J., Wang, C., Chi, M., Luo, D., Pan, T., Hunjan, S., Starkschall, G., Rosen, I., Prado, K., Liao, Z., Chang, J., Komaki, R., Cox, J. D., Mohan, R., and Dong, L. (2007). Assessing respiration-induced tumor motion and internal target volume using four-dimensional computed tomography for radiotherapy of lung cancer. *International Journal of Radiation Oncology*Biology*Physics*, 68(2):531–540.
- Low, D. A., Nystrom, M., Kalinin, E., Parikh, P., Dempsey, J. F., Bradley, J. D., Mutic, S., Wahab, S. H., Islam, T., Christensen, G., Politte, D. G., and Whiting, B. R. (2003). A method for the reconstruction of four-dimensional synchronized CT scans acquired during free breathing. *Medical Physics*, 30(6):1254–1263.
- Lu, W., Chen, M., Ruchala, K. J., Chen, Q., Langen, K. M., Kupelian, P. A., and Olivera, G. H. (2009). Real-time motion-adaptive-optimization (MAO) in tomotherapy. *Physics in Medicine and Biology*, 54(14):4373–4398.
- Lujan, A. E., Larsen, E. W., Balter, J. M., and Haken, R. K. T. (1999). A method for incorporating organ motion due to breathing into 3D dose calculations. *Medical Physics*, 26(5):715–720.
- Lüchtenborg, R., Saito, N., Durante, M., and Bert, C. (2011). Experimental verification of a real-time compensation functionality for dose changes due to target motion in scanned particle therapy. *Medical Physics*, 38(10):5448–5458.
- Mackie, R. T., Holmes, T., Swerdloff, S., Reckwerdt, P., Deasy, J. O., Yang, J., Paliwal, B., and Kinsella, T. (1993). Tomotherapy: A new concept for the delivery of dynamic conformal radiotherapy. *Medical Physics*, 20(6):1709–1719.
- Michalski, D., Sontag, M., Li, F., de Andrade, R. S., Uslene, I., Brandner, E. D., Heron, D. E., Yue, N., and Huq, M. S. (2008). Four-dimensional computed tomography-based interfractional reproducibility study of lung tumor intrafractional motion. *International Journal of Radiation Oncology*Biology*Physics*, 71(3):714 – 724.
- Minohara, S., Kanai, T., Endo, M., Noda, K., and Kanazawa, M. (2000). Respiratory gated irradiation system for heavy-ion radiotherapy. *International Journal of Radiation Oncology*Biology*Physics*, 47(4):1097–1103.
- Miyamoto, T., Baba, M., Sugane, T., Nakajima, M., Yashiro, T., Kagei, K., Hirasawa, N., Sugawara, T., Yamamoto, N., Koto, M., Ezawa, H., Kadono, K., Tsujii, H., Mizoe, J. E., Yoshikawa, K., Kandatsu, S., and Fujisawa, T. (2007). Carbon ion radiotherapy for stage I non-small cell lung cancer using a regimen of four fractions during 1 week. *Journal of Thoracic Oncology*, 2(10):916–926.
- Miyamoto, T., Yamamoto, N., Nishimura, H., Koto, M., Tsujii, H., Mizoe, J. E., Kamada, T., Kato, H., Yamada, S., Morita, S., Yoshikawa, K., Kandatsu, S., and Fujisawa, T. (2003). Carbon ion

-
- radiotherapy for stage i non-small cell lung cancer. *Radiotherapy and Oncology*, 66(2):127–140.
- Molière, G. (1948). Theorie der Streuung schneller geladener Teilchen II. Mehrfach- und Vielfachstreuung. *Zeitschrift für Naturforschung A*, 2:78–96.
- Mori, S., Endo, M., and Asakura, H. (2006). Improvement in banding artefacts in four-dimensional computed tomography for radiotherapy planning. *Physics in Medicine and Biology*, 51(20):5231–5244.
- Murthy, V., Master, Z., Adurkar, P., Mallick, I., Mahantshetty, U., Bakshi, G., Tongaonkar, H., and Shrivastava, S. (2011). ‘plan of the day’ adaptive radiotherapy for bladder cancer using helical tomotherapy. *Radiotherapy and Oncology*, 99(1):55–60.
- Nakamura, K. and Particle Data Group (2010). Review of particle physics. *Journal of Physics G: Nuclear and Particle Physics*, 37(7A).
- Negoro, Y., Nagata, Y., Aoki, T., Mizowaki, T., Araki, N., Takayama, K., Kokubo, M., Yano, S., Koga, S., and Sasai, K. (2001). The effectiveness of an immobilization device in conformal radiotherapy for lung tumor: reduction of respiratory tumor movement and evaluation of the daily setup accuracy. *International Journal of Radiation Oncology*Biology*Physics*, 50(4):889–898.
- Nohadani, O., Seco, J., and Bortfeld, T. (2010). Motion management with phase-adapted 4D-optimization. *Physics in Medicine and Biology*, 55(17):5189–5202.
- Ozhasoglu, C., Saw, C. B., Chen, H., Burton, S., Komanduri, K., Yue, N. J., Huq, S. M., and Heron, D. E. (2008). Synchrony - cyberknife respiratory compensation technology. *Medical Dosimetry*, 33(2):117–123.
- Pedroni, E., Bacher, R., Blattmann, H., Boehringer, T., Coray, A., Lomax, A., Lin, S., Munkel, G., Scheib, S., Schneider, U., and Tourovsky, A. (1995). The 200-MeV proton therapy project at the Paul Scherrer Institute: Conceptual design and practical realization. *Medical Physics*, 22(1):37–53.
- Pedroni, E., Bearpark, R., Boehringer, T., and Coray, A. (2004). The PSI Gantry 2: a second generation proton scanning gantry. *Zeitschrift für Medizinische Physik*, 14(1):25–34.
- Persson, G. F., Nygaard, D. E., Brink, C., Jahn, J. W., af Rosenschöld, P. M., Specht, L., and Korreman, S. S. (2010). Deviations in delineated GTV caused by artefacts in 4DCT. *Radiotherapy and Oncology*, 96(1):61–66.
- Phillips, M. H., Pedroni, E., Blattmann, H., Boehringer, T., Coray, A., and Scheib, S. (1992). Effects of respiratory motion on dose uniformity with a charged particle scanning method. *Physics in Medicine and Biology*, 37(1):223–233.
-

-
- Richter, D., Trautmann, J., Schwarzkopf, A., Kraemer, M., Gemmel, A., Jaekel, O., Durante, M., and Bert, C. (2011). 4D treatment planning implementations for TRiP98. *GSI Scientific Report 2010*.
- Rietzel, E. and Chen, G. T. Y. (2006). Deformable registration of 4D computed tomography data. *Medical Physics*, 33(11):4423–4430.
- Rietzel, E., Chen, G. T. Y., Choi, N. C., and Willet, C. G. (2005a). Four-dimensional image-based treatment planning: Target volume segmentation and dose calculation in the presence of respiratory motion. *International Journal of Radiation Oncology*Biology*Physics*, 61(5):1535–1550.
- Rietzel, E., Pan, T., and Chen, G. T. Y. (2005b). Four-dimensional computed tomography: Image formation and clinical protocol. *Medical Physics*, 32(4):874–889.
- Ritchie, C. J., Hsieh, J., Gard, M. F., Godwin, J. D., Kim, Y., and Crawford, C. R. (1994). Predictive respiratory gating: a new method to reduce motion artifacts on CT scans. *Radiology*, 190(3):847–852.
- Saito, N., Bert, C., Chaudhri, N., Durante, M., Gemmel, A., Lüchtenborg, R., Kraft, G., and Rietzel, E. (2010). Quality assurance test of the real-time beam tracking system. *GSI Scientific Report 2009*.
- Saito, N., Bert, C., Chaudhri, N., Gemmel, A., Schardt, D., and Rietzel, E. (2009). Speed and accuracy of a beam tracking system for treatment of moving targets with scanned ion beams. *Physics in Medicine and Biology*, 54:4849–4862.
- Schardt, D., Elsaesser, T., and Schulz-Ertner, D. (2010). Heavy-ion tumor therapy: Physical and radiobiological benefits. *Reviews of Modern Physics*, 82(1):383–425.
- Schlegel, W. and Mahr, A. (2001). *3D Conformal Radiation Therapy: Multimedia Introduction to Methods and Techniques*. Springer.
- Scholz, M. and Kraft, G. (1996). Track structure and the calculation of biological effects of heavy charged particles. *Advances in Space Research*, 18:5–14.
- Schweikard, A., Shiomi, H., and Adler, J. (2004). Respiration tracking in radiosurgery. *Medical Physics*, 31(10):2738–2741.
- Schweikard, A., Shiomi, H., and Adler, J. (2005). Respiration tracking in radiosurgery without fiducials. *The International Journal of Medical Robotics + Computer Assisted Surgery*, 1(2):19–27.

-
- Seco, J., Robertson, D., Trofimov, A., and Paganetti, H. (2009). Breathing interplay effects during proton beam scanning: simulation and statistical analysis. *Physics in Medicine and Biology*, 54(14):N283–N294.
- Seppenwoolde, Y., Berbeco, R. I., Nishioka, S., Shirato, H., and Heijmen, B. (2007). Accuracy of tumor motion compensation algorithm from a robotic respiratory tracking system: a simulation study. *Medical Physics*, 34(7):2774–2784.
- Serban, M., Heath, E., Stroian, G., Collins, D. L., and Seuntjens, J. (2008). A deformable phantom for 4D radiotherapy verification: design and image registration evaluation. *Medical Physics*, 35(3):1094–1102.
- Shackelford, J. A., Kandasamy, N., and Sharp, G. C. (2010). On developing B-spline registration algorithms for multi-core processors. *Physics in Medicine and Biology*, 55(21):6329–6351.
- Shirato, H., Harada, T., Harabayashi, T., Hida, K., Endo, H., Kitamura, K., Onimaru, R., Yamazaki, K., Kurauchi, N., Shimizu, T., Shinohara, N., Matsushita, M., aka Akita, H., and Miyasaka, K. (2003). Feasibility of insertion/implantation of 2.0-mm-diameter gold internal fiducial markers for precise setup and real-time tumor tracking in radiotherapy. *International Journal of Radiation Oncology*Biology*Physics*, 56(1):240–247.
- Sonke, J. J. and Belderbos, J. (2010). Adaptive radiotherapy for lung cancer. *Seminars in Radiation Oncology*, 20(2):94–106.
- Sonke, J. J., Lebesque, J., and van, H. M. (2008). Variability of four-dimensional computed tomography patient models. *International Journal of Radiation Oncology*Biology*Physics*, 70(2):590–598.
- Steidl, P. (2011). *Gating for scanned ion beam therapy*. Dissertation, TU Darmstadt.
- Steinsträter, O., Grün, R., Scholz, U., Friedrich, T., Durante, M., and Scholz, M. (2011). Mapping of RBE-weighted doses between HIMAC- and LEM-based treatment planning systems. *International Journal of Radiation Oncology*Biology*Physics*, in Press.
- Tobias, C. A., Lawrence, J. H., Born, J. L., McCombs, R. K., Roberts, J. E., Anger, H. O., Low-Beer, B. V., and Huggins, C. B. (1958). Pituitary irradiation with high-energy proton beams: a preliminary report. *Cancer Research*, 18(2):121–134.
- Tryggestad, E., Christian, M., Ford, E., Kut, C., Le, Y., Sanguineti, G., Song, D. Y., and Kleinberg, L. (2011). Inter- and intrafraction patient positioning uncertainties for intracranial radiotherapy: A study of four frameless, thermoplastic mask-based immobilization strategies using daily cone-beam CT. *International Journal of Radiation Oncology*Biology*Physics*, 80(1):281–290.

-
- Tsuji, H., Mizoe, J., Kamada, T., Baba, M., Tsuji, H., Kato, H., Kato, S., Yamada, S., Yasuda, S., Ohno, T., Yanagi, T., Imai, R., Kagei, K., Kato, H., Hara, R., Hasegawa, A., Nakajima, M., Sugane, N., Tamaki, N., Takagi, R., Kandatsu, S., Yoshikawa, K., Kishimoto, R., and Miyamoto, T. (2007). Clinical Results of Carbon Ion Radiotherapy at NIRS. *Journal of Radiation Research*, 48(Supplement A):A1–A13.
- van de Water, S., Kreuger, R., Zenklusen, S., Hug, E., and Lomax, A. J. (2009). Tumour tracking with scanned proton beams: assessing the accuracy and practicalities. *Physics in Medicine and Biology*, 54(21):6549–6563.
- Weber, U. and Kraft, G. (1999). Design and construction of a ripple filter for a smoothed depth dose distribution in conformal particle therapy. *Physics in Medicine and Biology*, 44(11):2765–2775.
- Weyrather, W. K., Ritter, S., Scholz, M., and Kraft, G. (1999). RBE for carbon track-segment irradiation in cell lines of differing repair capacity. *International Journal of Radiation Oncology*Biophysics*, 75(11):1357–1364.
- Willoughby, T. R., Kupelian, P. A., Pouliot, J., Shinohara, K., Aubin, M., M. Roach, I., Skrumeda, L. L., Balter, J. M., Litzenberg, D. W., Hadley, S. W., Wei, J. T., and Sandler, H. M. (2006). Target localization and real-time tracking using the calypso 4D localization system in patients with localized prostate cancer. *International Journal of Radiation Oncology*Biophysics*, 65(2):528–534.
- Wilson, R. R. (1946). Radiological use of fast protons. *Radiology*, 47:487–491.
- Wong, J. W., Sharpe, M. B., Jaffray, D. A., Kini, V. R., Robertson, J. M., Stromberg, J. S., and Martinez, A. A. (1999). The use of active breathing control (ABC) to reduce margin for breathing motion. *International Journal of Radiation Oncology*Biophysics*, 44(4):911–919.
- Yi, B. Y., Han-Oh, S., Lerma, F., Berman, B. L., and Yu, C. (2008). Real-time tumor tracking with preprogrammed dynamic multileaf-collimator motion and adaptive dose-rate regulation. *Medical Physics*, 35(9):3955–3962.
- Yoshitake, T., Shioyama, Y., Nakamura, K., Ohga, S., Nonoshita, T., Ohnishi, K., Terashima, K., Arimura, H., Hirata, H., and Honda, H. (2009). A clinical evaluation of visual feedback-guided breath-hold reproducibility of tumor location. *Physics in Medicine and Biology*, 54(23):7171–7182.
- Zenklusen, S. M., Pedroni, E., and Meer, D. (2010). A study on repainting strategies for treating moderately moving targets with proton pencil beam scanning at the new gantry 2 at PSI. *Physics in Medicine and Biology*, 55(17):5103–5121.



Lebenslauf

Persönliche Daten

Name Robert Lüchtenborg
Geburtstag 29. Juli 1981
Geburtsort Nordhorn

Ausbildung

seit 04/2008 **TU Darmstadt** (Durchführung an der **GSI**)
Promotion
01/2008 **Universität Münster**
Diplomabschluss in Physik
Titel der Diplomarbeit:
Produktion direkter Photonen in ultrarelativistischen Cu+Cu Stößen
am PHENIX-Experiment
10/2002–01/2008 **Universität Münster**
Physikstudium
08/1992–06/2001 **Wilhelm-Dörpfeld-Gymnasium**, Wuppertal
09/1988–07/1992 **Grundschule Rudolfstraße**, Wuppertal

Zivildienst

07/2001–04/2002 **Evangelische Kirchengemeinde Wuppertal-Uellendahl**

Nebentätigkeiten

12/2006–09/2007 **Universität Münster**
studentische Hilfskraft
05/2002 **Evangelische Kirchengemeinde Wuppertal-Uellendahl**
mobiler sozialer Dienst



Danksagungen

An dieser Stelle möchte ich mich bei allen bedanken, die zum Gelingen dieser Arbeit beigetragen haben. Zunächst danke ich Prof. Marco Durante, der mir die Doktorarbeit in dieser Arbeitsgruppe ermöglicht hat. Mein Projekt hat er stets mit großem Interesse und mit Begeisterung verfolgt. Prof. Gerhard Kraft hat entscheidend dazu beigetragen, mein Interesse nach meiner Diplomarbeit über Schwerionenkollisionen für die nicht ganz so schnellen und nicht ganz so schweren Kohlenstoffionen in der Therapie zu wecken. Er begleitet die Arbeit der Moving-Targets-Gruppe stets mit großem Interesse und wertvollen Ratschlägen. Auch für die bereitwillige Übernahme des Korreferats möchte ich ihm herzlich danken.

Christoph Bert danke ich für die Betreuung dieser Arbeit. Von all den Diskussionen, Hilfestellungen und Ideen, die man noch schnell implementieren kann, hat diese Arbeit entscheidend profitiert. Auch Nami Saito möchte ich danken, die mit vielen Ratschlägen und Ideen einen großen Beitrag am Gelingen dieser Arbeit hat. Der ganzen Moving-Targets-Gruppe möchte ich für die sehr schöne Zeit, die ich in dieser Arbeitsgruppe verbringen durfte, danken. Hierbei schließe ich natürlich auch alle ehemaligen Mitglieder der Arbeitsgruppe ein.

Besonders großen Anteil am Gelingen dieser Arbeit hatten Daniel Richter, ohne dessen unermüdliche Arbeit an TRiP4D viele Rechnungen nicht möglich gewesen wären, Nik Kurz, der mir bei der Implementierung von Hardware im Kontrollsystem eine große Hilfe war, sowie Michael Scholz und Thomas Friedrich, die als Ansprechpartner für biologische Dosisberechnung und Modellierung stets zur Verfügung standen. Außerdem möchte ich Michael Krämer danken, ohne dessen Pflege und Erweiterung der IT-Infrastruktur vor allem die Simulationen nicht möglich gewesen wären. Der ganzen Biophysik Arbeitsgruppe möchte ich für eine hervorragende Arbeitsatmosphäre danken.

I would like to thank Prof. Lei Dong for providing the 4DCT data used in the treatment planning studies.

Neben einigen der oben schon namentlich Genannten, haben auch Alexander Frank, Anna Constantinescu, John Eley und Till Dettmering durch sorgfältige Durchsicht des Manuskripts und wertvolle Hinweise zum Gelingen dieser Arbeit beigetragen.

Zum Schluss möchte ich mich bei meiner Familie und insbesondere bei meinen Eltern bedanken, die mich das gesamte Studium unterstützt und die Entstehung dieser Arbeit stets mit großem Interesse verfolgt haben. Claudia möchte ich für ihre Unterstützung, die sie mir während dieser Arbeit entgegengebracht hat, danken. Außerdem danke ich ihr für ihr Verständnis, wenn die Strahlzeit mal wieder in der Ferienzeit lag.



Erklärung zur Dissertation

Hiermit versichere ich, die vorliegende Dissertation ohne Hilfe Dritter nur mit den angegebenen Quellen und Hilfsmitteln angefertigt zu haben. Alle Stellen, die aus Quellen entnommen wurden, sind als solche kenntlich gemacht. Diese Arbeit hat in gleicher oder ähnlicher Form noch keiner Prüfungsbehörde vorgelegen.

Darmstadt, den 17. Oktober 2011

(Robert Luchtenborg)

